HEAVY HITTERS

interactions of tin ions from EUV source plasma

Luc Assink

This work has been conducted as part of the research program of the Advanced Research Center for Nanolithography (ARCNL), a public-private partnership between the University of Amsterdam, Vrije Universiteit Amsterdam, University of Groningen, the Netherlands Organisation for Scientific Research (NWO) and the semiconductor equipment manufacturer ASML. The ion-surface scattering and RFA transmission experiments were performed at the ZERNIKELEIF facility operated at the Zernike Institute for Advanced Materials at the University of Groningen. The laser-produced plasma experiments were conducted at ARCNL. The electron emission experiments were performed at TU Wien.

university of groningen / faculty of science and engineering / zernike institute for advanced materials

Zernike Institute for Advanced Materials PhD thesis series: 2026-23
ISSN: 1570-1530
Printed by: Ipskamp Printing, Enschede

Cover: Artistic impression of an emitting laser-produced tin plasma (front) and ionic tin debris moving through a hydrogen buffer gas (back).
Cover by: Luc Assink

rijksuniversiteit
groningen

HEAVY HITTERS

Interactions of tin ions from EUV source plasma

Proefschrift

ter verkrijging van de graad van doctor aan de
Rijksuniversiteit Groningen
op gezag van de
rector magnificus prof. dr. ir. J.M.A. Scherpen
en volgens besluit van het College voor Promoties.

De openbare verdediging zal plaatsvinden op

dinsdag 29 september 2026 om 16.15 uur

door

Luc Assink

geboren op 11 juli 1994
te Hengelo

Promotores
Prof. dr. ir. R.A. Hoekstra
Prof. dr. O.O. Versolato

Beoordelingscommissie
Prof. dr. ir. O.J. Luiten
Prof. dr. G. Palasantzas
Prof. dr. S. Schippers

Groningen, 2026

CONTENTS

Introduction 1
From a single transistor to billions on a microchip . . . 3
The bold leap to EUV lithography . . . 4
Laser-produced Sn plasma . . . 5
An incomplete atomic picture . . . 6
Thesis outline . . . 9

1. On the stopping of Sn^{1+} ions in H_2 gas 15
1.1 Introduction . . . 17
1.2 Research methodology . . . 19
1.2.1 The laser-produced plasma setup . . . 19
1.2.2 Data collection and analysis . . . 21
1.2.3 Modeling of the stopping cross sections . . . 26
1.3 Discussion . . . 28
1.4 Conclusion . . . 30

2. On the absence of a prominent single-collision peak in keV heavy-ion scattering 37
2.1 Introduction . . . 39
2.2 Research methods . . . 40
2.2.1 Experimental setup . . . 40
2.2.2 Binary collision approximation . . . 41
2.2.3 SPRAY simulations . . . 44
2.3 Results and discussion . . . 45
2.3.1 Experimental results . . . 45
2.3.2 SPRAY results . . . 49
2.3.3 Comparison of experiment and simulation . . . 51
2.4 Conclusion . . . 52

3. Electron emission induced by slow Sn^{1-5+} ions on metal surfaces 57
3.1 Introduction . . . 59
3.2 Mechanisms of ion-induced electron emission . . . 60
3.3 Emission statistics . . . 65
3.4 Research approach . . . 67
3.4.1 Experimental setup . . . 67
3.4.2 Spectral shape of the electron statistics spectra . . . 69
3.4.3 Spectral background . . . 71
3.4.4 MCA threshold . . . 72

3.5 Average electron yield . . . 73
3.6 Discussion . . . 76
3.6.1 Kinetic emission . . . 76
3.6.2 Potential emission . . . 80
3.7 Conclusion . . . 81

4. The voltage-dependent transmission function of a retarding field analyzer 87
4.1 Introduction . . . 89
4.2 RFA working principles . . . 91
4.3 Research methods . . . 93
4.3.1 Experimental setup . . . 93
4.3.2 Optical inspection of a grid stack . . . 93
4.3.3 Simulation approach . . . 94
4.4 Experimental results . . . 99
4.5 Simulation results . . . 101
4.5.1 Perfect grid alignment . . . 101
4.5.2 Staggered grid alignments . . . 103
4.5.3 Random grid alignment . . . 107
4.6 Conclusion . . . 109

5. The open retarding field analyzer 115
5.1 Introduction . . . 117
5.2 Design of the open RFA . . . 118
5.3 Results . . . 121
5.4 Conclusion . . . 124

Conclusion & outlook 129

Nederlandse samenvatting 135

List of publications 143

Dankwoord 147

INTRODUCTION

Exponential growth in time refers to processes in which the rate of change increases proportionally to the current size of the system. As the system grows over time, its growth speed accelerates because each increase becomes larger than the one before. This contrasts with linear growth, where the rate of increase stays the same over time, resulting in steady growth.

Examples of exponential growth emerge in many places and contexts. Population sizes can increase exponentially; for instance, the number of people newly infected with diseases like the flu and COVID-19 is proportional to the number of already-infected individuals. The same holds for chain-like chemical processes, which exhibit rapidly accelerating reaction rates. A technological example is the global production of digital data. As digital technologies have become widespread, expanding data infrastructure has enabled more devices, greater connectivity, and increased activity, which in turn generate even larger volumes of information. Over limited time spans, this expansion is well described by exponential scaling. Notably, the exponential growth of digital data is itself driven by another exponential trend.

In 1965, Gordon Moore predicted that the number of transistors on an integrated circuit, more commonly known as a microchip, would increase exponentially, initially doubling every year [1]. Transistors are the fundamental building blocks of a microchip. These chips are the workhorses of modern electronics and, as such, are present in many of the devices we use daily, ranging from smartphones and computers to electric bikes and cars. Moore later revised the doubling period to approximately every two years [2], and his prediction became known as Moore's law. For more than five decades, continuous miniaturization of transistors has enabled an increasing number of transistors to be integrated onto a single chip. As a result, transistor density has steadily increased, leading to corresponding growth in computational performance. To this day, sustaining affordable exponential growth in computing power remains the central driver of innovation in the semiconductor industry.

From a single transistor to billions on a microchip

The technological foundations of modern semiconductor manufacturing were established in the decades following the invention of the transistor in 1947 at Bell Labs [3]. A transistor has the ability to "switch", which allows computations to be performed or bits to be stored. Early transistors were fabricated as discrete components, but technological advances during the 1950s and 1960s enabled multiple transistors and their interconnections to be integrated into a circuit on a piece of semiconductor material [4]. The transition from discrete components to integrated circuits (ICs) fundamentally transformed electronics manufacturing.

Photolithography became the key enabling technology for writing increasingly smaller structures on an IC [5]. Ever since, it has remained the main driver of device scaling. The smallest printable feature size, commonly represented by the critical dimension (CD), is limited by diffraction [6]. Following the Rayleigh criterion, CD can be expressed as [7]:

$$\mathrm{CD} = k_1 \frac{\lambda}{\mathrm{NA}}, \tag{1}$$

where λ is the exposure wavelength, NA is the numerical aperture of the projection optics, and k_1 is an imaging enhancement factor. Continued reduction of CD therefore requires shorter wavelengths, larger numerical apertures, or technical improvements that lower the effective k_1 [8]. Advances in lithography systems have progressively reduced achievable feature sizes. Shortening the wavelength of photolithography systems is the boldest and most challenging step. After changing the wavelength, NA and k_1 are further optimized to achieve an even smaller CD. Fig. 1 provides a historical overview of exposure wavelengths across generations of lithography systems and illustrates how the smallest feature size has decreased by nearly three orders of magnitude over the past decades.

Early lithography systems operated at the boundary between visible and near-ultraviolet light using mercury lamp emission lines, most notably the g-line (436 nm) and later the i-line (365 nm), which supported micrometer-scale features [5]. A major transition occurred in the 1990s with the introduction of deep-ultraviolet (DUV) immersion lithography. Excimer laser sources operating at 248 nm (KrF) and later 193 nm (ArF) significantly reduced the diffraction-limited feature size. However, continued optimization of DUV systems would ultimately approach their limits [9], and discussion of next-generation lithography systems [10, 11] began in the 1990s. In the 2010s, the first production-capable next-generation lithography tools, using extreme ultraviolet (EUV) light at 13.5 nm, were shipped by ASML to chipmakers. Recently, the first high-NA ($\mathrm{NA} = 0.55$) EUV lithography systems [12], entering single-digit nanometer-scale feature sizes, were introduced.

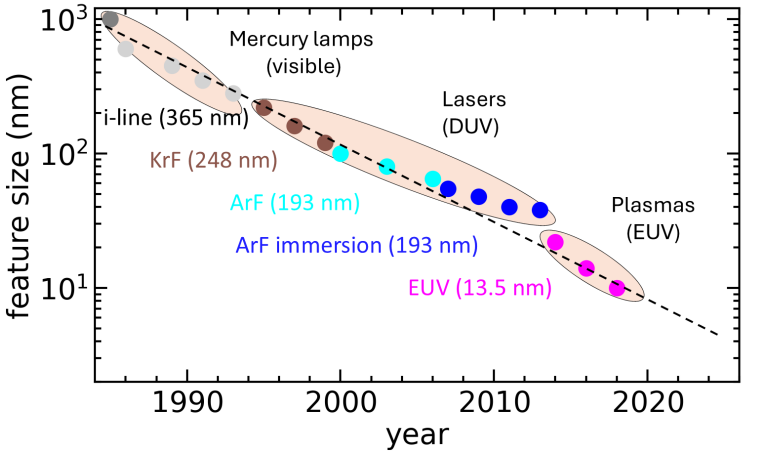

Figure 1: Historical evolution of semiconductor lithography systems using mercury lamp–based i-line (365 nm) and DUV (KrF; 248 nm, and ArF; 193 nm) to EUV (13.5 nm). The shaded regions indicate exposure wavelength regimes, while the dashed line serves as a guide to the eye, illustrating continued scaling of resolution driven by advances in light sources and optical systems.

The bold leap to EUV lithography

As a successor to 193 nm immersion lithography, several patterning approaches were considered including EUV [13], hard X-rays [14], electron-beam [15], and ion-beam lithography [16]. Among these, EUV lithography emerged as the most promising candidate. However, operating in the EUV regime introduces significant challenges. At wavelengths below 193 nm, radiation is strongly absorbed by most materials [17], including air. As a consequence, conventional refractive optics become unusable, and operation under high-vacuum conditions is required. A complete redesign of the lithography system was unavoidable. It required the development of a new type of powerful light source, compatible photoresists, and suitable optical components.

As an alternative to transmissive lenses, reflective multilayer mirrors (MLMs) were considered. These Bragg reflectors exhibit high reflectivity only within a narrow spectral bandwidth [18]. Ultimately, 13.5 nm was selected as the operating wavelength for next-generation lithography systems. At this wavelength, Mo/Si multilayer mirrors achieve a record reflectivity of 70 %, though within a narrow bandwidth of only 2 % [19, 20].

To generate 13.5 nm EUV light, several source concepts were investigated, including discharge-produced plasma, laser-produced plasma (with gas, liquid, and solid targets), and accelerator-based sources (such as the free-electron laser)

[21]. Laser-produced plasma (LPP) turned out to be the most viable. Plasmas of water [22, 23], lithium [24], xenon [25], and tin [26] were studied due to their intense emission feature near 13.5 nm, with Sn ultimately becoming the most suitable choice due to its high conversion efficiency [20].

Plasma-based sources, however, produce debris in the form of energetic ions and neutrals, posing a serious risk to the multilayer optics. So, various debris mitigation strategies were explored [27]. The adaptation of mass-limited microdroplet targets significantly reduced debris production [28]. To further mitigate ion-induced damage, a buffer gas surrounding the plasma was explored [27]. While Ar, He, and H_2 are all relatively transparent at 13.5 nm, hydrogen was chosen despite its lower stopping power. Its minimal EUV absorption and its ability to chemically remove tin deposits from plasma-facing components made it the preferred option [27, 29].

Despite the technical challenges associated with EUV lithography, ASML, a Dutch manufacturer of advanced lithography systems, was committed to its development. After a decade of research and development, this effort resulted in the introduction of the first demo-type EUV lithography system in 2006 [30]. The adoption of EUV eventually enabled a substantial reduction in critical dimensions, thereby extending the scaling trend described by Moore's law. To this day, ASML remains the only company worldwide that produces EUV lithography systems.

Laser-produced Sn plasma

Fifty thousand times per second, a microscopic tin droplet is irradiated by two successive laser pulses in the light source of an EUV lithography machine. As schematically illustrated in Fig. 2, the droplet is first hit by a relatively low-energy pre-pulse (I), which deforms it into an optimized target geometry (II). A subsequent high-energy main pulse then irradiates the shaped target (III) in order to generate the LPP (IV).

Within this plasma (IV), highly charged tin ions (Sn^{9-15+}) are formed in multiply excited states. The energy level separations of these states are all close to 92 eV, resulting in strong emission within a narrow spectral bandwidth at 13.5 nm [31–33]. A carefully engineered ellipsoidal MLM (depicted on the left side of the figure) surrounds the plasma to efficiently collect the emitted EUV radiation and direct it toward the lithographic scanner.

Alongside the desired EUV photons, the plasma also emits energetic Sn ions. These ions, which can reach high charge states and kinetic energies up to 10 keV or even more, travel outward from the plasma through a hydrogen buffer gas (V), which slows the energetic Sn ions down through collisional interactions (VI).

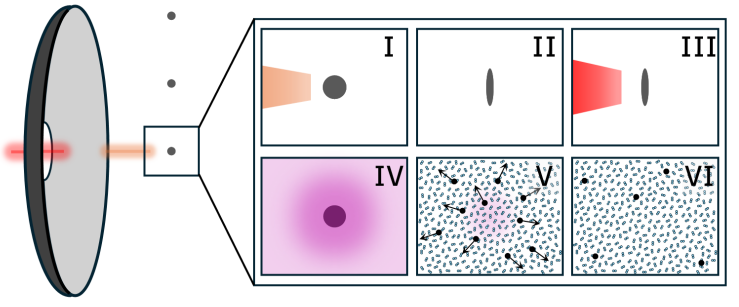

Figure 2: Schematic illustration of a laser-produced plasma EUV source. A microscopic tin droplet is first irradiated by a low-energy pre-pulse (I), deforming it into an optimized target shape (II), followed by a high-energy main pulse (III). The resulting hot plasma emits EUV radiation (IV), which is collected by the ellipsoidal multilayer mirror. Energetic Sn ions are also produced and propagate through the surrounding H_2 background gas (V), where they are slowed down before reaching plasma-facing components (VI).

If not fully mitigated, energetic ions can damage or contaminate the multilayer collector mirror, potentially reducing its lifetime and performance.

Optimizing the operation of the EUV source requires maintaining plasma conditions that maximize in-band EUV emission while simultaneously mitigating the energetic Sn ions. The continued improvement of EUV source technology remains an active field of research, to which this thesis contributes.

An incomplete atomic picture

The predictive power of simulations aiming to improve EUV source operation and output relies on accurate knowledge and understanding of particle interactions at the atomic (quantum) scale. The probabilities that specific processes occur are given by their so-called cross sections. By and large, input cross sections for models of mitigation of Sn ions escaping EUV source plasma remain largely unavailable. Here, two categories of collision can be identified: (i) ion-gas, and (ii) ion-surface. An illustration of these processes is shown in Fig. 3.

In general, one can distinguish two types of interactions, namely elastic and inelastic collision processes. In elastic scattering interactions, the total amount of kinetic energy in the system before and after the collision is the same. Elastic scattering processes will turn out to be key to the energy-loss studies presented in Chapter 1. In Chapter 3, dealing with secondary electron emission, inelastic processes are the main actors. In inelastic interactions, part of the kinetic energy is converted into potential energy, or vice versa, via electronic processes such as excitation, ionization, and/or charge exchange. The relative importance of each

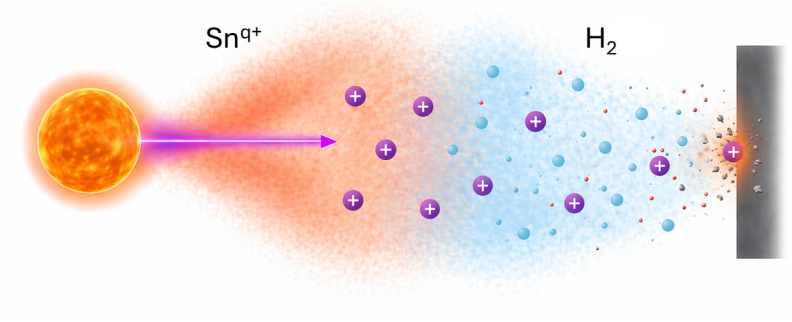

Figure 3: Artist impression of ion interactions in an EUV lithography source. EUV is generated by electronic transitions in highly charged Sn^{9-15+} ions in the core plasma. As the plasma expands, Sn^{q+} ions with kinetic energies up to 10 keV are ejected. These ions interact with the surrounding H_2 buffer gas, causing charge and energy transfer, and may eventually collide with plasma-facing materials, leading to electron emission, sputtering, and implantation.

of these processes depends on the properties of the system, such as ion energy and charge state, and the electronic structures of the projectile and target. Inelastic collisional processes, which define the far majority of collisions between Sn ions and matter, are seldom due to a single electronic process, but result from an intricate (quantum) interplay of multiple mechanisms that are inherently coupled and influence one another. As a result, simple descriptions fail even though the relevant processes are generally well identified. This, in turn, highlights the need for more detailed experimental data to advance our understanding and facilitate more accurate model calculations.

As Sn ions propagate through the hydrogen buffer gas, charge-exchange and energy-transfer processes occur. A common assumption was that charge exchange predominantly leads to Sn^{2+} as the final charge state, with this process occurring before significant energy loss sets in. This assumption is largely due to the fact that further charge exchange to Sn^{1+} is endothermic (requiring energy) in collisions with H_2, making this pathway unlikely under typical conditions. Notably, significant amounts of keV Sn^{1+} have been observed in the presence of hydrogen in laser-produced plasma sources [34]. This observation has been attributed to reaction pathways involving metastable states of Sn^{2+}. In addition, double-electron capture has been revealed as an alternative route from Sn^{3+} to Sn^{1+} [35]. The final charge state of the ions, particularly whether Sn^{1+} rather than Sn^{2+} is formed, is highly relevant, as the only experimental dataset [36] for the stopping of Sn ions in H_2 indicates a significant difference between these charge states in the keV regime. Furthermore, the commonly used stopping code SRIM systematically underestimates the stopping cross sections [27, 37], likely due to

its treatment of the projectile ions as neutral particles, its description of H_2 as two independent H atoms, and its use of a generic interaction potential. Recent theoretical and modeling data [38, 39] have improved upon these limitations but still do not provide a universal description. Together, this underlines the need for more detailed experimental and computational investigations.

If (slowed-down) ions reach the plasma-facing components, various damaging processes may occur, including sputtering and implantation. The interaction of ions with surfaces is commonly described within a binary collision approximation (BCA), in which the dynamics are governed by a sequence of elastic two-body collisions. Such BCA approaches form the basis of the widely used TRIM-type simulation codes, which are employed to estimate ion-surface interactions. Experimentally, however, probing these interactions is particularly challenging. In the low-energy regime relevant here, high neutralization probabilities and low detection efficiencies pose significant challenges to direct measurements. In addition, under normal-incidence conditions of heavy Sn ions onto relevant lighter targets, distinct BCA features such as primary backscattering or recoil peaks are not expected, further complicating the interpretation of experimental data. To enable a more direct comparison with BCA predictions, benchmark experiments [40] have therefore been performed under oblique incidence conditions, where single-collision BCA features should, in principle, be observable. Unexpectedly, however, no distinct single-collision scattering peak was observed for keV Sn ions impacting on various surfaces. This discrepancy motivated experimental and modeling efforts to understand the absence of a single-collision signature in these heavy-ion–surface interactions [41, 42], but the problem remains unsolved. A better understanding of the underlying mechanisms is therefore essential before extending such studies to collisional parameters that are more directly relevant for EUV source environments.

Changes in EUV source parameters (e.g., laser power and target size) can affect the energy and charge state distribution of Sn ions ejected by the laser-produced plasma [43]. Accurate measurements of these ion distributions are therefore essential for understanding and optimizing EUV source performance. The retarding field analyzer (RFA) is a widely used diagnostic tool for measuring energy distributions and particle fluxes of charged particles emitted from a plasma. When combined with time-of-flight spectroscopy, it enables reconstruction of charge-state-resolved energy distributions [44]. Experimental studies have demonstrated that LPP ion emission is anisotropic [45], laser-power dependent [46], and that the average charge state scales with kinetic energy [47]. Despite these insights, uncertainties remain regarding systematic errors in the diagnostic methods employed. In particular, the transmission characteristics of the RFA and

its influence on the measured ion distributions remain insufficiently quantified [48]. A gridless RFA might overcome the issues of conventional gridded RFAs.

Thesis outline

This thesis addresses several open questions in the atomic-scale description of interactions involving slow, heavy ions relevant to EUV source operation, and raises a central question addressed in this thesis: *to what extent can the required data on the atomic-scale interactions of slow heavy Sn ions under EUV source conditions be obtained in dedicated experiments?*

In Chapter 1 we investigate the stopping of LPP Sn^{1+} ions in hydrogen gas. By changing the H_2 pressure, the flight time of the ions from plasma to detector changes. From this change, stopping cross sections are extracted in the energy range 0.13–3 keV. The experiments are compared with simulations performed using our GIonS (Groningen Ion Stopping) code, a semi-classical collision model that incorporates interatomic potentials based on density functional theory (DFT) and explicitly accounts for the molecular structure of H_2.

Chapters 2 and 3 focus on the interactions of slow heavy ions with surfaces. In Chapter 2, the absence of a distinct single-collision peak in keV heavy-ion scattering experiments is investigated. We examine the extent to which surface roughness may account for the apparent missing peak. Experimental scattering spectra of 15 keV Ar^{2+}, Kr^{2+}, and Xe^{2+} ions from a polycrystalline Ru surface are presented and compared with simulations performed using the ray-tracing code SPRAY for surfaces with varying degrees of roughness. In Chapter 3 we study the ion-induced electron emission resulting from the impact of slow keV Sn^{1-5+} ions colliding with metal surfaces. Materials commonly used in detector components, such as copper and stainless steel, can become coated with tin during prolonged exposure to Sn particles escaping the EUV plasma. Therefore, electron emission yields from Sn ion impact on Sn, Cu, and stainless steel surfaces are measured to assess how secondary electrons may affect detector performance.

Chapters 4 and 5 focus on the RFA, the workhorses of ion-energy detectors in EUV sources. In Chapter 4, the ion transmission characteristics of a standard gridded RFA are studied using both experiments and SIMION simulations. The dependence of the transmission on electrode voltage and grid alignment configurations is systematically analyzed. In Chapter 5, the design and implementation of a gridless retarding field analyzer is presented. Compared with the findings for gridded RFAs, we show that a gridless RFA design eliminates the need for transmission-function corrections and avoids electron emission from grid structures, implying its superiority over a gridded RFA.

References

[1] G. E. Moore, "Cramming more components onto integrated circuits", Electronics **38**, 114–117 (1965).

[2] G. E. Moore, "Progress in digital integrated electronics", Int. Electron Devices Meet., IEEE, 11–13 (1975).

[3] J. Bardeen and W. H. Brattain, "The transistor, a semi-conductor triode", Phys. Rev. **74**, 230 (1948).

[4] J. Kilby, "Invention of the integrated circuit", IEEE Trans. Electron Devices **23**, 648–654 (1976).

[5] J. H. Bruning, "Optical lithography ... 40 years and beyond", Proc. SPIE 6520, Optical Microlithography XX, 652004 (2007).

[6] E. Abbe, "Beiträge zur theorie des mikroskops und mikroskopischen wahrnehmung", Arch. Mikros. Anat. **9**, 413 (1873).

[7] H. J. Levinson, *Principles of lithography* (SPIE Press, 2005).

[8] C. A. Mack, *Fundamental principles of optical lithography* (Wiley, 2007).

[9] H. Ito and S. Okazaki, "Pushing the limits of lithography", Nature **406**, 1027–1031 (2000).

[10] C. Wagner and N. Harned, "EUV lithography: lithography gets extreme", Nature Photonics **4**, 24–26 (2010).

[11] V. Y. Banine, K. N. Koshelev, and G. H. P. M. Swinkels, "Physical processes in EUV sources for microlithography", J. Phys. D: Appl. Phys. **44**, 253001 (2011).

[12] H. Levinson, "The era of high-NA EUV lithography has arrived!", JM3 **24** (2025).

[13] J. E. Bjorkholm, "EUV lithography—the successor to optical lithography?", Intel Technol. J. **3**, 9 (1999).

[14] J. P. Silverman, "Challenges and progress in X-ray lithography", J. Vac. Sci. Technol. B **16**, 3137–3141 (1998).

[15] W. Waskiewicz, et al., "SCALPEL proof-of-concept system: preliminary lithography results", Proc. SPIE **3048**, 2 (1997).

[16] J. Melngailis, A. A. Mondelli, I. L. Berry III, and R. Mohondroa, "A review of ion projection lithography", J. Vac. Sci. Technol. B **16**, 927–957 (1998).

[17] Center for X-Ray Optics, *X-ray interactions with matter: gas transmission calculator*, Lawrence Berkeley National Laboratory, (2024) `https://henke.lbl.gov/optical_constants/gastrn2.html`.

[18] T. W. Barbee Jr., S. Mrowka, and M. C. Hettrick, "Molybdenum-silicon multilayer mirrors for the extreme ultraviolet", Appl. Opt. **24**, 883 (1985).

[19] S. Bajt, J. B. Alameda, T. W. Barbee Jr., W. M. Clift, J. A. Folta, B. Kaufmann, and E. A. Spiller, "Improved reflectance and stability of Mo-Si multilayers", Opt. Eng. **41**, 1797 (2002).

[20] V. Banine and R. Moors, "Plasma sources for euv lithography exposure tools", J. Phys. D: Appl. Phys. **37**, 3207 (2004).

[21] J. Benschop, "EUV lithography: past, present and future", Photopolym. Sci. Technol. **4**, 263–267 (2025).

[22] S. Düsterer, H. Schwoerer, W. Ziegler, and C. Ziener, "Optimization of EUV radiation yield from laser-produced plasma", Appl. Phys. B **73**, 693–698 (2001).

[23] C. Rajyaguru, T. Higashiguchi, M. Koga, W. Sasaki, and S. Kubodera, "Systematic optimization of the extreme ultraviolet yield from a quasi-mass-limited water-jet target", Appl. Phys. B **79**, 669–672 (2004).

[24] C. Rajyaguru, T. Higashiguchi, M. Koga, K. Kawasaki, M. Hamada, N. Dojyo, W. Sasaki, and S. Kubodera, "Parametric optimization of a narrow-band 13.5-nm emission from a Li-based liquid-jet target using dual nano-second laser pulses", Appl. Phys. B **80**, 409–412 (2005).

[25] H. Komori, T. Abe, T. Suganuma, Y. Imai, Y. Sugimoto, H. Someya, H. Hoshino, G. Soumagne, Y. Takabayashi, H. Mizoguchi, A. Endo, K. Toyoda, and Y. Horiike, "Laser-produced-plasma light source development for extreme ultraviolet lithography", J. Vac. Sci. Technol. B **21**, 2843 (2003).

[26] P. A. C. Jansson, B. A. M. Hansson, O. Hemberg, M. Otendal, A. Holmberg, J. de Groot, and H. M. Hertz, "Liquid-tin-jet laser-plasma extreme ultraviolet generation", Appl. Phys. Lett. **84**, 2256–2258 (2004).

[27] S. S. Harilal, B. O'Shay, Y. Tao, and M. S. Tillack, "Ion debris mitigation from tin plasma using ambient gas, magnetic field and combined effects", Appl. Phys. B **86**, 547–553 (2007).

[28] M. Richardson, C. S. Koay, K. Takenoshita, and C. Keyser, "High conversion efficiency mass-limited Sn-based laser plasma source for extreme ultraviolet lithography", J. Vac. Sci. Technol. B **22**, 785 (2004).

[29] M. M. J. W. van Herpen, D. J. W. Klunder, W. A. Soer, R. Moors, and V. Banine, "Sn etching with hydrogen radicals to clean EUV optics", Chem. Phys. Lett. **484**, 197–199 (2010).

[30] H. Meiling, et. al., "First performance results of the ASML alpha demo tool", Proc. SPIE **6151**, 615108 (2006).

[31] W. Svendsen and G. O'Sullican, "Statistics and characteristics of xuv transition arrays from laser-produced plasmas of the elements tin through iodine", Phys. Rev. A **50**, 3710–3718 (1994).

[32] J. Colgan, D. Kilcrease, J. Abdallah, M. Sherrill, C. Fontes, P. Hakel, and G. Armstrong, "Atomic structure considerations for the low-temperature opacity of sn", High Energy Density Phys. **23**, 133–137 (2017).

[33] F. Torretti, J. Sheil, R. Schupp, M. M. Basko, M. Bayraktar, R. A. Meijer, S. Witte, W. Ubachs, R. Hoekstra, O. O. Versolato, A. J. Neukirch, and J. Colgan, "Prominent radiative contributions from multiply-excited states in laser-produced tin plasma for nanolithography", Nat. Commun. **11**, 1–8 (2020).

[34] S. Rai, K. I. Bijlsma, L. Poirier, E. de Wit, L. Assink, A. C. Lassise, I. Rabadan, L. Méndez, J. Sheil, O. O. Versolato, and R. Hoekstra, "Evidence of production of keV Sn^{+} ions in the H_2 buffer gas surrounding a Sn-plasma EUV source", Plasma Sources Sci. Technol. **32**, 035006 (2023).

[35] L. Oltra, L. Méndez, I. Rabadán, K. I. Bijlsma, E. de Wit, and R. Hoekstra, "Sequential synchronous mechanism for double-electron capture: insights into unforeseen large cross sections in low-energy $Sn^3 + H_2$ collisions", Phys. Rev. Lett. **134**, 093002 (2024).

[36] D. B. Abramenko, M. V. Spirodonov, P. V. Krainov, V. M. Krivtsun, D. I. Astakhov, V. V. Medvedev, M. van Kampen, D. Smeets, and K. N. Koshelev, "Measurements of hydrogen gas stopping efficiency for tin ions from laser-produced plasma", Appl. Phys. Lett. **112**, 164102 (2018).

[37] S. S. Harilal, B. O'Shay, Y. Tao, and M. S. Tillack, "Ambient gas effects on the dynamics of laser-produced tin plume expansion", J. Appl. Phys. **99**, 083303 (2006).

[38] N. Bartlett, A. Herschberg, J. Crouse, T. Dallal, J. Nuttal, J. Stahl, N. Braaksma, and D. Ruzic, "Elastic scattering cross sections and transport of tin ions in extreme ultraviolet lithography sources", Phys. Scr. **99**, 065411 (2024).

[39] X. Feng, Y. Song, Y. Ma, and B. Li, "DFT-based interatomic potentials for hydrogen-metal systems: improved stopping power modeling", Nucl. Instrum. and Methods Phys. Res. B **572**, 165999 (2026).

[40] M. J. Deuzeman, "Generation and interactions of energetic tin ions", PhD thesis (University of Groningen, 2019).

[41] S. Rai, K. I. Bijlsma, S. Koeleman, O. G. Tjepkema, N. W. Noordam, H. T. Jonkman, O. O. Versolato, and R. Hoekstra, "Single-collision scattering of keV-energy Kr ions off a polycrystalline Cu surface", Nucl. Instrum. and Methods Phys. Res. B **482**, 58–63 (2020).

[42] R. A. Wilhelm, M. J. Deuzeman, S. Rai, W. Husinsky, P. S. Szabo, H. Biber, R. Stadlmayr, C. Cupak, J. Hundsbichler, C. Lemell, W. Möller, A. Mutzke, G. Hobler, O. O. Versolato, F. Aumayr, and R. Hoekstra, "On the missing single collision peak in low energy heavy ion scattering", Nucl. Instrum. and Methods Phys. Res. B **544**, 165123 (2023).

[43] A. Bayerle, M. J. Deuzeman, S. van der Heijden, D. Kurilovich, T. de Faria Pinto, A. Stodolna, S. Witte, K. S. E. Eikema, W. Ubachs, and R. Hoekstra, "Sn ion energy distributions of ns- and ps-laser produced plasmas", Plasma Sources Sci. Technol. **27**, 045001 (2018).

[44] L. Poirier, A. C. Lassise, Y. Mostafa, L. Behnke, N. Braaksma, L. Assink, R. Hoekstra, and O. O. Versolato, "Energy-and charge-state-resolved spectrometry of tin laser-produced plasma using a retarding field energy analyzer", Appl. Phys. B **128**, 053302 (2021).

[45] L. Poirier, D. J. Hemminga, A. C. Lassise, L. Assink, R. Hoekstra, J. Sheil, and O. O. Versolato, "Strongly anisotropic ion emission in the expansion of Nd:YAG-laser-produced plasma", Phys. Plasmas **29**, 123102 (2022).

[46] L. Poirier, A. C. Lassise, R. Hoekstra, J. Sheil, and O. O. Versolato, "Laser-intensity dependence of ion emission from Nd:YAG-laser-produced plasma expanding into vacuum", Phys. Plasmas **30**, 083505 (2023).

[47] J. Sheil, L. Poirier, A. C. Lassise, S. Schouwenaars, N. Braaksma, A. Frenzel, R. Hoekstra, and O. O. Versolato, "Power-law scaling relating the average charge state and kinetic energy in expanding laser-driven plasmas", Phys. Rev. Lett. **133**, 125101 (2024).

[48] T. van de Ven, C. A. de Meijere, R. M. van der Horst, M. van Kampen, V. Y. Banine, and J. Beckers, "Analysis of retarding field energy analyzer transmission by simulation of ion trajectories", Rev. Sci. Instrum. **89**, 043501 (2018).

CHAPTER 1

On the stopping of Sn^{1+} ions in molecular hydrogen gas

Luc Assink, Thomas Nieboer, Jelger Bijma, Boris Neijzen, Klaas Bijlsma, Lucas Poirier, Emiel de Wit, Dion Engels, John Sheil, Oscar Versolato, and Ronnie Hoekstra

Under review

Abstract

We investigate the stopping of energetic (0.13–3 keV) Sn^{1+} ions in molecular hydrogen gas using a combined experimental and modeling approach. Data on $Sn^{q+}-H_2$ collisions in this energy range is sparse, limiting a complete atomistic understanding. Time-of-flight measurements employing retarding field analyzers are used to quantify pressure-dependent flight-time shifts of Sn^{1+} ions traversing H_2 at pressures between 2×10^{-4} and 2×10^{-2} mbar. From these shifts, stopping cross sections are extracted as a function of ion energy. To interpret the measurements, a semi-classical collision model is developed, which incorporates interaction potentials derived from density functional theory and explicitly accounts for the molecular structure of H_2. The modeled stopping cross sections are in good agreement with the experimental results. Compared with other work, our dataset falls within the range reported in the literature and occupies a central position within this range.

1.1 Introduction

In advanced semiconductor manufacturing, extreme ultraviolet (EUV) lithography at a wavelength of 13.5 nm is used to pattern at the nanometer scale [1, 2]. This radiation is generated by a laser-produced plasma (LPP), which is created by pulsed-laser irradiation of liquid tin droplets [3]. The emitted EUV radiation arises from transition arrays originating from singly [4–6], and even more so from doubly and triply [7] excited configurations of several high charge states of Sn.

In addition to EUV radiation, the LPP emits a broad distribution of energetic Sn ions. Charge- and energy-resolved measurements have shown that these ions can reach kinetic energies in the keV range and that a significant fraction leaves the plasma in moderately high charge states (4–8+ [8]). Upon interaction with plasma-facing components, such ions can deposit a substantial amount of energy into those components and thereby reduce their lifetimes. To prevent this, EUV sources are typically operated within a hydrogen buffer gas flow. The H_2 gas slows down and mitigates expelled Sn ions without appreciably absorbing EUV radiation [9–12].

As the Sn ions propagate through the hydrogen gas, they undergo collisional processes that lead to charge-state lowering and energy loss. Traditionally, this successive charge state reduction has been assumed to stop at 2+, since the one-electron capture reaction that would produce Sn^{1+} in $Sn^{2+} + H_2$ collisions is endothermic by 1.3 eV. However, recent measurements revealed a significant number of keV Sn^{1+} ions when the H_2 pressure was increased from base pressure to 6×10^{-4} mbar, while no substantial energy loss was yet observed [13]. It was shown by cross section measurements and calculations [14] that these Sn^{1+} can originate from electron capture by metastable Sn^{2+} ($4s4p\ ^3P$) ions, which are the main product ions in one-electron capture by Sn^{3+} colliding with H_2 [13]. Very recently, a second pathway was uncovered at energies below 5 keV, namely double electron capture in collisions of $Sn^{3+} + H_2$ [15], which directly leads to the production of Sn^{1+} ions. Therefore, instead of Sn^{2+} ions, that were previously thought to be the dominant end product of charge exchange, we explicitly focus on the stopping cross sections, S, of Sn^{1+} ions in H_2 at energies of 0–3 keV. The stopping cross sections relate to the macroscopic stopping power, i.e., the energy loss per unit length (dE/dx) via

$$\frac{dE}{dx} = -nS, \tag{1.1}$$

with n the density of the target.

Experimental stopping data for tin ions in molecular hydrogen gas are scarce. The only available measurements for keV Sn ions in charge states 1+ (and 2+)

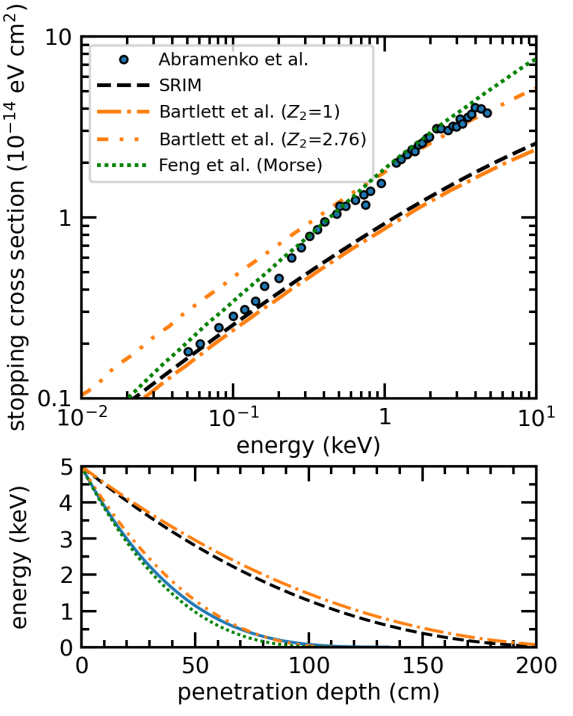

Figure 1.1: Stopping cross sections for Sn^{1+} – H_2 data available in literature (top panel). The symbols show the experimental data, and the corresponding fit by Abramenko et al. [16] for Sn^{1+}. The dashed-dotted orange lines are the calculated stopping cross sections of Bartlett et al. [17] using slightly different interaction potentials specified by the effective nuclear charge of the target of $Z_2 = 1$ and $Z_2 = 2.76$. The dotted green line is the calculated stopping cross section of Feng et al. [18] using a Morse potential. The black dashed curve shows the SRIM results. Using Eq. (1.1), the bottom panel shows the penetration depths of 5 keV Sn particles through 1 mbar of H_2 for the stopping cross section sets presented in the top panel.

are reported by Abramenko et al. [16]. The commonly used stopping code SRIM [19, 20] predicts significantly lower stopping cross sections, see Fig. 1.1. The sheer fact that SRIM calculates H_2 stopping cross sections that are too small was already clear from the pioneering research on the possibilities of Sn ion mitigation by gases such as H_2, He, and Ar [9, 10]. The underprediction of H_2 stopping cross sections by SRIM is likely linked to its treatment of the projectile ions as neutral particles, its description of the target H_2 molecules as two H atoms, and its use of the generic ZBL (Ziegler-Biersack-Littmark) potential [19, 20] as the interaction potential. Cross sections presented in the literature translate into large uncertainties in predictions of how far Sn ions expelled from the EUV source plasma penetrate into the surrounding H_2 stopping gas, as illustrated in Fig. 1.1.

Bartlett et al. [17] advanced the stopping description by using density functional theory (DFT) to obtain an interatomic potential specific to the Sn^{1+} – H_2 system. This approach significantly improved the agreement between experiment and theory.

In this work, we present an extensive set of stopping measurements for 0.12 to 3 keV Sn^{1+} ions in H_2 gas. The energy range encompasses the transition regime in which, based on the data of Abramenko et al. [16], the stopping cross section switches from being in line with the "$Z_2 = 1$" prediction to the "$Z_2 = 2.76$" prediction by Bartlett et al. [17], where Z_2 is the nuclear charge of the target (more details are given in Section 1.2.3). The Sn ions are produced by one of the laser-produced plasma sources installed at ARCNL in Amsterdam. The flight time of the ions from the LPP plasma to the detector is measured as a function of H_2 pressure. From the changes in ToF times, stopping cross sections are extracted. The results are compared to the existing experimental data of Abramenko et al. [16], to the model results by Bartlett et al. [17] and by Feng et al. [18], and to our own model extension of the approach of Bartlett et al., in which we explicitly incorporate the two-center geometry of the H_2 molecules in energy-loss trajectory calculations.

1.2 Research methodology

1.2.1 The laser-produced plasma setup

The laser-Sn plasma EUV source installed at ARCNL, Amsterdam, used here has been described in detail in earlier work, e.g., Refs. [3, 8]. A schematic overview of those parts of the ARCNL-LPP setup most relevant to the experiments is shown in Fig. 1.2.

A tin reservoir, held at a temperature of 260 °C to ensure a stable supply of molten Sn, is mounted on top of the central LPP vacuum chamber with a base pressure of approximately 1×10^{-7} mbar. Tin microdroplets are generated through an orifice in the reservoir, forming a continuous stream of droplets with a repetition rate of 22 kHz. The droplets, with a diameter of approximately 38 µm, travel downward along the vertical axis of the chamber.

Before reaching the laser-droplet interaction region, the droplet stream passes through a horizontally oriented laser light sheet. Light scattered by the droplets is detected by a photomultiplier tube, and the resulting signal is electronically down-converted to 10 Hz. This processed signal is used to trigger the Nd:YAG laser used for Sn plasma generation.

The Nd:YAG laser (at a wavelength of 1064 nm) delivers light pulses with a full-width at half-maximum (FWHM) duration of approximately 10 ns. The

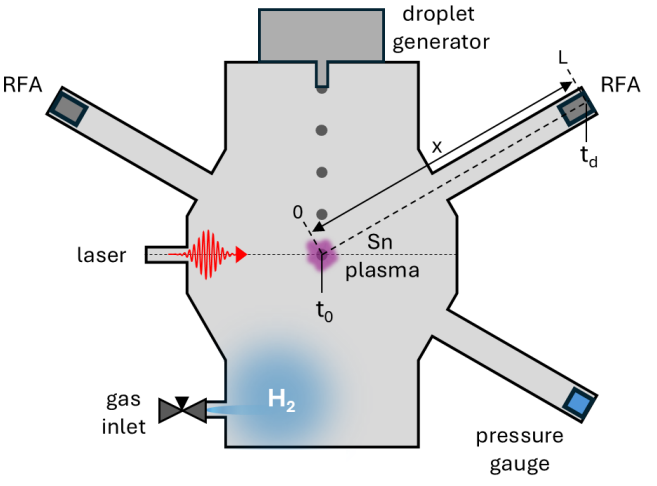

Figure 1.2: Schematic of the LPP experiment used to measure time-of-flight ion spectra as a function of the hydrogen buffer gas pressure. After their creation at t_0, ions propagate over a flight distance L from the plasma source to retarding field analyzer (RFA) detectors. A total of eight RFAs are employed at two different distances from the source. The flight time of the ions is denoted by t_d.

laser beam is focused onto the droplet to a Gaussian spot with a diameter of approximately 100 µm (FWHM). The pulse energy is adjusted using a combination of a half-wave plate and a thin-film polarizer, allowing control of the laser energy without significantly altering the beam profile. For all measurements reported here, the pulse energy was set to 90 mJ.

Ion emission from laser-produced tin plasmas is anisotropic [21]. Backward ion emission (ions coming from the back side of the target) is typically characterized by lower energies and charge states than forward emission. Consequently, low-energy 1+ ions are difficult to resolve in the forward direction, while high-energy ions are relatively scarce in the backward direction. To cover a wide range of energies, we used all our available retarding field analyzers (RFAs, of type Kimball Physics FC-73A), positioned at various observation angles relative to the incident laser.

Two RFAs were positioned in the backward direction at a flight distance of 0.68 m from the plasma source to optimize detection of low-energy ions. The remaining six RFAs were positioned at a distance of 0.93 m. The angular positions and solid angles of all RFAs are summarized in the Appendix.

Within each RFA, ions are collected by a Faraday cup biased at $V_{FC} = -30$ V. A suppressor grid held at $V_S = -100$ V is used to prevent secondary electrons from entering or escaping the cup. The retarding grid voltage V_R is stepped

between 0 to 4 kV in 90 increments, corresponding to a voltage step of 44.5 V. The ion current is converted to a voltage signal using a transimpedance amplifier with a gain of 25 kV A^{-1} and a bandwidth of 25 MHz.

All measurements were performed at controlled hydrogen pressures in the range of 2×10^{-4} to 2×10^{-2} mbar. For the analysis, the gas pressure is assumed to be uniform throughout the experimental chamber. This assumption is supported by MOLFLOW+ Monte Carlo simulations reported previously [13], which showed that pressure variations along the ion trajectories (flight distance of 0.68 m) are below 5 % under the present operating conditions.

1.2.2 Data collection and analysis

Traditional stopping experiments employ monoenergetic ion beams that pass through a gas-filled drift chamber, where the stopping cross section is either directly determined from the measured energy loss [22, 23] or indirectly measured via time-of-flight (ToF) [24, 25]. However, ions emitted from an LPP source exhibit a broad energy distribution. To address this, we follow the method proposed by Abramenko et al. [16] to extract stopping cross sections from such distributions by combining energy selection with time-of-flight measurements. In our approach, energy selection is achieved using the high-pass filtering characteristic of a retarding field analyzer (RFA), while the laser pulse that ignites the plasma provides the ToF start signal.

The voltage V_R applied to the retarding grids of the RFA creates an electrostatic potential barrier that blocks ions with kinetic energy below $E = qV_R$, where q is the charge state of the ion. As a result, a distinct cutoff appears in the ToF spectrum at flight times corresponding to ions with kinetic energy equal to qV_R.

As an example, Fig. 1.3 displays ToF current traces recorded at $V_R = 800$ V for a set of H_2 pressures covering a pressure range of 2×10^{-4} to 2×10^{-2} mbar. With increasing hydrogen pressure, changes are observed in the spectral shape, amplitude, and cutoff position. At the lowest pressures, the signal increases with pressure, while the cutoff position remains unchanged within the experimental uncertainty. At higher pressures, a shift of the cutoff towards shorter flight times emerges. At the same time, the spectral shape near the cutoff changes, and the detected ion current decreases.

These observations are in full agreement with the findings of Rai et al. [13]. They showed that, at low pressures of the LPP surrounding H_2 gas, electron capture by Sn^{q+} ions ($q > 1+$) rapidly reduces the charge states to 1+, thereby increasing the fraction of Sn^{1+} ions. This charge-state lowering precedes appreciable collisional energy loss. Only at higher pressures does energy loss

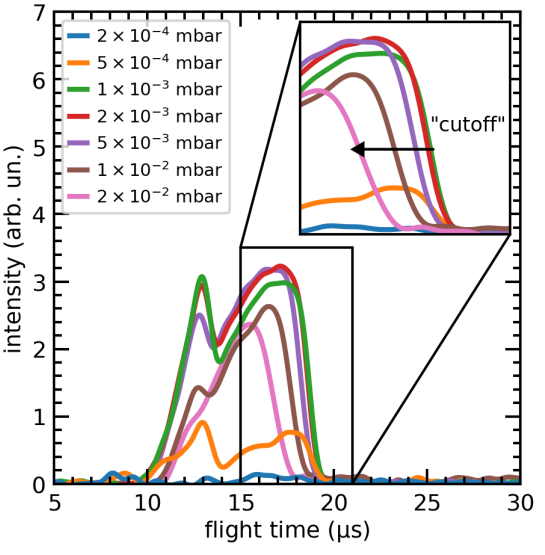

Figure 1.3: Time-of-flight current traces recorded with RFA1 (see Table 1) at a retarding voltage of $V_R = 800\,\mathrm{V}$ for hydrogen pressures between 2×10^{-4} to $2 \times 10^{-2}\,\mathrm{mbar}$. The inset highlights the characteristic cutoff associated with the high-pass energy filtering at $E_d = 800\,\mathrm{eV}$.

become significant, leading to measurable cutoff shifts and a reduction in signal. Charge-state lowering and energy loss can thus be considered not to interweave with one another.

At sufficiently high H_2 pressures in the energy loss regime, the ion energy at position x along its trajectory from plasma to detector is defined by $E(x) = E_0 - \Delta E(x)$, where E_0 is the initial energy of the ion upon being expelled from the plasma, and $\Delta E(x)$ represents the integral energy loss between 0 and x. When a Sn ion of mass M loses energy, its velocity decreases. Consequently, one has to integrate over its actual velocity $v(x)$ to determine the ToF T from plasma to the detector positioned at a distance L:

$$T = \int_0^L \frac{dx}{v(x)} = \int_0^L \sqrt{\frac{M}{2E(x)}}\, dx. \tag{1.2}$$

In the experiment, the initial energy of the ions is unknown. Ions are filtered on their energy E_d upon arrival at the detector. Therefore, it is more convenient to express $E(x)$ as $E_d + \Delta E'(x)$, where $\Delta E'(x)$ is the energy that the ion still has to lose between x and the position of the detector, L. With this substitution, Eq. (1.2) can be rewritten as:

$$T = \sqrt{\frac{M}{2E_\mathrm{d}}} \int_0^L \frac{dx}{\sqrt{1 + \frac{\Delta E'(x)}{E_\mathrm{d}}}}. \tag{1.3}$$

If there is no H_2 gas, there is no energy loss and $T = T_\mathrm{vac} = L\sqrt{M/(2E_\mathrm{d})}$. For $\Delta E'(x)$ much smaller than E_d, a first-order Taylor expansion of the denominator can be applied, yielding:

$$T \backsimeq T_\mathrm{vac} \left(1 - \frac{1}{2E_\mathrm{d}L} \int_0^L \Delta E'(x)\, dx\right). \tag{1.4}$$

The ToF difference $\Delta T = T - T_\mathrm{vac}$ is the experimental observable that can be linked to the stopping cross sections. From Eq. (1.4), it follows that:

$$\Delta T = -\frac{T_\mathrm{vac}}{2E_\mathrm{d}L} \int_0^L \Delta E'(x)\, dx. \tag{1.5}$$

Using Eq. (1.1), $\Delta E'(x)$ can be written as:

$$\Delta E'(x) = \int_x^L nS\, dx \backsimeq nS(L - x), \tag{1.6}$$

where, in the second step, it is assumed that S is constant over the full path length, which is justified if the total energy loss from the source to the detector is small compared to the ion's kinetic energy.

If we substitute Eq. (1.6) for the residual energy loss into the equation for the time-of-flight shift ΔT (Eq. (1.5)), we find:

$$\Delta T = -\frac{T_\mathrm{vac} nS}{2E_\mathrm{d}L} \int_0^L (L - x)\, dx = -\frac{T_\mathrm{vac} nSL}{4E_\mathrm{d}}. \tag{1.7}$$

Thus, the stopping cross section as a function of kinetic energy can be extracted via

$$S(E) = -\frac{4E}{T_\mathrm{vac}} \frac{\Delta T}{nL}. \tag{1.8}$$

The key experimental parameter is ΔT, which relies on a consistent determination of flight times with and without H_2 gas present. For determination of the ions' ToF, the long-flight-time cutoff edges of the ToF traces (see Fig. 1.3) are used, specifically their inclination points. These inclination points are identified by taking the derivative of the ToF traces, resulting in Gaussian-like peaks centered at the flight times marking the inclination point of the falling ToF edge. For the same set of H_2 pressures as shown in Fig. 1.3, Fig. 1.4 presents the derivatives of the ToF traces. The peak positions, which define the ion cutoff flight times T,

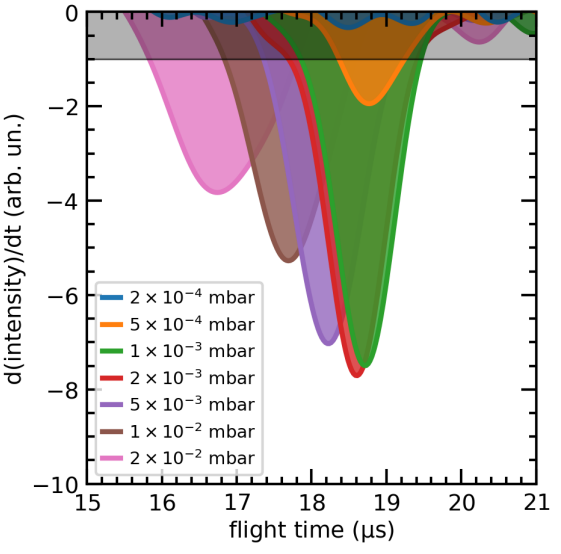

Figure 1.4: Derivatives of ToF traces taken at a retarding voltage of $V_R = 800\,V$ for H_2 pressures in the range of 2×10^{-4} to 2×10^{-2} mbar (same dataset as in Fig. 1.3). The positions of the minima mark the ions' ToF at the cutoff. The dashed line indicates the threshold acceptance level applied in the analysis.

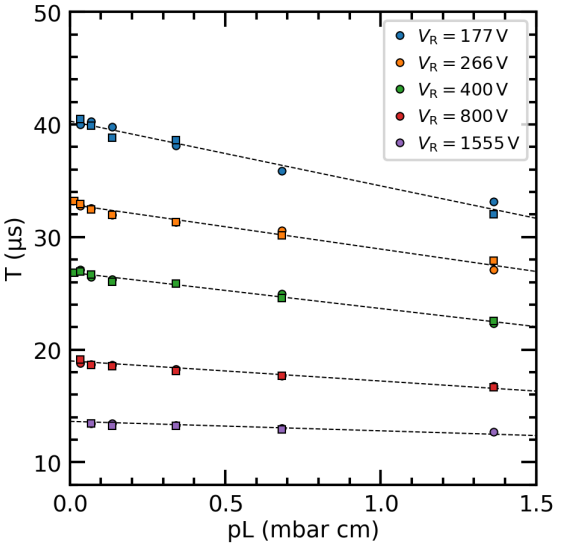

Figure 1.5: Peak positions of the differentiated current traces associated with the Sn^{1+} cutoffs as a function of the hydrogen pressure-length product pL for the two RFAs located at a flight distance of 0.68 m (RFA1 & RFA2; Table 1). The dashed lines represent linear fits, from which the stopping cross sections are extracted.

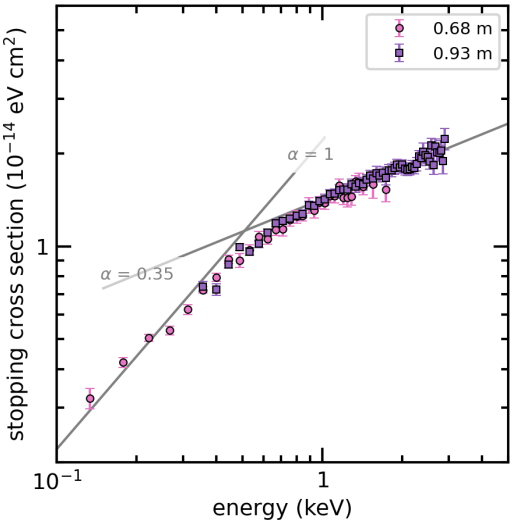

Figure 1.6: Experimental stopping cross sections derived from time-of-flight measurements at hydrogen pressures in the range of 2×10^{-4} to 2×10^{-2} mbar. The figure shows results obtained from the two RFAs located at 0.68 m (pink dots) and from the six RFAs at 0.93 m (purple squares).

decrease smoothly with H_2 pressure, from 18.7 µs at 5×10^{-4} mbar to 16.5 µs at 2×10^{-2} mbar. To exclude artificial dips arising from noise or signal fluctuations, a threshold level of approximately 10 % of the strongest dip is applied.

For five RFA barrier voltage settings, Fig. 1.5 shows the extracted peak positions as a function of the H_2 column density nL (represented here by the product of pressure and distance, pL). The underlying ToF traces were recorded with the two RFAs located at a distance of 0.68 m from the LPP. The slopes of linear fits to these data yield the ratio $\Delta T/nL$, which is required to calculate the stopping cross section (cf. Eq. (1.8)). The fits are performed with the intercept on the ToF axis fixed at T_{vac}. The same procedure was applied to the datasets obtained with the RFAs positioned at 0.93 m.

The resulting stopping cross sections are presented in Fig. 1.6. The datasets obtained at the two flight distances show very good agreement in the overlapping energy range between approximately 0.3 and 2 keV. The shorter flight distance allows extraction of stopping data at lower energies, while the longer distance provides improved sensitivity at higher energies. Together, the two configurations enable the determination of the stopping cross section over the full investigated energy range. The agreement between results obtained at two different flight distances (0.68 m and 0.93 m) demonstrates the consistency of the method and

confirms that the derived stopping cross sections are not sensitive to the specific detector geometry or the underlying ion energy distribution within the present uncertainties. Therefore, in the final comparison to other data (see Section 1.3), the average of the two datasets is used. For further discussion in Section 1.3, two power-law trend lines of the form $S \propto E^{\alpha}$ are included, with $\alpha = 1$ and $\alpha = 0.35$, representing the approximate low- and high-energy dependencies of the data, respectively.

1.2.3 Modeling of the stopping cross sections

The universal stopping code SRIM [19, 20] underestimates the experimental stopping cross sections (see Fig. 1.1). The three main reasons for this discrepancy are likely: (i) projectile ions are treated as neutral particles, (ii) the target H_2 molecule is approximated as two independent hydrogen atoms, and (iii) the use of the generic ZBL potential [19, 20].

Bartlett et al. [17] addressed this limitation by calculating the potential energy surface (PES) specific to the three-center nature of the $Sn^{1+} - H_2$ system, thereby explicitly taking the charge state of the Sn ion into account. In their approach, the PES was calculated using density functional theory (DFT) with the NWCHEM package [26]. A central ZBL potential was subsequently fitted to the radial average of the DFT interaction potential by tuning the effective target charge Z_2, for which a value of 2.76 was found to be optimal. Implementing this modified ZBL potential in conventional stopping codes such as SRIM resulted in stopping cross sections that are in good agreement with the experimental data of Abramenko et. al. [16].

Alongside the reported measurements, an in-house quasi-classical collision model, referred to as GIonS (Groningen Ion Stopping), was developed. In contrast to the effective central-potential approach of Bartlett et al. [17], GIonS retains the full non-central, molecular character of the interaction potential in the energy-loss calculations. The interaction potential is obtained from DFT calculations using the NWCHEM package, employing the range-separated hybrid functional rCAM-B3LYP [27]. Rather than constructing the potential on a uniform grid, the PES is sampled on two complementary sparse grids, referred to as the R- and C-grid. The C-grid covers a half-sphere centered on each hydrogen nucleus, spanning radial distances from 5 a.u. down to 0.3 a.u., and captures interactions in the vicinity of each nucleus. In contrast, the R-grid is a rectangular grid extending 5 a.u. perpendicular to the molecular axis and 1.7 a.u. parallel to it, thereby covering the full extent of the H_2 molecule. The C-grid is constructed using Clenshaw-Curtis nodes, while the R-grid employs Chebyshev nodes, allowing for efficient sampling and reducing interpolation artifacts such as Runge's phenomenon [28,

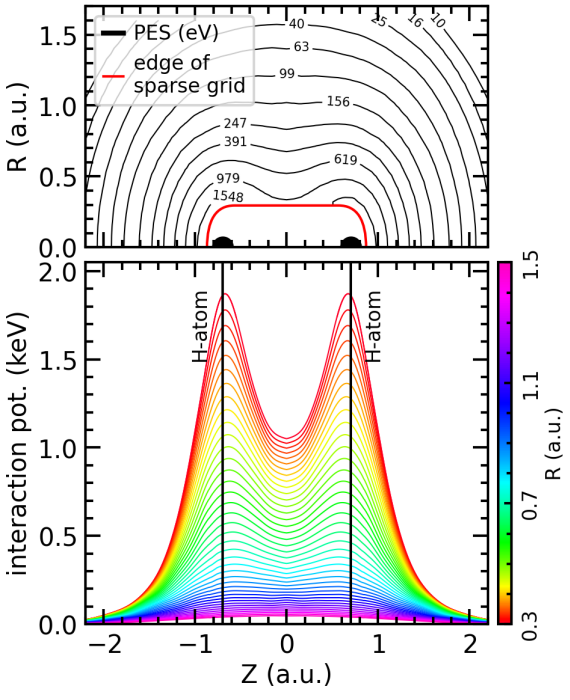

Figure 1.7: Potential energy surface (PES) of the $Sn^{1+} - H_2$ system used in the GIonS model. The top panel shows a contour plot of the PES (in eV) in the molecular plane, with the hydrogen atoms indicated by the black circles. The red curve marks the boundary between the C-grid and R-grid sparse sampling regions. The bottom panel shows 1D line-outs of the PES as a function of the projectile coordinate Z for different perpendicular distances R, indicated by the color scale. Vertical lines mark the positions of the hydrogen atoms.

29]. The discrete DFT data points obtained on both grids are combined into a single representation of the PES and interpolated using the Tasmanian sparse grid package [30, 31], yielding a continuous potential that can be evaluated at arbitrary positions in space. Contour plots and representative line-outs of the potential energy surface are shown in Fig. 1.7.

Energy-loss calculations are then performed for specific ion trajectories through the interpolated PES. For each trajectory, characterized by a given impact parameter (up to 40 a.u.), the interaction potential is evaluated along the ion path and integrated to obtain the energy loss. Due to the molecular nature of the target, these calculations are repeated for many orientations of the H_2 molecule, and the results are averaged accordingly. This procedure is carried out for projectile energies ranging from 0.1 to 5 keV.

1.3 Discussion

Fig. 1.8 compares our experimental and model stopping cross sections for keV Sn^{1+} ions in molecular hydrogen with all other available datasets. Similar to the experimental results of Abramenko et al. [16], our data exhibit a pronounced increase below 1 keV and a gradual leveling off above this energy. However, on an absolute scale, our measured stopping cross sections are on average about 20 % lower than those reported by Abramenko et al. Slightly above 1 keV, their data appear to make a step to somewhat higher values, which enlarges the difference between the two datasets to about 50 %. At the high-energy side, both datasets appear to approach a plateau.

The available model calculations do not provide a single unique description of the stopping cross section over the energy range from 0.1 to 5 keV. SRIM systematically underestimates the measured stopping cross sections across the full energy range. The modeling results of Bartlett et al. [17] show a clear improvement over SRIM. Instead of the common ZBL potential used by SRIM, Bartlett et al. used a modified ZBL potential fitted to potential energies obtained from DFT calculations. The best agreement with the DFT results was achieved by adjusting the effective nuclear charge Z_2 to 2.76. For collision energies above approximately 1 keV, this modified ZBL potential shows good agreement with the data of Abramenko et al.

More recently, Feng et al. [18] calculated potential energy surfaces for *neutral* Sn on H_2 using DFT, which they fitted with a Morse potential, which inherently includes an attractive potential-energy well. In this way, the model mimics the potential-energy well present in the ionic $Sn^{1+} - H_2$ system due to polarization effects. The resulting stopping cross sections based on the Morse potential exhibit a steeper increase with collision energy and do not yet level at higher energies. However, below 1 keV, they are in somewhat better agreement with the experimental data.

As described in Section 1.2.3, our GIonS model is likewise based on DFT-derived interaction potentials, but explicitly retains the molecular structure of H_2 in the calculation of stopping cross sections. Over the full energy range accessible in the present experiment (0.13–3 keV), the GIonS results are in very good agreement with our experimental stopping cross sections. Small deviations are observed around 0.7 keV and at the highest energies. The calculated cross sections lie between the upper ($Z_2 = 2.76$) and lower ($Z_2 = 1$) limits reported by Bartlett et al. [17].

More clearly than the data of Abramenko et al. [16] and previous calculations, both our experimental and modeled results show a smooth transition in the energy dependence of the stopping cross section, from an approximately E^1 scaling to

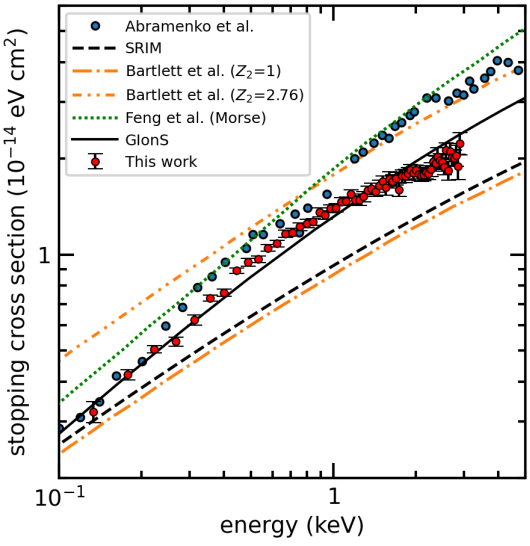

Figure 1.8: Stopping cross sections for Sn^{1+} ions in H_2 as a function of impact energy. The present experimental results (red symbols) are compared to calculations from the GIonS model (solid black line), as well as to literature data from Abramenko et al. [16] (blue symbols), Bartlett et al. [17] (dash-dotted and dash-double-dotted lines), Feng et al. [18] (dotted line), and SRIM (black dashed line).

an $E^{0.35}$ scaling. This indicates that the investigated energy range encompasses the transition from one collision regime to another (see also Fig. 1.8).

At collision energies well below 1 keV/u, the system remains deep in the nuclear stopping regime (see, e.g., reviews [32–35]. In this low-energy limit, the stopping cross section scales linearly with collision energy, which is characteristic of hard-sphere (or billiard-ball-type) elastic collisions. This hard-sphere approximation holds for energies where the distance of closest approach is larger than the (Firsov) screening length a_F of the appropriate screened Coulomb potential. In atomic units, this length is given by $a_F = 0.8853(\sqrt{Z_1} + \sqrt{Z_2})^{-2/3}$, where Z_1 and Z_2 denote the nuclear charge state of the projectile and target atom, respectively. For the present system, $a_F \approx 0.25$ a.u.

Our measurements show a transition from hard-sphere behavior at collision energies of approximately 600 eV (cf. Fig. 1.6). According to the potential energy surface shown in the top panel of Fig. 1.7, 600 eV facilitates a distance of closest approach of about 0.5 a.u., i.e., roughly twice the screening length a_F. However, at these low energies, one might assume that the inner-shell electrons of Sn efficiently act as inert spectators (fully shielding the Sn nucleus), such that only the outer $5s^2 5p$ electrons contribute to the interaction. This would imply

an effective nuclear charge state of $Z_1 = 4$ instead of 50, increasing a_F from approximately 0.25 to nearly 0.45 a.u., thereby bringing the two length scales into closer agreement.

At higher energies, beyond the hard-sphere regime, Lindhard and co-workers [36, 37] derived a general description of nuclear stopping up to the Rutherford regime, where nuclear stopping cross sections decrease and electronic stopping takes over. Just above the hard-sphere regime, where Thomas-Fermi and Moliere potentials are quite applicable, the stopping cross sections are predicted to scale as $E^{1/3}$. This is remarkably close to the exponent of 0.35 that we obtained from our measurements (see Fig. 1.6).

1.4 Conclusion

In this work, we have investigated the stopping of slow (0.13–3 keV) Sn^{1+} ions in H_2 gas by combining time-of-flight measurements with energy selection using retarding field analyzers. From the analysis of the pressure-dependent shifts in the time-of-flight spectra, absolute stopping cross sections were determined over more than an order of magnitude in ion energy.

The measured stopping cross sections show excellent agreement with the results of our GIonS semi-classical collision model. Similar to the work of Bartlett et al. [17], the model is based on DFT-calculated interaction potentials. While other DFT-based approaches [17, 18] fit centrosymmetric potentials to DFT potential energy surfaces, GIonS directly retains the full DFT PES in the calculation of stopping cross sections. The energy dependence of both the measured and calculated stopping cross sections agrees with available literature data in the nuclear stopping regime.

Our results confirm that the commonly used SRIM package systematically underestimates stopping for slow, heavy ions in molecular gases at low energies. At the same time, our cross sections are more than 40 % lower than the only other experimental dataset by Abramenko et al. [16] at energies above 1 keV, whereas good agreement is found at the lowest energies (0.13–0.25 keV). Since the penetration depth of Sn^{1+} ions in an H_2 stopping gas exponentially depends on the stopping cross sections, an uncertainty of 20 % or less is desirable for reliable predictive modeling of the stopping of Sn ions expelled from EUV sources.

These discrepancies highlight the need for further experimental and theoretical work. In particular, given the broad energy distributions of ions escaping EUV source plasmas and the uncertainties in the exact composition of the gas surrounding the EUV plasma, experiments using monoenergetic Sn ion beams may provide a more controlled route toward improved accuracy.

Acknowledgments

This work was conducted as part of the research program of the Advanced Research Center for Nanolithography (ARCNL), a public-private partnership of the University of Amsterdam (UvA), Vrije Universiteit Amsterdam, University of Groningen (RuG), the Dutch Research Council (NWO) and the semiconductor equipment manufacturer ASML. This publication is part of the project ARIES with file number 20152 of the research programme VENI which is (partly) financed by the Dutch Research Council under an NWO grant.

Appendix

The geometrical configuration of the retarding field analyzers (RFAs) used in the experiments are specified in this Appendix. Eight RFAs are positioned at different observation angles with respect to the incident laser direction. Two detectors are placed in the backward direction at a flight distance of 0.68 m, while the remaining six RFAs are positioned at a distance of 0.93 m and cover forward and intermediate emission angles. Each RFA is mounted on a fixed vacuum-chamber port, defining its observation angle relative to the laser axis. The detector acceptance $\Delta\Omega$ is determined by its aperture and distance from the source. Table 1 summarizes the detector distances and angular positions in terms of the angle with respect to the laser axis (α), elevation (β), and azimuth (γ).

RFA	d (m)	$\alpha(^\circ)$	$\beta(^\circ)$	$\gamma(^\circ)$	$\Delta\Omega$(μsr)
1	0.68	139	30	150	44
2	0.68	150	30	180	44
3	0.93	30	30	0	23
4	0.93	41	-30	30	23
5	0.93	64	30	60	23
6	0.93	64	30	300	23
7	0.93	90	30	90	23
8	0.93	120	30	120	23

Table 1: Geometrical configuration of the retarding field analyzers used in the present experiment. The table lists the detector positions in terms of their distance from the plasma source and their angular orientation with respect to the laser propagation axis, given by the polar angle α, elevation β, and azimuth γ.

References

[1] V. Bakshi, *EUV lithography* (SPIE Press, 2018).

[2] I. Fomenkov, D. Brandt, A. Ershov, A. Schafgans, Y. Tao, G. Vaschenko, S. Rokitski, M. Kats, M. Vargas, M. Purvis, R. Rafac, B. L. Fontaine, S. D. Dea, A. LaForge, J. Stewart, S. Chang, M. Graham, D. Riggs, T. Taylor, M. Abraham, and D. Brown, "Light sources for high-volume manufacturing EUV lithography: technology, performance, and power scaling", Adv. Opt. Techn. **6**, 173–186 (2017).

[3] O. O. Versolato, J. Sheil, S. Witte, W. Ubachs, and R. Hoekstra, "Microdroplet-tin plasma sources of EUV radiation driven by solid-state-lasers", J. Opt. **24**, 054014 (2022).

[4] G. O'Sullivan, B. Li, R. D'Arcy, P. Dunne, P. Hayden, D. Kilbane, T. McCormack, H. Ohashi, F. O'Reilly, P. Sheridan, E. Sokell, C. Suzuki, and T. Higashiguchi, "Spectroscopy of highly charged ions and its relevance to EUV and soft X-ray source development", J. Phys. B: At. Mol. Opt. Phys. **48**, 144025 (2015).

[5] S. Fujioka, H. Nishimura, K. Nishihara, A. Sasaki, A. Sunahara, T. Okuno, N. Ueda, T. Ando, Y. Tao, Y. Shimada, K. Hashimoto, M. Yamaura, K. Shigemori, M. Nakai, K. Nagai, T. Norimatsu, T. Nishikawa, N. Miyanaga, Y. Izawa, and K. Mima, "Opacity effect on extreme ultraviolet radiation from laser-produced tin plasmas", Phys. Rev. Lett. **95**, 1–4 (2005).

[6] J. Colgan, D. Kilcrease, J. Abdallah, M. Sherrill, C. Fontes, P. Hakel, and G. Armstrong, "Atomic structure considerations for the low-temperature opacity of sn", High Energy Density Phys. **23**, 133–137 (2017).

[7] F. Torretti, J. Sheil, R. Schupp, M. M. Basko, M. Bayraktar, R. A. Meijer, S. Witte, W. Ubachs, R. Hoekstra, O. O. Versolato, A. J. Neukirch, and J. Colgan, "Prominent radiative contributions from multiply-excited states in laser-produced tin plasma for nanolithography", Nat. Commun. **11**, 1–8 (2020).

[8] L. Poirier, A. C. Lassise, R. Hoekstra, J. Sheil, and O. O. Versolato, "Laser-intensity dependence of ion emission from Nd:YAG-laser-produced plasma expanding into vacuum", Phys. Plasmas **30**, 083505 (2023).

[9] S. S. Harilal, B. O'Shay, Y. Tao, and M. S. Tillack, "Ambient gas effects on the dynamics of laser-produced tin plume expansion", J. Appl. Phys. **99**, 083303 (2006).

[10] S. S. Harilal, B. O'Shay, Y. Tao, and M. S. Tillack, "Ion debris mitigation from tin plasma using ambient gas, magnetic field and combined effects", Appl. Phys. B **86**, 547–553 (2007).

[11] D. Bleiner and T. Lippert, "Stopping power of a buffer gas for laser plasma debris mitigation", J. Appl. Phys. **106**, 123301 (2009).

[12] T. Wu, X. Wang, H. Lu, and P. Lu, "Debris mitigation power of various buffer gases for CO_2 laser produced tin plasmas", J. Phys. D: Appl. Phys. **45**, 475203 (2012).

[13] S. Rai, K. I. Bijlsma, L. Poirier, E. de Wit, L. Assink, A. C. Lassise, I. Rabadan, L. Méndez, J. Sheil, O. O. Versolato, and R. Hoekstra, "Evidence of production of keV Sn^+ ions in the H_2 buffer gas surrounding a Sn-plasma EUV source", Plasma Sources Sci. Technol. **32**, 035006 (2023).

[14] K. Bijlsma, L. Oltra, E. de Wit, L. Assink, I. Rabadan, L. Méndez, and R. Hoekstra, "Electron capture from molecular hydrogen by metastable Sn^{2+*} ions", Atoms **12**, 9 (2024).

[15] L. Oltra, L. Méndez, I. Rabadán, K. I. Bijlsma, E. de Wit, and R. Hoekstra, "Sequential synchronous mechanism for double-electron capture: insights into unforeseen large cross sections in low-energy $Sn^3 + H_2$ collisions", Phys. Rev. Lett. **134**, 093002 (2024).

[16] D. B. Abramenko, M. V. Spirodonov, P. V. Krainov, V. M. Krivtsun, D. I. Astakhov, V. V. Medvedev, M. van Kampen, D. Smeets, and K. N. Koshelev, "Measurements of hydrogen gas stopping efficiency for tin ions from laser-produced plasma", Appl. Phys. Lett. **112**, 164102 (2018).

[17] N. Bartlett, A. Herschberg, J. Crouse, T. Dallal, J. Nuttal, J. Stahl, N. Braaksma, and D. Ruzic, "Elastic scattering cross sections and transport of tin ions in extreme ultraviolet lithography sources", Phys. Scr. **99**, 065411 (2024).

[18] X. Feng, Y. Song, Y. Ma, and B. Li, "DFT-based interatomic potentials for hydrogen-metal systems: improved stopping power modeling", Nucl. Instrum. and Methods Phys. Res. B **572**, 165999 (2026).

[19] J. F. Ziegler, J. P. Biersack, and M. D. Ziegler, "SRIM – The stopping and range of ions in matter", in (Ion Implantation Press, 2008).

[20] J. F. Ziegler, M. D. Ziegler, and J. P. Biersack, "SRIM – The stopping and range of ions in matter (2010)", Nucl. Instrum. and Methods Phys. Res. B **268**, 1818–1823 (2010).

[21] L. Poirier, D. J. Hemminga, A. C. Lassise, L. Assink, R. Hoekstra, J. Sheil, and O. O. Versolato, "Strongly anisotropic ion emission in the expansion of Nd:YAG-laser-produced plasma", Phys. Plasmas **29**, 123102 (2022).

[22] G. Sidenius, "Systematic stopping cross-section measurements with low-energy ions in gases", Mat. Fys. Dan. Vid. Selsk **19**, 1–32 (1974).

[23] P. Hvelplund, "Energy loss and straggling of 100–500-keV $_{90}$Th, $_{82}$Pb, $_{80}$Hg, and $_{64}$Gd in H_2", Phys. Rev. A **11**, 1921 (1975).

[24] V. Martini, "Energy loss measurements of keV-ions in gases by time-of-flight spectroscopy", Nucl. Instr. and Meth. **124**, 119–124 (1975).

[25] K. Freitag, D. Reschke, and E. Geyer, "Stopping power measurements for low energy ions in gases by time-of-flight spectroscopy", Nucl. Instrum. and Methods Phys. Res. B **27**, 344–352 (1987).

[26] E. Aprà, E. J. Bylaska, W. A. de Jong, N. Govind, K. Kowalski, T. P. Straatsma, M. Valiev, H. J. J. van Dam, Y. Alexeev, J. Anchell, V. Anisimov, F. W. Aquino, R. Atta-Fynn, J. Autschbach, N. P. Bauman, J. C. Becca, D. E. Bernholdt, K. Bhaskaran-Nair, S. Bogatko, P. Borowski, J. Boschen, J. Brabec, A. Bruner, E. Cauët, Y. Chen, G. N. Chuev, C. J. Cramer, J. Daily, M. J. O. Deegan, T. H. Dunning Jr., M. Dupuis, K. G. Dyall, G. I. Fann, S. A. Fischer, A. Fonari, H. Früchtl, L. Gagliardi, J. Garza, N. Gawande, S. Ghosh, K. Glaesemann, A. W. Götz, J. Hammond, V. Helms, E. D. Hermes, K. Hirao, S. Hirata, M. Jacquelin, L. Jensen, B. G. Johnson, H. Jónsson, R. A. Kendall, M. Klemm, R. Kobayashi, V. Konkov, S. Krishnamoorthy, M. Krishnan, Z. Lin, R. D. Lins, R. J. Littlefield, A. J. Logsdail, K. Lopata, W. Ma, A. V. Marenich, J. Martin del Campo, D. Mejia-Rodriguez, J. E. Moore, J. M. Mullin, T. Nakajima, D. R. Nascimento, J. A. Nichols, P. J. Nichols, J. Nieplocha, A. Otero-de-la-Roza, B. Palmer, A. Panyala, T. Pirojsirikul, B. Peng, R. Peverati, J. Pittner, L. Pollack, R. M. Richard, P. Sadayappan, G. C. Schatz, W. A. Shelton, D. W. Silverstein, D. M. A. Smith, T. A. Soares, D. Song, M. Swart, H. L. Taylor, G. S. Thomas, V. Tipparaju, D. G. Truhlar, K. Tsemekhman, T. Van Voorhis, Á. Vázquez-Mayagoitia, P. Verma, O. Villa, A. Vishnu, K. D. Vogiatzis, D. Wang, J. H. Weare, M. J. Williamson, T. L. Windus, K. Woliński, A. T. Wong, Q. Wu, C. Yang, Q. Yu, M. Zacharias, Z. Zhang, Y. Zhao, and R. J. Harrison, "NWChem: Past, present and future", J. Chem. Phys. **152**, 184102 (2020).

[27] A. J. Cohen, P. Mori-Sánchez, and W. Yang, "Development of exchange-correlation functionals with minimal many-electron self-interaction error", J. Chem. Phys. **126**, 191109 (2007).

[28] J. Stoer and R. Bulirsch, *Introduction to numerical analysis* (Springer, 2002).

[29] L. N. Trefethen, *Approximation theory and approximation practice* (SIAM, 2013).

[30] M. Stoyanov, D. Lebrun-Grandie, J. Burkardt, and D. Munster, *Tasmanian*, `https://github.com/ORNL/Tasmanian`, Version 9, 2013.

[31] M. Stoyanov, *User manual: tasmanian sparse grids*, tech. rep. ORNL/TM-2015/596 (Oak Ridge National Laboratory, One Bethel Valley Road, Oak Ridge, TN, 2015).

[32] K. B. Winterbon, P. Sigmund, and J. B. Sanders, "Spatial distribution of energy deposited atomic particles in elastic collisions", K. Dan. Vidensk. Selsk. Mat. Fys. Medd. **37**, 5–73 (1970).

[33] W. Eckstein, *Computer simulation of ion-solid interactions* (Springer, 1991).

[34] R. Smith, *Atomic and ion collisions in solids and at surfaces: theory, simulations and applications* (Cambridge University Press, 1997).

[35] P. Sigmund, *Stopping of heavy ions: a theoretical approach* (Springer, 2004).

[36] J. Lindhard, M. Scharff, and H. E. Schiott, "Range concepts and heavy ion ranges (Notes on atomic collisions, II)", Mat. Fys. Medd. Dan. Vid. Selsk. **33**, 1–42 (1963).

[37] J. Lindhard, V. Nielsen, and M. Scharff, "Approximation method in classical scattering by screened Coulomb fields (Notes on atomic collisions, I)", Mat. Fys. Medd. Dan. Vid. Selsk. **36**, 1–32 (1968).

CHAPTER 2

On the absence of a prominent single-collision peak in keV heavy-ion scattering off a polycrystalline Ru surface

Luc Assink, Johannes Brötzner, Christian Cupak,
Mart Salverda, Harry Jonkman, Oscar Versolato,
Richard Wilhelm, and Ronnie Hoekstra

Nucl. Instrum. and Methods Phys. Res. B. **554**, 165442 (2024)

Abstract

In a joint experimental and modeling effort, we have studied 15 keV Ar^{2+}, Kr^{2+}, and Xe^{2+} projectiles scattering off a polycrystalline Ru surface to assess the possible role of surface roughness in the apparent near-absence of the single-collision (SC) peak for Xe, the heaviest of the ions. The surface roughness of the Ru sample was determined by atomic force microscopy (AFM). The AFM image is used as input to simulations by means of the ray-tracing code SPRAY. The observed spectra display a significant SC peak in the energy distributions of reflected Ar and Kr ions, which is not the case for Xe. The energy spectrum produced by the reflection of Xe and recoiled Ru ions closely corresponds to the results obtained from our SPRAY simulations. It is evident that surface roughness plays a crucial role in the visibility of the SC peak. From simulations for different target roughnesses, it is clear that a concentrated distribution of inclination angles centered around 2° effectively reduces the intensity of the single-collision peak for Xe ion scattering. The presence of a distinct SC peak for Ar and Kr ions, unlike Xe ions, supports the notion that the absence of a prominent SC peak in Xe ion scattering is not primarily due to geometric blocking of trajectories by surface roughness. This suggests that for slow, heavy ions like Xe, scattering effects arising from the nearest neighbors to the binary collision partner are significant and should be carefully examined.

2.1 Introduction

To model what happens when keV ions impact on a surface, binary collision codes like SRIM [1, 2] are typically used. The output of these codes has been extensively tested [3–5] for the reflection of light ions at these low energies, as it finds an application in analysis methods such as low-energy ion scattering (LEIS) [6–8]. However, data on the interaction between keV heavy ion scattering and a heavy surface appear to be lacking. Recently, an extensive systematic study of the interaction of Sn ions on the transition metals Mo and Ru was performed [9]. While the experimental data did not show a clear sign of a single binary collision (SC) peak on top of the broad multiple-scattering distribution, all tested binary codes did show the peak, though intensities varied between different simulation packages. Many options were considered to explain the absence or extensive smearing out of the SC peak, such that it is no longer visible on top of the multiple-scattering background.

A possible explanation not rigorously tested yet is surface roughness. In this joint experimental and modeling study, we investigate whether surface roughness may be the cause of the apparent absence of the SC peak. If roughness-induced blocking of ion trajectories would suppress the SC peak for specific scattering angles, the choice of projectile should not matter. To test this, we considered noble gas projectile ions, i.e., Ar, Kr, and Xe, which substitute for Sn ions used in our previous work [9]. Xe ions are more conveniently produced than Sn ions and in higher beam currents. Kinetic energy distributions of reflected Ar, Kr, and Xe particles are measured with an electrostatic analyzer. The results are discussed in comparison to SPRAY simulations. The SPRAY code is a ray-tracing code that explicitly includes surface roughness. The surface roughness is extracted from atomic force microscopy (AFM) images of the surface. The collisions are described by the conventional binary collision approximation (BCA).

Using the comparison of SPRAY simulations and experimental data together with the spectral differences between the results of Ar, Kr, and Xe ions, it is argued that it is unlikely that the absence of the SC peak for heavy projectiles such as Xe (and Sn) is primarily a result of geometrical blocking of SC trajectories due to roughness. In addition, the remarkable large fraction of energetic Ru recoils stemming from binary single collision events is discussed.

2.2 Research methods

2.2.1 Experimental setup

The primary beams of 15 keV Ar^{2+}, Kr^{2+}, and Xe^{2+} are extracted from the 14-GHz Electron Cyclotron Resonance (ECR) ion source (SUPERNANOGAN, Pantechnik) at the ZERNIKELEIF ion beam facility at the University of Groningen. An 110° analyzing magnet with a resolution of $\sim 0.5\%$ assures the use of monoisotopic ion beams: ^{40}Ar, ^{84}Kr, and ^{132}Xe. By means of three magnetic quadrupole triplets, the ion beam is transported 15 m downstream. For final mass-over-charge clean up, a 45° dipole magnet is placed 2 m in front of the collision chamber. Since the main components of the setup are presented in detail in previous papers [10–12], only a brief description of the setup is given here.

The polycrystalline Ru target (Surface Preparation Labs, Zaandam, The Netherlands) is attached to the sample holder of a five-axes manipulator mounted on top of a μ-metal chamber kept at a base pressure of 1×10^{-10} mbar. By rotating the target around its axis, the angle of incidence with respect to the surface plane, ψ, can be set with a resolution of 0.1°. In the present experiments, the incidence angle is kept constant at 15°.

The rotatable high-precision electrostatic analyzer (ESA), which measures ions only, is used at a scatter angle of $\theta = 40°$. The ESA has an opening diaphragm of 0.4 mm, positioned 75 mm from the sample, which allows for a solid angle $\Delta\Omega$ of 2.2×10^{-5} sr at the center of the target. Each ESA spectrum presented here is corrected for the beam current, the solid angle, the increasing energy bin size resulting from the spectrometer's fixed $\Delta E/E$ resolution (0.5 % FWHM), and the energy-dependent detection efficiency of the microchannel plate. For the latter correction, the empirical detection efficiency curves determined by Krems et al. [13] are used. Given the energy range of reflected Ar, Kr, and Xe ions, i.e., approximately $6 - 10$ keV, only a small correction for the lowest-energy Xe ions of at most ~ 20 % is needed to be applied.

To assess the roughness of the Ru sample, the sample was taken out of the collision chamber and transferred to a Bruker Dimension ICON Atomic Force Microscope. A typical AFM topographical image of 4 µm^2 of the Ru surface after Ar sputtering and heat treatment is shown in Fig. 2.1. Outside of the deeper troughs, which are remnants of the original surface polishing, the sample locally has a root mean square (RMS) roughness of 0.7 nm. This RMS roughness is taken over an area of 0.3 µm^2. The sample is oriented such that the troughs are aligned along the detector plane. This way, projectile ions that impinge on the sidewalls of the troughs are scattered out of the detector plane, and thus do not contribute to the experimental results. It is to be realized that for the treated

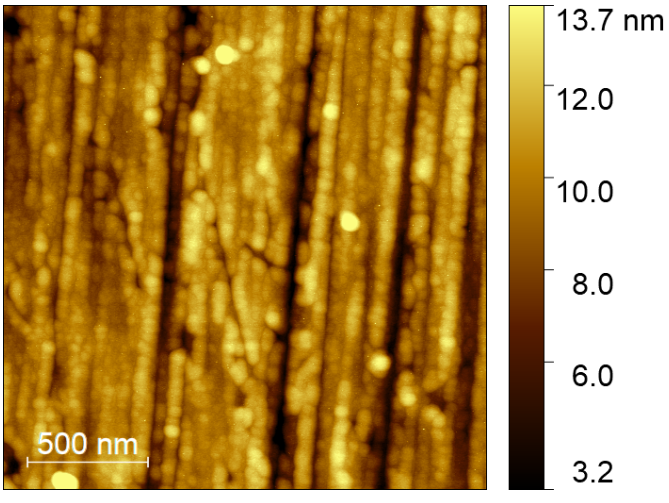

Figure 2.1: A typical $2 \times 2\,\mu m^2$ AFM topography image of the polycrystalline Ru surface being exposed to Ar ion beam cleaning and heat treatment. The 10-nm height scale is shown by the color bar on the right.

sample, shown in Fig. 2.1, the side walls are inclined to the surface plane by at maximum 5° to 10° (see also Fig. 2.3).

2.2.2 Binary collision approximation

For a binary collision of a projectile of mass m_p with energy E_0 on a target atom of mass m_t the final energy E_f after scattering over an angle θ is given by:

$$E_f = \left(\frac{\cos(\theta) \pm \sqrt{(m_t/m_p)^2 - \sin^2(\theta)}}{1 + m_t/m_p} \right)^2 E_0. \tag{2.1}$$

The energy of a recoiled target particle E_{rec} detected at the same scattering angle θ is given by:

$$E_{rec} = \frac{4 m_t m_p}{(m_t + m_p)^2} \cos^2(\theta)\ E_0. \tag{2.2}$$

The $\pm$ sign in Eq. (2.1) takes care of the two options for a heavier particle scattering on a lighter target atom. Here, this is relevant to the Xe – Ru collision system. The projectile being heavier than the target atom also implies that there is a maximum scattering angle that can be reached. The maximum scattering angle is then calculated by $\theta_{max} = \arcsin(m_t/m_p)$, which yields for ^{132}Xe projectiles on Ru a maximum angle of approximately 50°, assuming a weighted average mass of Ru of 101.1 mass units.

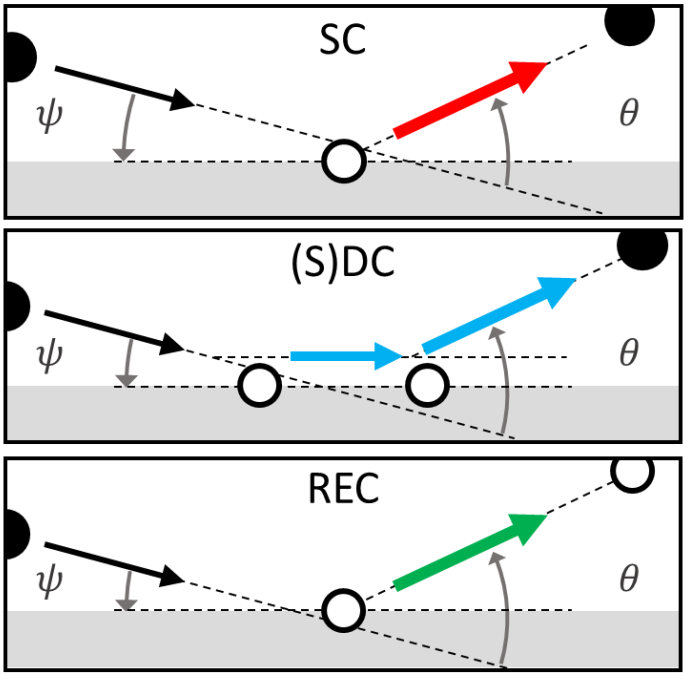

Figure 2.2: Visualization and color coding of different collisional events leading to the detection of a particle at a scattering angle θ. For a given projectile impinging under an incidence angle ψ, three types of collision processes are considered: top panel - single collisions (SC), middle panel - (symmetric) double collisions ((S)DC), and bottom panel - primary target recoils (REC). In all other figures, the positions of SC, (S)DC, and REC events will be indicated by red, blue, and green bars, respectively.

In the comparison between experiments and model simulations, we will mainly focus on the three different types of scattering events, which are depicted in Fig. 2.2.

- Single collision (SC): the projectile is deflected over an angle θ after colliding only once with a target atom. If roughness would geometrically block SC trajectories from reaching the detector, it would affect all ions (Ar, Kr, and Xe) alike.

- Double collision (DC): the projectile is deflected over an angle θ after two consecutive collisions with a target atom. From Eq. (2.1) it follows that, in total, less energy is lost by the projectile when it scatters twice, thus if $\theta_1 + \theta_2 = \theta$, with θ_1 and θ_2 the scattering angles of the first and second collision, respectively. The least energy is lost in symmetric double collisions (SDC), i.e. $\theta_1 = \theta_2 = \theta/2$. However, as can be inferred from Fig. 2.2, symmetric double collisions can only occur if the incidence angle $\psi > \theta/2$. Otherwise, the particle would already be scattered away from the surface after the first scattering event. No symmetric double collisions will take place unless the target is locally rough.

- Primary target recoils (REC): an energetic target atom knocked out of the sample by the projectile in a single collision. In order to do so, the projectile should hit the target atom from below the surface. The likelihood to do so depends on the incidence angle ψ and once again on the local roughness of the surface. At the relatively small angle of incidence of $\psi = 15^\circ$ used here, roughness would likely enhance the production of primary target recoils.

In the results discussed in the next sections, the energy ranges in which the three types of collision events are expected to show up are indicated by shaded bands in the same color code as used in Fig. 2.2: SC - red, (S)DC - blue, and REC - green. The width of these bands is determined by the different masses of the Ru isotopes, and an angular scattering range of $\pm 0.5^\circ$.

2.2.3 SPRAY simulations

The simulations described in this paper have been performed using the SPRAY code. As this code is explained in detail in [14], only a brief description of the working principles of the simulation package is given here. Where most conventional BCA codes assume a perfectly flat target, only a few include sample roughness [14–16]. The SPRAY code is a ray-tracing simulation code that is especially developed to study target sputtering and re-deposition in case of rough surfaces. SPRAY is based on a repository of energy-dependent scattering angle distributions pre-calculated with SDTrimSP [17] for the projectile target combination of interest. Thus, intrinsic features of SDTrimSP in describing the binary collision are part of SPRAY as well. In the present work we used the option of SDTrimSP to include weak collisions along the projectile trajectory. This explicit inclusion of nearest neighbor interactions upgrades the description from a pure binary case to the integral scattering off a small surface area. By triangulating a surface, the roughness in SPRAY is described as locally tilted surfaces. The code can incorporate the actual surface roughness of an experimental sample by importing an AFM image of that surface. This is in contrast to codes like TRI3DYN and SDTrimSP-3D, which build their surfaces as cubic voxels, leading to untilted flat surfaces on the size scale of the voxel dimensions. Instead of using the RMS value of the target roughness, SPRAY describes the surface roughness by means of the surface inclination angle distribution (SIAD) of flat surface patches (see inset Fig. 2.3). This kind of representation of surface roughness was shown to be more appropriate for modeling ion sputtering of rough targets [14].

In this paper, SPRAY simulations are performed for three targets, each with different sample roughness. Besides the 'treated' target as shown in Fig. 2.1, two other test targets are used. One of these targets is generated to be artificially flat. It represents the ideal scenario without any kind of roughness. As no roughness is present, the SPRAY simulations do not differ from conventional BCA codes. The roughest-surface scenario is based on an AFM image of the original Ru target before any kind of treatment. This target is referred to as the 'untreated' target. All the experimental results presented in this work were taken using the 'treated' target.

Fig. 2.3 compares the surface inclination angle distribution of the treated target (green) and untreated target (red). It is of note that the distribution of inclination angles of the treated target is limited to a few degrees only. Nevertheless, as will be shown, this suffices to affect the energy distributions of scattered projectiles. Simulations are performed for 15 keV Ar, Kr, and Xe beams incident at 15° on the flat, treated, and untreated Ru surface. The output of each of these simulations contains both reflected and recoiled particles. For an

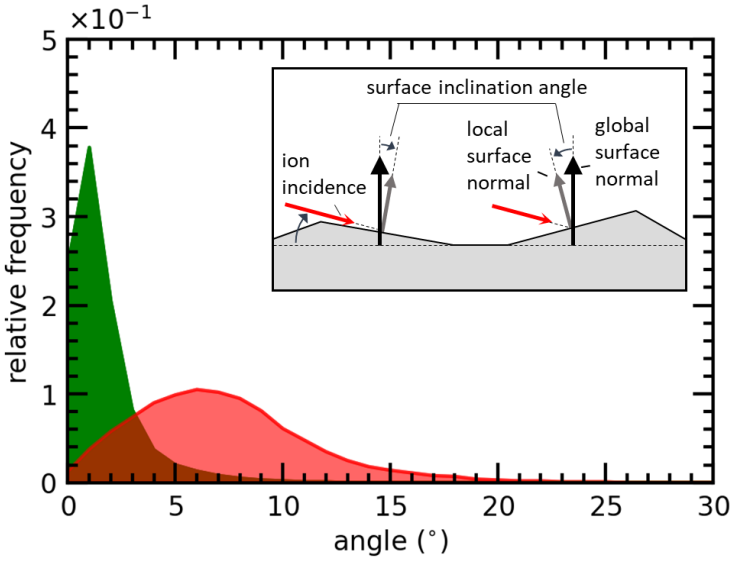

Figure 2.3: The relative frequency of the absolute value of the surface inclination angle with respect to the global surface normal for the treated (green) and untreated (red) cases of surface roughness.

adequate comparison with enough statistics to the experiments on the treated target, the output of the simulations is binned in angular scattering and azimuthal bins of $\pm 0.5^\circ$ and $\pm 4^\circ$, respectively, and an energy bin of 150 eV. The size of the angular scattering and azimuthal bins yield a solid angle $\Delta\Omega$ of 2.2×10^{-3} sr.

2.3 Results and discussion

2.3.1 Experimental results

Fig. 2.4 shows measured ion energy spectra taken with the ESA for 15 keV Ar^{2+} (left), Kr^{2+} (middle), and Xe^{2+} (right) ions colliding on the 'treated' Ru target at a scattering geometry of $(\psi, \theta) = (15^\circ, 40^\circ)$. The following general observations can be made on the contributions of SC, (S)DC, and REC to the spectrum.

Single collisions of Ar, Kr, and Xe projectiles

Looking at the energy distributions of the reflected ions, a prominent SC peak is seen for the 15 keV Ar and Kr projectiles. For the 15 keV Xe projectiles, a broad structure appears in the ion spectrum at and slightly above the SC-peak energy. The latter is likely due to hetero-atomic double collisions on O and Ru atoms.

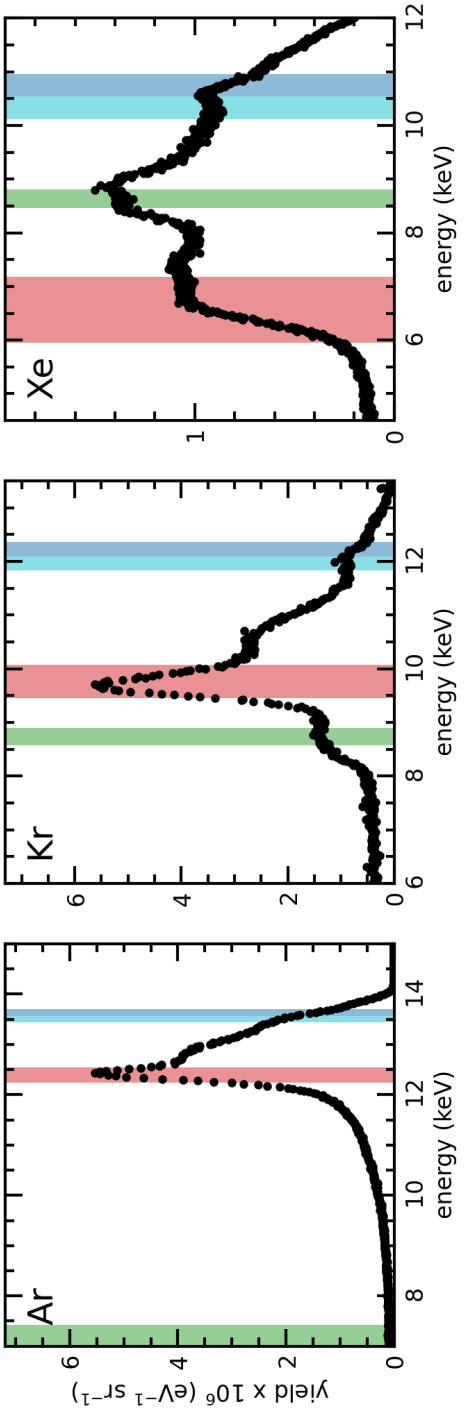

Figure 2.4: Ion energy distributions of reflected projectile and recoiled target ions for 15 keV (left column) Ar^{2+}, (middle column) Kr^{2+}, and (right column) Xe^{2+} ions colliding on a Ru surface at a scattering geometry of $(\psi, \theta) = (15°, 40°)$. The expected energy range of the peak due to single collisions (red), double collisions (blue) and recoil (green) events are indicated by the shaded areas.

The maximum scattering angle of Xe on O is only 7°. For additional scattering on O over 2°, a peak would appear at $\sim 7.4\,\mathrm{keV}$ in the ESA spectrum of Xe. The fact that the SC peaks are dominantly present for Ar and Kr ions indicates that roughness of the surface in our case does not lead to significant geometrical blocking of SC trajectories. For Xe ions, SC events show up in the spectrum but no clear SC peak stands out in the spectrum. This may in part be explained because of overlap with ions stemming from hetero-atomic double collisions and with a possible overlapping low-energy tail of Ru recoils. On top of that, the ion spectrum is measured at a scattering angle of $\theta = 40°$, which is not far below the maximum scattering angle for Xe on Ru of 50°. Thus, the cross section for scattering over 40° is expected to be small.

Double collisions of Ar, Kr, and Xe projectiles

The exact energies of the DC peak in the ESA spectra of, in particular, Kr and Xe underline the conclusion drawn from the SC results that the surface roughness does not play an appreciable part. The DC peaks fall just below the calculated energies of the symmetric double-collision peak marked by the dark blue bands in Fig. 2.4. For a scatter angle of $\theta = 40°$, an SDC peak requires two consecutive collisions of 20° to take place. At an incoming angle of $\psi = 15°$, this is not possible unless local surface inclination in the surface exist (local surface roughness). For a locally flat surface, the DC events remaining the highest energy would show up for an angular combination of 15° and 25° scattering angles. The energy band associated with consecutive 15° and 25° scattering is indicated by the light blue bands in Fig. 2.4. It is indeed within the light blue bands that the DC peak primarily shows up.

Primary Ru recoils

Another interesting observation comes from the contribution of the primary Ru recoils (green-shaded areas). While the small fraction of Ru recoils does not interfere with the energy distribution of the reflected Ar ions, the larger contributions of Ru recoils for the heavier projectiles start to overlap with the energy distributions of the reflected ions. In particular for Xe: the distribution of the primary Ru recoils is in between the expected SC and (S)DC position, and thus, as mentioned above, a low-energy tail of primary Ru recoils may influence the shape of the energy spectrum near the position of the SC scattering events between 6 and 7 keV (see Fig. 2.4).

The presence of a primary recoil peak for Xe impact is in itself evidence that SC events take place. Primary recoils are the most energetic target particles

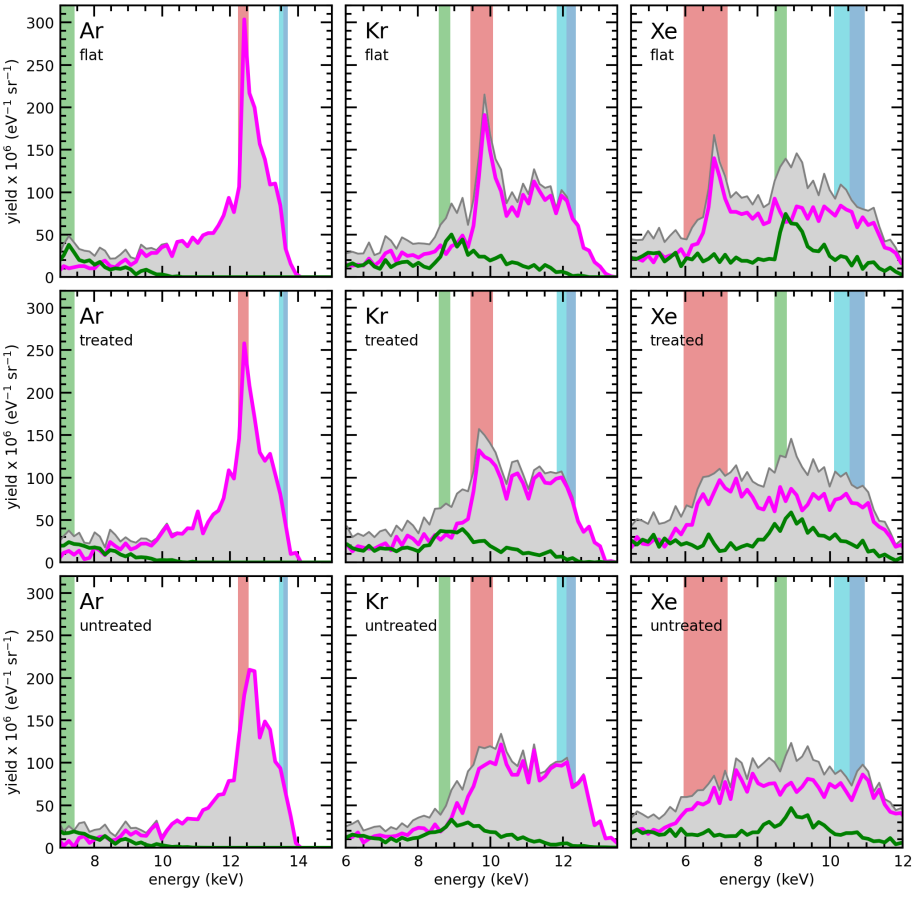

Figure 2.5: Compilation of simulated energy distributions of reflected (magenta line) and recoiled (dark green line) particles for 15 keV Ar (left), Kr (middle), and Xe (right) projectiles colliding on Ru targets of different surface roughness: flat (top row), treated (middle row), and untreated (bottom row). For each case, the sum of the reflected and recoiled particles is shown by the gray shaded spectrum.

knocked out of the sample by the projectile in a single collision. Contrary to single scattering, the projectile ions hit the target atom from below the surface. To knock out a Ru target atom over an angle θ of 40°, one finds by applying Eqs. (2.2) and (2.1) associated scatter angles of respectively 78°, 57°, and 41° for Ar, Kr, and Xe. Therefore, for the 40° angle under which the Ru recoils are measured here, Xe ions producing those primary recoils will be scattered over almost the same angle. Assuming that the Xe ions do not penetrate below the surface, one might expect intensities from SC Xe and recoiled Ru to be of similar magnitude.

2.3.2 SPRAY results

In Fig. 2.5, a compilation of the simulated energy spectra of reflected (magenta) and recoiled (green) particles is shown for 15 keV Ar (left column), Kr (middle column), and Xe (right column) projectiles incident on Ru targets of different sample roughness: flat target (top row), treated target (middle row), and the untreated target (bottom row). For all projectiles, the angle of incidence angle is $\psi = 15°$ with respect to the surface plane, and the scattering angle θ is 40°. The sum of both reflected and recoiled particles is shown for each of the cases by the gray shaded spectrum. Similarly as for the experimental spectra, the expected energy ranges of the three different collisional events (see Fig. 2.2) are in each spectrum highlighted by the corresponding colored bands.

Fig. 2.5 indicates that the overall yield decreases when the target roughness goes up. The decrease in intensity is similar for all three projectiles. This common behavior could be expected as a surface inclination distribution (roughness) leads to a larger angular range of outgoing trajectories almost independent of projectile species. Light ions might be a bit more sensitive since, for the same impact parameter, light particles get scattered over a larger angle, and therefore, compared to heavier projectiles, a bit more likely to be scattered out off the angular detection bin of the simulations (and experiments). When examining the simulated spectra of the perfectly flat target, depicted in the top row of Fig. 2.5, it is evident that an SC peak is detected at the anticipated energy for each of the projectile types. However, the effect of roughness on the SC peak appears to be very different for each projectile. Where the SC peak is only a little bit suppressed for the Ar projectile (left column), it gets fully suppressed for Xe (right column). Besides a suppressed SC peak, a similar suppression of the REC peak is observed. This suppression is particularly visible for the heavier projectiles, where the ratio between the SC peak and the REC peak is the smallest.

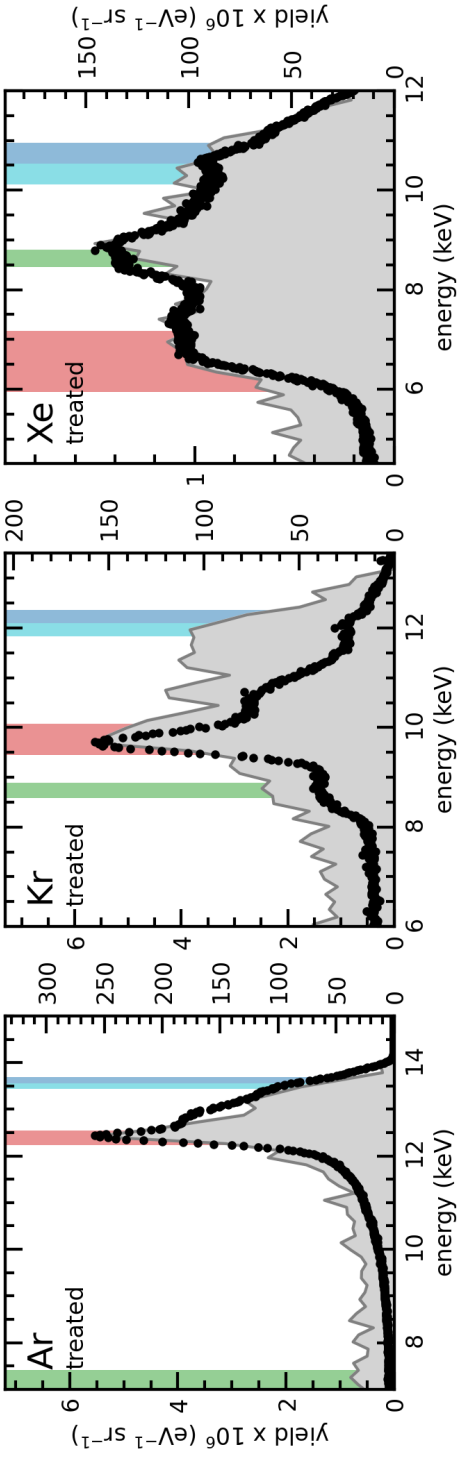

Figure 2.6: Spectral comparison of the experimental ion yield (black, left axis) and simulated particle yield (gray, right axis) for 15 keV (left) Ar, (middle) Kr, and (right) Xe projectiles colliding on a Ru surface. The expected energy range of the peak due to single collisions (red), double collisions (blue) and primary recoils (green) are indicated by the shaded areas. A darker shade of blue is included in the double collision band to indicate the expected energy range of the symmetric double collisions.

2.3.3 Comparison of experiment and simulation

For the treated Ru target, Fig. 2.6 compares normalized measured and simulated energy spectra. In comparing the measured and simulated spectra, one should realize that the measurements contain only charged particles, while in the simulations the charge state of the particles is not a parameter that is included. This difference might explain some of the (small) disagreements between the experiment and the simulation. From Fig. 2.6, one can see that for each projectile the low-energy tail is more pronounced in the simulated spectra than in the measured data. Typically, the tail is due to projectiles that scatter from deeper layers of the target and thus have a longer path length through the target which leads to enhanced straggling [18]. Generally, the lower the energy of the particle, the higher the probability that the scattered particles are neutralized [19].

For two of three projectiles (Ar and Xe) a good overall agreement between the experimental and simulation results is found. Interestingly enough, it is the Kr spectra where most disagreement is found. According to the SPRAY simulations, cf. Fig. 2.5, the shape of Ar spectrum is not very sensitive to the state of the surface roughness. On the contrary, the characteristic SC feature for Xe already disappears when going from the ideally flat to treated surface. For Kr, one notes that the SC peak is still present though less pronounced for the treated surface, and therefore might be most sensitive to the exact surface roughness. The area of the AFM image that served as input for the SPRAY simulations is smaller than the area from which scattered and recoiled ions are detected.

The high-energy side of the Kr spectrum, which contains the multiple scattering events, seems to be over-predicted by the simulations. However, one might equally well argue that the experimental spectrum is dominated by the SC events. The different ratio between SC and DC events in the simulations and the experiment could be due to a difference in the ion fractions for SC and DC trajectories, as assumed earlier for light ions [20]. This might be substantiated by the high ion fraction for Kr of $\approx 4\,\%$ obtained from the ratio between the ion and particle yield. Future time-of-flight measurements, in which both ions and neutrals are measured, could help clarify a potential effect of different ionization fractions. According to the SPRAY simulations shown in Fig. 2.5, roughness appears an unlikely explanation for the measured low fraction of multiple collision events, as the intensity of the multiple scattering events is almost independent on the roughness.

2.4 Conclusion

We have conducted a concerted set of experiments and simulations to investigate keV heavy-ion scattering off a polycrystalline Ru surface. A possible explanation of surface roughness as the cause for the absence of a prominent SC peak for the heaviest ions was tested. Experimental ion energy spectra of reflected and recoiled ions were taken for 15 keV Ar^{2+}, Kr^{2+}, and Xe^{2+} projectile beams incident on the Ru target at a scattering geometry of $(\psi, \theta) = (15^\circ, 40^\circ)$. A clear SC peak was observed for Ar and Kr, while for Xe, a prominent SC peak remained to be absent. The shape of the combined energy spectrum of reflected Xe and recoiled Ru ions is very well reproduced by our SPRAY simulations. Input to the SPRAY calculations is the actual roughness of the surface, which is extracted from AFM images. The roughness is described by triangulating small surface patches which then obtain a slightly inclined angle (a few degrees at maximum) from the global target surface. It is found that roughness indeed strongly impacts the visibility of the SC peak. From comparison to simulations for an ideally flat sample surface, it is found that such a narrow distribution of inclination angles peaking around 2° suffices to wash out the SC peak for Xe ion scattering. The surface roughness in our case (cf. Fig. 2.1) is, however, too small to lead to geometrical blocking of certain trajectories. The observation of a clear SC peak for Ar and Kr, but not for Xe, is in support of the conclusion that roughness-induced geometrical blocking of trajectories is not the prime cause of the absence of a prominent peak for Xe ion scattering. Therefore, weak scattering events on nearest neighbors to the binary collision partner are decisive, because it are these nearest neighbor contributions that define the integral scattering on single surface area patches, which are used to construct the actual surface roughness.

Acknowledgments

This work was conducted as part of the research program of the Advanced Research Center for Nanolithography (ARCNL), a public-private partnership of the University of Amsterdam (UvA), Vrije Universiteit Amsterdam, University of Groningen (RuG), the Netherlands Organisation for Scientific Research (NWO) and the semiconductor equipment manufacturer ASML. The experiments were performed at the ZERNIKELEIF facility operated by the Zernike Institute for Advanced Materials at the University of Groningen. The SPRAY simulations were performed at the Institute of Applied Physics of the TU Wien.

References

[1] J. F. Ziegler, J. P. Biersack, and U. Littmark, "The stopping and range of ions in matter", in (Pergamon Press, New York, 1985).

[2] J. F. Ziegler, M. D. Ziegler, and J. P. Biersack, "SRIM – The stopping and range of ions in matter (2010)", Nucl. Instrum. and Methods Phys. Res. B **268**, 1818–1823 (2010).

[3] N. Novikov, Y. Teplova, Y. Fainberg, and V. Kulikauskas, "Reflection of nitrogen ions from copper surface: Experiment and calculations", Nucl. Instrum. and Methods Phys. Res. B **235**, 448–451 (2005).

[4] M. Jurado Vargas and A. Fernández Timón, "A comparison between the codes SRIM and AlfaMC in the Monte Carlo simulation of alpha-particle backscattering", J. Radioanal. Nucl. Chem. **305** (2015).

[5] V. Shulga, "Note on the artifacts in SRIM simulations of sputtering", Appl. Surf. Sci. **439** (2018).

[6] H. Brongersma, M. Draxler, M. de Ridder, and P. Bauer, "Surface composition analysis by low-energy ion scattering", Surf. Sci. Rep. **62**, 63–109 (2007).

[7] C. Stilhano Vilas Boas, A. Zameshin, J. Sturm, and F. Bijkerk, "The influence of oxygen on the neutralization of slow helium ions scattered from transition metals and aluminum surfaces", Surf. Sci. **700**, 121680 (2020).

[8] S. Průša, M. Linford, E. Vaníčková, P. Bábík, J. Pinder, T. Šikola, and H. Brongersma, "A practical guide to interpreting low energy ion scattering (LEIS) spectra", Appl. Surf. Sci. **657**, 158793 (2024).

[9] R. A. Wilhelm, M. J. Deuzeman, S. Rai, W. Husinsky, P. S. Szabo, H. Biber, R. Stadlmayr, C. Cupak, J. Hundsbichler, C. Lemell, W. Möller, A. Mutzke, G. Hobler, O. O. Versolato, F. Aumayr, and R. Hoekstra, "On the missing single collision peak in low energy heavy ion scattering", Nucl. Instrum. and Methods Phys. Res. B **544**, 165123 (2023).

[10] S. T. de Zwart, A. G. Drentje, A. L. Boers, and R. Morgenstern, "Electron emission induced by multiply charged Ar ions impinging on a tungsten surface", Surface Science **217**, 298–316 (1989).

[11] N. Stolterfoht, R. Hellhammer, D. Fink, B. Sulik, Z. Juhász, E. Bodewits, H. M. Dang, and R. Hoekstra, "Dynamic properties of ion guiding through nanocapillaries in an insulating polymer", Phys. Rev. A **79**, 022901 (2009).

[12] E. Bodewits, H. M. Dang, A. J. de Nijs, D. F. A. Winters, and R. Hoekstra, "Atomic electron energy spectra of slow He^{2+} ions impinging on metallic surfaces", Nucl. Instrum. and Methods Phys. Res. B **267**, 594–597 (2009).

[13] M. Krems, J. Zirbel, M. Thomason, and R. D. DuBois, "Channel electron multiplier and channelplate efficiencies for detecting positive ions", Rev. Sci. Instrum. **76**, 093305 (2005).

[14] C. Cupak, P. S. Szabo, H. Biber, R. Stadlmayr, C. Grave, M. Fellinger, J. Brötzner, R. A. Wilhelm, W. Möller, A. Mutzke, M. V. Moro, and F. Aumayr, "Sputter yields of rough surfaces: importance of the mean surface inclination angle from nano- to microscopic rough regimes", Appl. Surf. Sci. **570**, 151204 (2021).

[15] W. Möller, "TRI3DYN - Collisional computer simulation of the dynamic evolution of 3-dimensional nanostructures under ion irradiation", Nucl. Instrum. and Methods Phys. Res. B **322**, 23–33 (2014).

[16] U. von Toussaint, A. Mutzke, and A. Manhard, "Sputtering of rough surfaces: a 3D simulation study", Phys. Scr., 014056 (2017).

[17] A. Mutzke, R. Schneider, W. Eckstein, and R. Dohmen, "SPTrimSP Version 5.00", IPP-report 12/8, 1–70 (2011).

[18] S. Lohmann, R. Holenák, P. Grande, and D. Primetzhofer, "Trajectory dependence of electronic energy-loss straggling at keV ion energies", Phys. Rev. B **107**, 085110 (2023).

[19] A. Boers, "Charge state of low energy reflected particles", Nucl. Instrum. and Methods Phys. Res. B **4**, 98–106 (1984).

[20] D. Primetzhofer, S. Rund, D. Roth, D. Goebl, and P. Bauer, "Electronic excitations of slow ions in a free electron gas metal: Evidence for charge exchange effects", Phys. Rev. Lett. **107**, 163201 (2011).

CHAPTER 3

Electron emission induced by slow Sn^{1-5+} ions on metal surfaces

Luc Assink, Victoria Vojtech, Richard Wilhelm, and Ronnie Hoekstra

In preparation

Abstract

Ion-induced electron emission by slow Sn^{1-5+} ions impacting Sn, Cu, and stainless steel targets is investigated. Average yields were obtained from electron statistics measurements and adjusted for zero-electron counting losses via Poisson-based correction. Deviations from Poisson statistics at higher electron numbers reveal an additional emission component with an effective electron yield of $\gamma^* \approx 2.5$, which, although small in magnitude, significantly enhances collision events generating a large number of electrons. For Sn^{1+} and Sn^{2+}, the electron yield scales linearly with ion velocity, indicating that electron emission is dominated by kinetic emission (KE). The extracted KE thresholds ($\sim 3 \times 10^4$ m/s) are nearly an order of magnitude lower than theoretical predictions and are similar for all targets. In contrast, the absolute values of electron yields show a clear material dependence, with Cu yielding the highest values, almost a factor of 2 higher than Sn and stainless steel. For Sn^{3-5+}, an additional velocity-independent contribution is observed and attributed to potential emission (PE). By separating KE and PE contributions, a clear increase of PE with charge state is found for Sn and stainless steel, while Cu exhibits significantly reduced PE yields. These results demonstrate that electron emission by Sn ions, in this regime of 0.5–20 keV, is governed by an intrinsic interplay of KE and PE, depending on charge state and target material.

3.1 Introduction

Particle-induced electron emission is a fundamental surface interaction process in which low-energy electrons are released following the impact of energetic particles. It plays a critical role in a wide range of applications, including vacuum electronics [1], space instrumentation [2, 3], low-temperature plasma devices [4], plasma-surface interactions [5–9], and ion-beam and plasma diagnostics [10, 11].

For the characterization of plasmas, including the laser-produced Sn plasmas in extreme ultraviolet lithography sources, charged-particle detectors such as Faraday cups, retarding field analyzers, and Langmuir probes are commonly employed. All these devices rely on an accurate measurement of particle-induced currents, which most often - if not always - are affected by secondary electron emission from detector surfaces themselves or from surrounding particle-facing material. An incomplete understanding of electron emission processes can introduce systematic errors in measured ion fluxes, or energy and charge-state distributions. Particle-induced electron emission depends sensitively on the projectile's charge state and velocity, and the electronic properties of the target material.

Detector components are frequently fabricated from stainless steel or copper because of their mechanical robustness, electrical conductivity, and compatibility with ultra-high vacuum environments. However, in EUV source conditions, prolonged operation might result in the deposition of tin on exposed detector surfaces. As a consequence, the effective surface encountered by the incoming ions may evolve over time from the original pure substrate material to tin-coated stainless steel or copper. If electron-emission yields differ appreciably between these materials, such an evolution of surface composition can significantly change detector response and thus its long-term measurement stability.

In this work, we systematically investigate secondary electron emission yields of slow Sn^{1-5+} ions impacting Sn, stainless steel, and Cu surfaces. By comparing these materials under identical experimental conditions, we aim to clarify the role surface composition plays in secondary electron emission and to provide data relevant for ion diagnostics in EUV lithography environments. The basic theory aspects of ion-induced electron emission are described first in the following. Then, the research approach is presented, which includes a description of the experimental setup and an extensive explanation of the data analysis methodology. Thereafter, the main results are discussed.

3.2 Mechanisms of ion-induced electron emission

Electron emission from solid surfaces under the bombardment by energetic particles has been studied extensively for almost a century. Nevertheless, electron emission driven by low-energy heavy species still lacks an adequate description. Two main mechanisms responsible for the emission of electrons are generally distinguished: potential emission (PE) and kinetic emission (KE). Potential emission typically occurs in the vicinity of the surface, prior to impact, and is governed by electronic transitions Kinetic emission, on the other hand, mainly originates inside the material due to collisional energy transfer.

As an ion approaches the surface, the potential barrier between the ion and the surface decreases, enabling several charge exchange and excitation processes. Fig. 3.1 schematically illustrates the four main electronic processes that can occur when an ion approaches a solid surface. In resonant charge exchange processes (I), electron transfer takes place from the solid to the ion (capture) or from excited levels of the ion/neutral to the solid (ionization). When an ion level aligns energetically with occupied states in the solid, an electron can transit from the solid to the ion (resonant neutralization), or, conversely, from the ion into empty states of the solid (resonant ionization), without requiring additional energy exchange. These processes are sensitive to the ion-surface distance, as the relative alignment of the electronic levels evolves due to image charge effects and screening. In Auger-type processes, energy is exchanged between two electrons. During Auger neutralization (II), an electron from the solid fills a low-lying empty level of the ion while a second electron of the sample is excited into the continuum. Auger deexcitation (III) is similar to Auger neutralization, but in this case, it is not an electron from the target that is emitted, but one from the projectile. This requires inner-shell holes in the projectile. Finally, collective excitations (IV), such as plasmons, can be triggered by capturing a surface electron in a tighter bound level in the incoming projectile.

Typically, for multiply charged ions, potential electron emission proceeds via resonant neutralization followed by Auger deexcitation, while for singly and doubly charged ions, Auger neutralization is the more likely source of electron emission [12, 13]. As a general rule of thumb, the smallest amount of potential energy E_{pot} required to allow for either of the two emission processes is determined by the work function W, and is given by:

$$E_{\text{pot}} > 2W, \tag{3.1}$$

where E_{pot} is the potential energy of the ion, and W the work function of the surface. For single charged ions, an estimate of the PE electron yield, based on

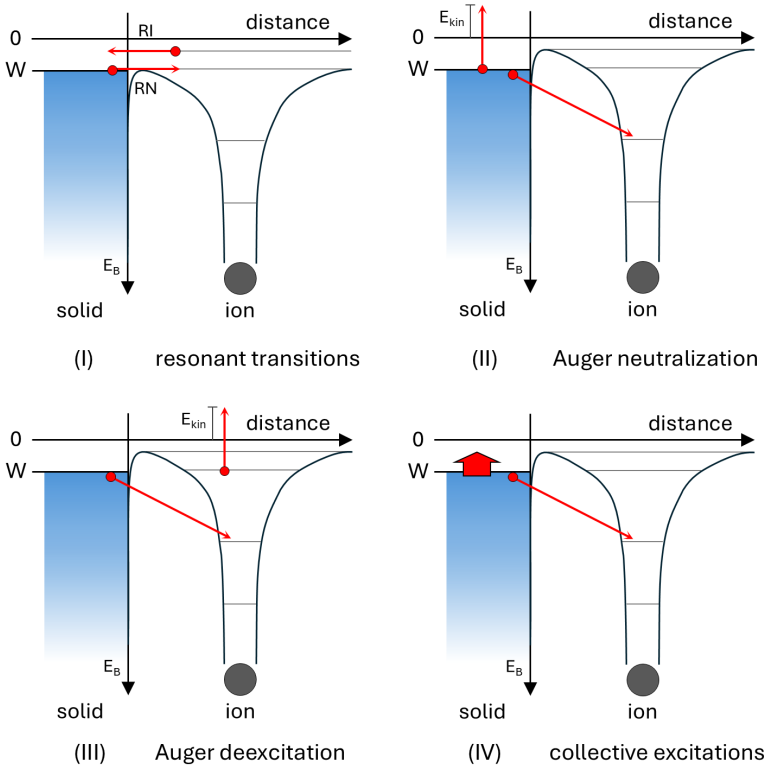

Figure 3.1: Schematic representation of electronic processes occurring during ion-surface interaction. (I) Resonant neutralization (RN) and resonant ionization (RI) occur via energy-aligned electron tunneling. (II) Auger neutralization involves a two-electron process in which one electron fills the ion while another is emitted. (III) Auger deexcitation describes the relaxation of an excited neutralized ion accompanied by electron emission. (IV) Collective excitations represent energy transfer to many-electron modes of the solid. The work function W and emitted electron kinetic energy E_{kin} are indicated.

the Auger neutralization model, was calculated by Kishinevsky et al. [14] as

$$\gamma_{\text{PE}} = 0.2(0.8E_{\text{IP}} - 2W)/E_F, \tag{3.2}$$

in which E_{IP} is the ionization potential of the neutral particle, and E_F is the Fermi energy of the target electrons. Baragiola et al. [15] used experimental data available in literature, and proposed an empirical formula of the form

$$\gamma_{\text{PE}} = 0.032(0.78E_{\text{IP}} - 2W). \tag{3.3}$$

In both cases, the electron yield scales linearly with the excess potential energy above an effective threshold. Since the interaction (and decay) time is limited

	E_F (eV)	v_F (m/s)	W (eV)	v_{th} (m/s)
Sn	10.5	1.91×10^6	4.42	1.8×10^5
Cu	7.0	1.56×10^6	4.70	2.3×10^5
SS 304	7.6	1.61×10^6	4.60	2.2×10^5

Table 3.1: Material-dependent parameters used to estimate the threshold velocity for kinetic emission, including the Fermi energy E_F [16], Fermi velocity v_F, work function W [17, 18], and resulting threshold velocity v_{th}, for Sn, Cu, and stainless steel (SS 304).

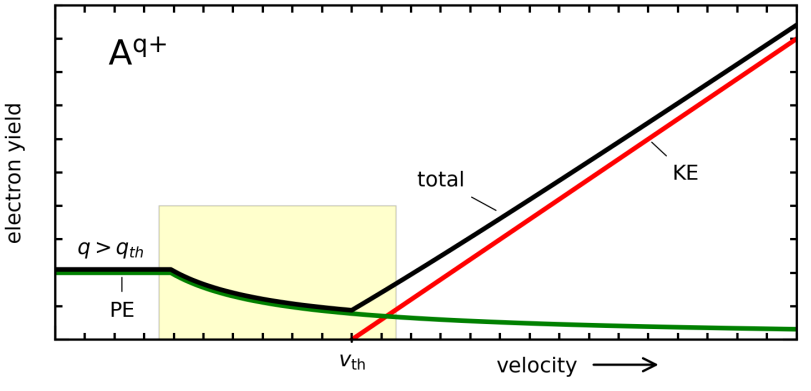

Figure 3.2: Schematic dependence of the electron yield on projectile velocity for an ion A^{q+}. At low velocities, electron emission is dominated by potential emission (PE), which decreases with inverse velocity. Above a threshold velocity v_{th}, kinetic emission (KE) emerges and increases approximately linearly with velocity, resulting in a transition regime from PE- to KE-dominated emission (shaded area).

	E_{IP} (eV)	E_{pot} (eV)	γ_{PE}		
			Sn	Cu	SS 304
Sn^{0+}	7.3	0	-	-	-
Sn^{1+}	14.6	7.3	-	-	-
Sn^{2+}	30.5	22.0	0.05–0.08	0.06–0.07	0.07
Sn^{3+}	40.7	52.5	0.30–0.48	0.43–0.46	0.40–0.47
Sn^{4+}	77.0	93.2	0.45–0.73	0.66–0.72	0.61–0.72
Sn^{5+}	94	170.3	1.00–1.64	1.49–1.62	1.38–1.63

Table 3.2: Ionization potentials (E_{IP}) [19] and the corresponding potential energies (E_{pot}) for different charge stats of Sn, together with calculated ranges of potential electron emission yields γ_{PE} (based on Eqs. 3.2 and 3.3) for the Sn, Cu, and stainless steel (SS 304) target materials. The reported ranges arise from variations in the work function and Fermi energy of the targets (see Table 3.1). The potential energy is given as the sum of the ionization energies required to reach the respective charge state.

to the short time interval in which the ion is in close vicinity to the surface, the efficiency of PE decreases with increasing projectile velocity [13]. Consequently, potential emission most significantly contributes at low impact velocities.

As the projectile penetrates the surface, it transfers kinetic energy to the electronic system of the target. Along its trajectory, the ion can interact with many target electrons, creating a large number of possible excitation events. If an electron gains sufficient energy to overcome the work function, it may escape from the surface. The maximum energy transfer from an ion to an electron occurs in a head-on collision, in which the momentum of the electron reverses [20]. Based on this, Baragiola et al. [20] proposed a threshold for kinetic emission. The transferred energy can be approximated by $\Delta E = 2mv(v + v_e)$, where v is the ion velocity, and m and v_e are the electron mass and velocity, respectively. This leads to a threshold velocity of the ion:

$$v_{th} = \frac{1}{2} v_F \left(\sqrt{1 + \frac{2W}{m v_F^2}} - 1 \right), \tag{3.4}$$

where v_F is the Fermi velocity. For the three target materials studied here, these parameters and the corresponding threshold velocities are shown in Table 3.1.

Typically, Eq. (3.4) yields threshold velocities on the order of 10^5 m/s for most metal surfaces. However, this approximation does not explicitly require the electron to reverse its direction after the collision, which is needed for the electron to be able to leave the surface. Accounting for this additional constraint would imply that the actual threshold velocity is higher. Nevertheless, good agreement between experiments and Eq. (3.4) is found for light projectiles [20]. For heavy ions, significantly lower thresholds have been observed [21, 22]. This discrepancy is generally attributed to additional mechanisms such as electron promotion [23].

The total electron emission resulting from the impact of an ion can be understood as the sum of contributions from both potential emission and kinetic emission. The relative importance of these two mechanisms depends strongly on the projectile velocity: while potential emission dominates at low velocities, kinetic emission becomes increasingly relevant as the velocity increases. Consequently, the total yield is a sum of potential and kinetic emission processes, see Fig. 3.2.

The slow, heavy Sn ions we consider here have velocities in the sub-threshold regime of Eq. (3.4), placing them in the regime where kinetic emission is expected to be absent. At the same time, Table 3.2 shows that for the lowest charge states considered, the available potential energy is relatively small, indicating that potential emission is likewise expected to be weak or absent. Consequently, the total electron yield in this regime is anticipated to be small, with only limited contributions from either mechanism (see the highlighted region in Fig. 3.2).

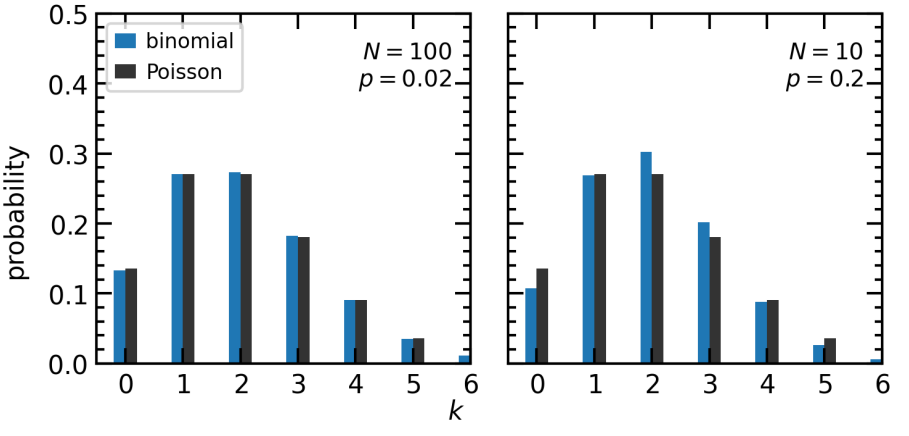

Figure 3.3: Comparison between binomial and Poisson distributions for an average yield of $\gamma = 2$. The left panel shows a binomial distribution with $N = 100$, and $p = 0.02$, which closely follows the Poisson distribution. The right panel shows a binomial with $N = 10$, and $p = 0.2$, where clear deviations from the Poisson appear. This illustrates that the Poisson approximation is valid when the number of possible excitation events N is large, and the probability p for each individual event is small.

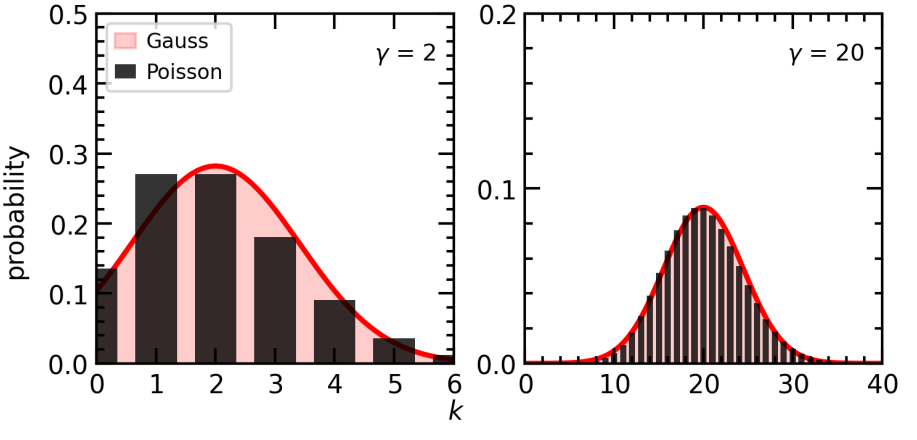

Figure 3.4: Comparison between Poisson and Gaussian distributions. The left panel shows the distributions for $\gamma = 2$, where noticeable differences remain. The right panel shows the distributions for $\gamma = 20$, where the Poisson closely approaches a Gaussian distribution. This illustrates the convergence of the Poisson distribution to a Gaussian for large values of γ.

3.3 Emission statistics

For electron emission processes, like KE emission, that are stochastic in nature, each interaction event has only a small probability of emitting an electron. However, a large number of such interactions may occur along the trajectory of the impinging ion. If these excitation events are statistically independent, the emission of electrons can be treated as a sequence of Bernoulli trials. If the number of possible events is denoted by N, and each event leads to electron emission with probability p, the probability of emitting n electrons follows a binomial distribution:

$$P(n) = \binom{N}{n} p^n (1-p)^{N-n}. \tag{3.5}$$

In most practical situations, the number of possible excitation events is large, while the emission probability for each individual event is small. In this limit, the binomial distribution approaches a Poisson distribution, which is given by:

$$P_n(\gamma) = \frac{\gamma^n}{n!} e^{-\gamma}, \tag{3.6}$$

where γ represents the average number of emitted electrons per ion impact. Fig. 3.3 shows a comparison between binomial and Poisson distributions for an average emission yield of $\gamma = 2$. The left panel shows a binomial distribution with $N = 100$ events, each with a probability of $p = 0.02$, which closely follows the Poisson distribution. The right panel shows a binomial with $N = 10$, and $p = 0.2$, which is not perfectly described by the corresponding Poisson distribution. This illustrates that the Poisson approximation is valid when the number of possible excitation events N is large, and the probability p for each individual event is small.

For large values of γ, the Poisson distribution converges to a Gaussian distribution given by

$$G(n, \sigma, \gamma) = \frac{1}{\sqrt{2\pi}\sigma} e^{-\frac{(n-\gamma)^2}{2\sigma^2}}, \tag{3.7}$$

in which the standard deviation is given by $\sqrt{\gamma}$. As illustrated in Fig. 3.4, noticeable differences remain between the two distributions for $\gamma = 2$ (left panel), while the Poisson closely approaches a Gaussian distribution in the case of $\gamma = 20$ (right panel).

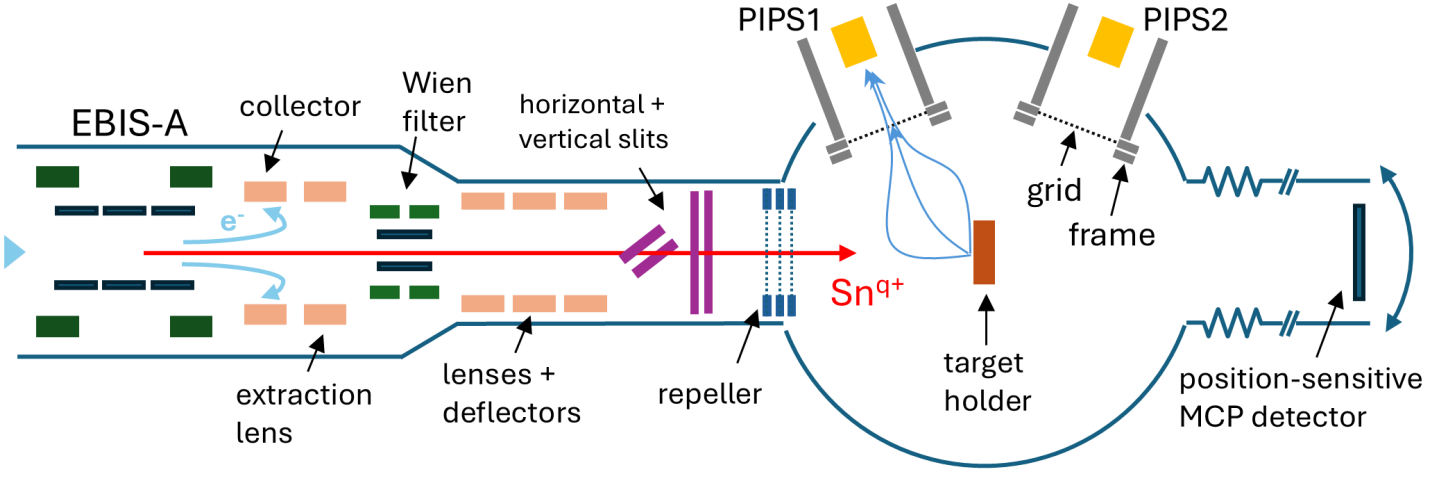

Figure 3.5: Schematic illustration of the *NIELS* setup at TU Wien. The Sn^{q+} ions are produced in the EBIS-A ion source. The desired isotope and charge state of the extracted ion beam is selected by the Wien filter and guided to the target chamber by means of electrostatic lenses, deflectors, and slits. The ion-induced emitted electrons can be collected by each one of the passivated implanted planar silicon (PIPS) detectors. To enhance the collection efficiency of the emitted electrons, a typical bias can be set to the electron repeller grid (−150 V), and to the collector grid (500 V) and its surrounding frame (−50 V) attached to the detector tubes surrounding each of the PIPS detectors.

In practice, large values of γ allow for rather accurate determination of the average yield since both the peak position and the width of the distribution relate to γ. This is different for small values of γ. The lower the yields, the larger the contribution of the "unmeasurable" $n = 0$ electrons case becomes. By fitting a partial Poissonian distribution P_n with $n > 0$, one can still obtain average electron yields, though with a somewhat lower accuracy.

3.4 Research approach

3.4.1 Experimental setup

The experiments presented in this chapter have been carried out using the *NIELS* (Neutrals and Ions Energy Loss Spectrometer) setup installed at TU Wien (Vienna, Austria) as part of the research facilities of the Atomic and Plasma Physics group led by Prof. Richard Wilhelm. A detailed description of the apparatus can be found in Ref. [24]; here, only the elements relevant to the present measurements are summarized. A schematic overview of the setup is shown in Fig. 3.5.

Ion beams are produced by an electron beam ion source (EBIS, from DREEBIT Dresden, Germany, type EBIS-A [25]). Sn ions are generated by introducing tetramethyltin ($C_4H_{12}Sn$) into the source via a leak valve. The voltage on which the source is operated is typically 4.4 kV, determining the kinetic energy of the extracted ions according to $E_{\text{kin}} = q \times 4.4\,\text{keV}$. The kinetic energy of the ion beam can be tuned to lower energies by applying an additional negative potential to the complete ion source.

After extraction, the ions are guided through a Wien filter to select the desired isotope and charge state. The beam subsequently passes through an electrostatic lens system, beam deflectors, horizontal and vertical slits, and an electron repeller (a high-transmission grid at negative voltage) before entering the target chamber. Downstream of the target chamber, a time-of-flight system equipped with a position-sensitive microchannel plate (MCP) detector is installed. In the present work, this detector is used exclusively for beam profile optimization.

The ultra-high-vacuum target chamber is held at a base pressure of 5×10^{-10} mbar and contains a movable sample holder capable of accommodating three different targets. In this study, three surface materials are investigated: stainless steel grade 1.4031 (X10CrNi18-8, commonly referred to as A2, comparable to AISI 304 stainless steel), polycrystalline Sn, and Cu. The first two are mounted in dedicated slots of the holder, while the sample holder itself, fabricated from an oxygen-free high thermal-conductivity copper-chromium-zirconium alloy (OFHC-CuCrZr), serves as the Cu sample. A schematic illustration of the sample holder is shown in Fig. 3.6.

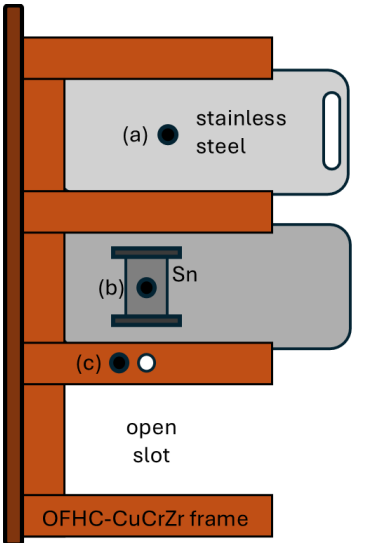

Figure 3.6: A schematic illustration of the sample holder, which can hold up to three different samples. The three different target positions presented in this work are indicated by the black dots: (a) stainless steel, (b) Sn, and (c) Cu. To ensure a constant beam profile for the different measurements, the ion beam is focused onto a position-sensitive microchannel plate detector (see Fig. 3.5) through the aperture in the sample holder.

For each projectile-energy setting, the ion beam is first focused through an aperture in the sample holder (diameter $\approx 3\,\text{mm}$) onto the MCP at the end of the beamline. This procedure ensures a reproducible beam position and profile for all measurements, independent of ion energy or target material. Prior to the measurements, all target surfaces were cleaned in situ by Ar^+ sputtering to remove possible surface contaminants.

The chamber is equipped with two partially implanted passivated silicon (PIPS) detectors used for electron-emission statistics measurements. This setup is based on earlier designs described in Refs. [26, 27]. Electrons emitted from the surface are accelerated towards the detector by an applied potential of approximately 25 kV. The detector is mounted inside a grounded tube containing a positively biased extraction grid surrounded by a negatively biased frame. For optimal collection efficiency, potentials of 500 V and −50 V are applied to the grid and frame, respectively, while −150 V is applied to the upstream repeller grid.

The detector generates an electric pulse whose amplitude is proportional to the total electron energy deposited by the incoming electrons. Since each emitted electron is accelerated through the full detector bias, and all n electrons produced by a single ion impact arrive within the integration time of the data

acquisition system (2 µs), the pulse height ideally scales with $n \times eV_{\text{det}}$, where n is the number of emitted electrons. The pulse-height spectra are recorded using a GBS MCA Cube527E multichannel analyzer (MCA). Based on the integration time of the MCA, the maximum count rate is approximately 500 kHz.

3.4.2 Spectral shape of the electron statistics spectra

When electrons are emitted following the impact of an ion on a surface, they are accelerated towards the PIPS detector by the detector potential V_{det}. Each electron therefore deposits an energy of approximately $-eV_{\text{det}}$ in the detector. As a consequence, peaks in the recorded spectrum appear at energies corresponding to integer multiples of this value.

In the present experiments, the detector voltage is $V_{\text{det}} = 25\,\text{kV}$. The full width half maximum (FWHM) of the individual peaks, denoted by ΔE_{det}, is experimentally determined to be approximately 12 keV. This width is primarily governed by the intrinsic energy resolution of the detector and by electronic noise in the detection system.

In practice, however, the observed spectral line shapes deviate from simple Gaussian peaks. This is mainly caused by electron backscattering within the detector. A fraction of the incident electrons undergo backscattering either at the detector surface or inside the bulk of the detector. In such cases, only part of the backscattered electron's energy is deposited. Consequently, the detected pulse height is reduced, and additional spectral structures appear between the main peaks.

If m out of n incoming electrons are backscattered, the corresponding spectral components appear at

$$E_{nm} = (n - mk)\, V_{\text{det}}, \tag{3.8}$$

where k represents the fraction of the energy deposited before backscattering. Typical values are around $k \approx 0.6$ [27], implying that approximately 40 % of the initial electron energy is deposited before the electron escapes.

The width of these backscattered peaks is larger than that of the primary peaks because of the additional spread introduced by the backscattering process. The resulting peak width can be written as

$$\Delta E_m = \sqrt{(\Delta E_{\text{det}})^2 + m(\Delta E)^2}, \tag{3.9}$$

where ΔE represents the FWHM of the energy distribution associated with the backscattered electrons (typically also about 12 keV [27]).

Fig. 3.7 illustrates the expected spectral shape of an ES spectrum for two limiting cases. In the absence of detector backscattering (left panel), the spectrum

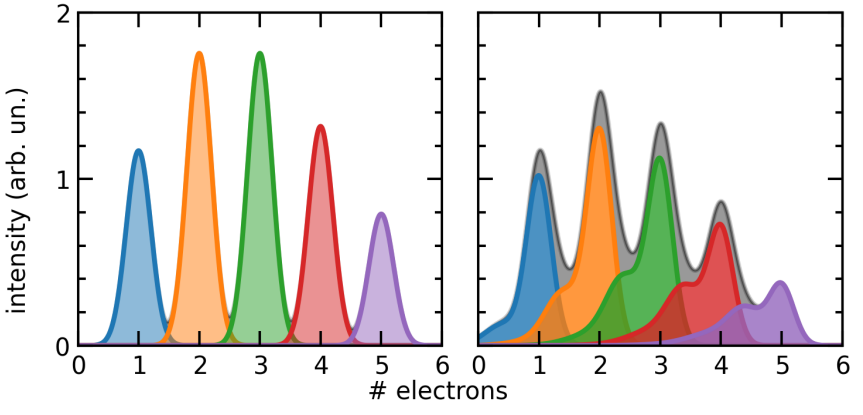

Figure 3.7: Illustration of the expected spectral shape of electron-emission statistics spectra recorded with a PIPS detector. Left panel: idealized spectrum in the absence of backscattering. Right panel: spectrum including electron backscattering within the detector. Partial energy deposition of backscattered electrons produces additional spectral components between the main peaks, resulting in the characteristic structured background observed in experimental ES spectra.

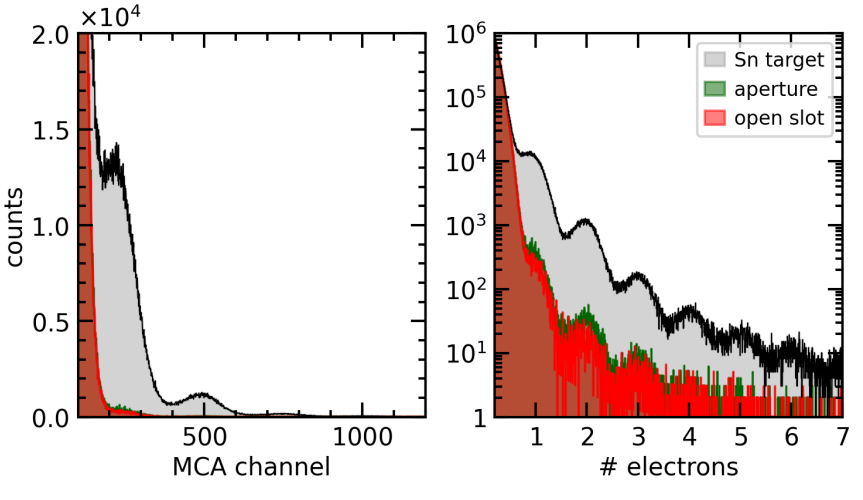

Figure 3.8: Comparison between experimental spectra of a 3.4 keV Sn^{1+} ion beam focused through the aperture (green), through the open target slot (red), and onto the Sn target (gray).

consists of well-separated Gaussian peaks located at integer multiples of V_{det}. When backscattering is included (right panel), additional structures appear between the main peaks, giving rise to the characteristic background observed in experimental ES spectra.

In the idealized case without backscattering, the measured spectrum can be described as

$$S(E) = \sum_{n=0}^{\infty} C_n F_n(E), \tag{3.10}$$

where C_n is a factor proportional to the probability for the emission of n electrons and $F_n(E)$ represents the detector response function, which can be approximated by a Gaussian distribution centered at E_n.

When backscattering is taken into account, the line-shape function becomes

$$F_n(E) = \sum_{m=0}^{n} P_{nm} G_{nm}(E, E_{nm}, \Delta E_{nm}), \tag{3.11}$$

where P_{nm} the probability that out of n electrons, m electrons are backscattered. This probability follows a binomial distribution (see Eq. (3.5)), with p the single-electron backscattering probability. The value of p depends weakly on the experimental geometry and detector configuration. Literature values typically lie between approximately 11 % and 13 % when partial re-attraction of backscattered electrons is taken into account, while an upper limit of about 17 % corresponds to pure backscattering without re-attraction [27]. The function G_{nm} represents a Gaussian distribution (see Eq. (3.7)) centered at E_{nm} with a standard deviation $\sigma_m = \Delta E_{nm}/2\sqrt{2ln2}$.

The complete spectral model is written as

$$S(E) = \sum_{n=1}^{n_{max}} \sum_{m=0}^{n} C_n \binom{n}{m} p^m (1-p)^{n-m} \frac{1}{\sqrt{2\pi}\sigma_m} e^{\frac{-(E-E_{nm})^2}{2\sigma_m^2}}, \tag{3.12}$$

and is fitted to the measured spectrum in order to extract C_n, which contains the information required to determine the average electron yield per ion.

3.4.3 Spectral background

The left panel of Fig. 3.8 shows a raw spectrum obtained for a 3.4 keV Sn^{1+} ion beam impinging on the Sn target. In this figure, the number of recorded counts is plotted as a function of the MCA channel number. Distinct peaks are observed around 250, 500, 750, etc., corresponding to the emission of one, two, three, and more electrons, respectively. From this spacing, we infer that approximately 250

MCA channels correspond to an electron energy of 25 keV, i.e., the conversion from channel number to electron number is 1/250.

A rapidly rising low-energy tail is visible at channel numbers below the first electron peak. Such a tail is typically caused by electronic noise picked up by the pre-amplifier. In order to correct for this low-energy contribution, and to account for possible additional background sources such as field-emission electrons, background spectra were taken by steering the ion beam through the aperture in the target holder or through the open target slot (see Fig. 3.6), thereby preventing ions from striking the target surface.

The right panel of Fig. 3.8 shows the same spectrum on a logarithmic scale together with two independently recorded background spectra. In this representation, the MCA channel number has been converted to the corresponding electron number, as will be done for all the following figures in this chapter. As can be seen, the two background spectra are in close agreement. Moreover, the low-energy tails of the signal and the background spectra overlap closely, indicating that this is truly a background signal. In contrast, the electron peaks themselves show almost no contribution from the background.

It is of note that, even for the 3.4 keV Sn^{1+} ion beam, emission events of no less than six electrons are observed, despite the fact that the projectile's kinetic energy is below the expected threshold and the potential energy of the ion is insufficient for potential emission (see Table 3.2). This will be further addressed in the Discussion section.

The low-energy tail caused by the electronic noise can be suppressed electronically by increasing the threshold settings of the MCA. However, we found that increasing the threshold also reduces the sensitivity of the lowest MCA channels. Conversely, if the threshold is set too low, the MCA gets drowned by the background signal. To optimize signal-to-noise, we investigated the dependence of the peak heights on the MCA threshold.

3.4.4 MCA threshold

The left panel of Fig. 3.9 shows the ratio of the peak height A_n for electron multiplicity n relative to the peak for $n+1$ (A_{n+1}) as a function of the MCA threshold value for a 4.4 keV/q Xe^{30+} beam incident on Cu. While only minor changes are observed with $n \geq 3$, a strong dependence on the threshold setting is observed for $n = 1$, and 2. Lowering the threshold further leads to washing out the peak structure. However, this effect affects all channels approximately equally. The data points were fitted with an exponential trend function, allowing us to estimate the peak height ratios in the limit of zero threshold.

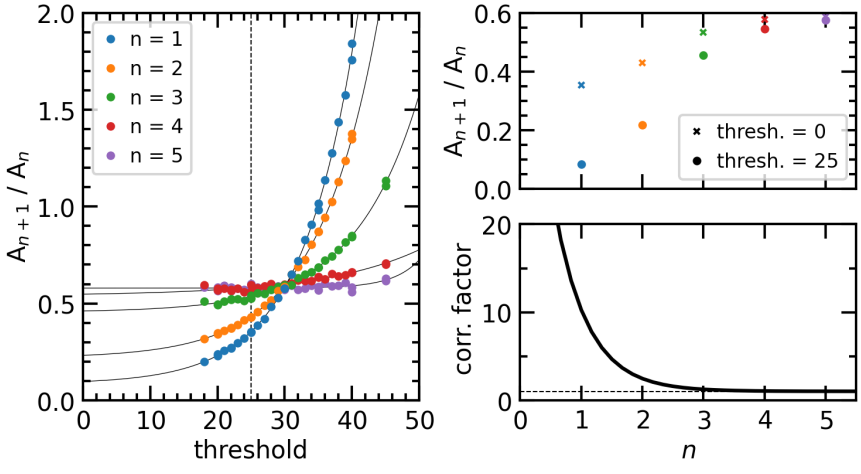

Figure 3.9: Correction of electron peak ratios for threshold effects in the MCA. The left panel shows the ratio of peak height (A_{n+1}/A_n as a function of the MCA threshold for a 4.4 keV/q Xe^{30+} beam incident on the copper target holder. The data are fitted with a trend function to extrapolate the intrinsic ratios in the limit of zero threshold. The upper right panel compares the measured ratios at the threshold setting of 25 with the extrapolated zero-threshold values. The lower right panel shows the resulting correction factor obtained from these ratios.

The upper right panel of Fig. 3.9 compares the measured peak height ratios at the threshold setting of 25 (used for the measurements in this chapter) with the extrapolated ratios at a threshold of zero. From these values, we determined the correction factor for the measured spectra. The resulting correction factors, shown in the lower right panel of Fig. 3.9, are obtained from the ratio between the extrapolated and measured peak ratios. For $n \geq 3$, the correction is negligible. However, for $n = 1$ and 2, a significant correction must be applied.

3.5 Average electron yield

The experimentally accessible quantities C_n (see Eq. (3.12)) represent the number of emission events of n electrons. Ideally, the true average electron yield is determined from

$$\gamma = \frac{\sum_{n=1}^{\infty} nC_n}{\sum_{n=0}^{\infty} C_n}. \tag{3.13}$$

However, the zero-emission events ($n = 0$) do not generate a detectable signal, and hence the so-called counting-loss C_0 cannot be measured directly. As already described in Section 2.3, this is not really a problem for high electron yields as

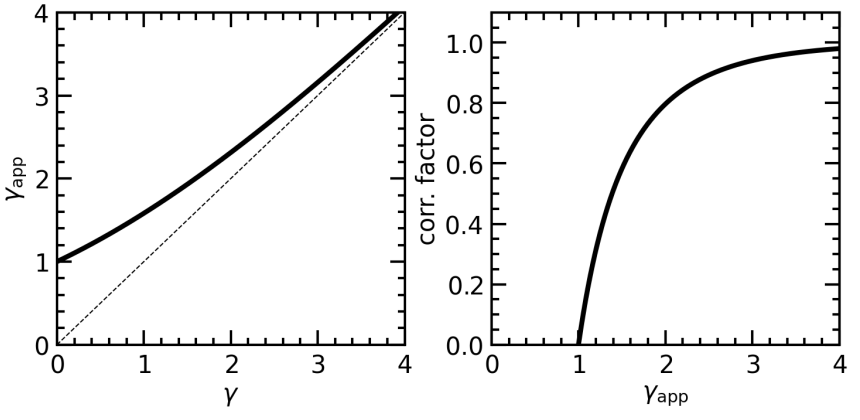

Figure 3.10: Relation between the apparent electron yield γ_{app} obtained from measured spectra and the true yield γ according to Eq. (3.16) (left panel). From this relation, a correction factor is approximated using a Taylor expansion of $e^{-\gamma}$. For small yields, the difference becomes significant because the fraction of undetected $n = 0$ events increases rapidly.

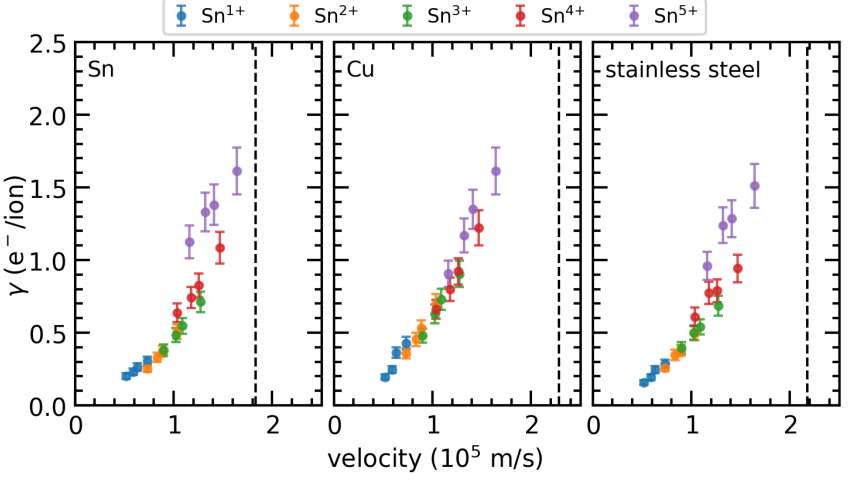

Figure 3.11: Average electron yield γ as a function of projectile velocity for Sn ions with charge states $q = 1 - 5+$ interacting with Sn, Cu, and stainless steel targets. Each panel corresponds to a different target material, as indicated. The dashed vertical line marks the characteristic threshold velocity v_{th} derived from the Fermi energy and work function of the respective material.

C_0 is negligible in these cases. But for systems with small yields ($\gamma \ll 1$), this can become problematic. In this regime, the contribution of unobserved $n = 0$ events increases rapidly. Without C_0, we can only extract the apparent average electron yield,

$$\gamma_{\text{app}} = \frac{\sum_{n=1}^{\infty} nC_n}{\sum_{n=1}^{\infty} C_n}. \tag{3.14}$$

This apparent yield basically represents the average yield of only those events that lead to electron emission.

Using Eq. (3.13) and Eq. (3.14), we find that

$$\frac{\gamma_{\text{app}}}{\gamma} = \frac{\sum_{n=0}^{\infty} C_n}{\sum_{n=1}^{\infty} C_n} = 1 + \frac{C_0}{\sum_{n=1}^{\infty} C_n}. \tag{3.15}$$

In the absence of a more accurate approach, C_0 is best estimated by assuming a Poisson distribution. By rewriting Eq. (3.15) and inserting the formula for the Poisson probability in the case of $n = 0$ (Eq. (3.6)), we find an approximate relation between the experimentally accessible apparent average yield and the true average yield:

$$\gamma_{\text{app}} = \frac{\gamma}{1 - e^{-\gamma}}. \tag{3.16}$$

This relation can be used to correct the apparent yields and estimate the true average emission yields (see Fig. 3.10).

Fig. 3.11 shows the corrected apparent electron yields as a function of projectile velocity for Sn^{1-5+} ions impacting three different target materials: Sn (left panel), Cu (middle panel), and stainless steel (right panel). In all three panels, the corresponding threshold for kinetic emission (see Table 3.1) is indicated by the black dashed line. The uncertainties in the measured γ_{app} are typically 5%, consistent with comparable experiments [27, 28]. An additional 5% uncertainty was included to account for the γ correction. Propagating these combined uncertainties through γ correction results in the error bars shown.

When comparing the different materials, the Cu target consistently exhibits the highest γ, while Sn and stainless steel are comparable over the investigated range. For all targets, a similar trend is found for Sn^{1-3+}: the electron yield increases with projectile velocity, and this increase appears to be approximately linear. For Sn^{4+} and Sn^{5+}, a similar linear dependence on velocity is observed. However, for the Sn and stainless steel targets, this yield seems to be enhanced with respect to the linear behavior describing Sn^{1-3+}. This enhanced yield is not observed for the Cu target, which follows the general trend more closely and thus appears an outlier compared to the other two materials.

3.6 Discussion

In Fig. 3.11, a non-zero electron yield is observed for all ion velocities, all charge states and target materials. Based on the respective thresholds for KE and PE, neither kinetic nor potential emission was to be expected for Sn^{1+}. Because the yields for Sn^{1-3+} follow the same linear trend, their difference in potential energy apparently plays no appreciable role. Therefore, it is safe to conclude that the observed electron emission is driven by KE, with a threshold of approximately 3×10^4 m/s for all materials, nearly an order of magnitude below the theoretical predictions around 2×10^5 m/s (see Table 3.1). Although in the sub-threshold regime, similar observations have been reported for singly-charged noble gas ions, for which potential emission is not excluded [15, 21, 22, 29, 30], only a few studies report non-zero yields in systems where both potential and kinetic emission are expected to be zero based on their emission thresholds [31–34]. There, the non-zero electron yield is attributed to KE-driven processes. One can thus derive the contribution of kinetic emission by Sn ions from the data taken with Sn^{1+} and Sn^{2+}. Knowing the KE yields, the additional PE yields may be determined.

3.6.1 Kinetic emission

Without PE contributions, the measured electron yield is solely due to γ_{KE}. To determine γ_{KE}, we consider Sn^{1+} and Sn^{2+}. Their yields in Fig. 3.11 are < 1, indicating that the emission is dominated by zero- and one-electron emission events. As explained in Section 3.5, the apparent average yield is corrected for the counting loss C_0, assuming Poissonian statistics. As observed in Fig. 3.8 for the example of 3.4 keV Sn^{1+} impacting on Sn, peaks corresponding to higher electron numbers n are clearly present, with yields for $n > 4$ up to one order of magnitude higher than expected from a Poisson distribution fitted to the $n = 1, 2$, and 3 electron peaks.

A straightforward workaround is the consideration of the intensity ratios of neighboring peaks. For a purely Poissonian distribution, the following relation holds:

$$\gamma = (n+1)\frac{C_{n+1}}{C_n}. \tag{3.17}$$

If this relation is satisfied over a range of consecutive n, the measured electron-emission statistics are consistent with a Poisson process.

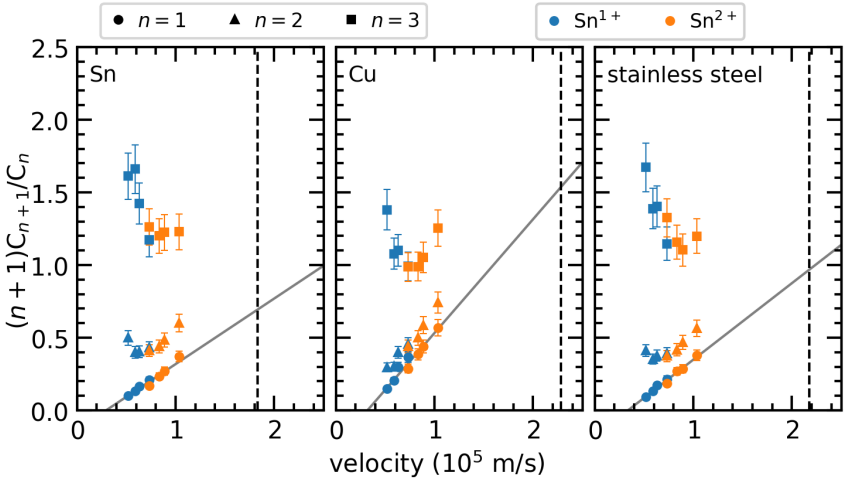

Figure 3.12: Consistency check of electron yields using adjacent peak ratios (Eq. (3.17)) for $n = 1, 2$, and 3 for Sn^{1+} (blue) and Sn^{2+} (orange) onto the three different target materials: Sn (left panel), Cu (middle panel), and stainless steel (right panel). The dashed lines indicate the threshold velocities v_{th}, while the lines represent linear trend lines fitted through the combined $n = 1$ data of the two charge states.

The results of such consistency checks are presented in Fig. 3.12 for Sn^{1+} and Sn^{2+} on the three target materials, for $n = 1, 2$, and 3. A clear systematic trend is observed: for both charge states, γ values derived from $n = 1$ are consistently lowest, those from $n = 2$ are slightly higher, and those from $n = 3$ are significantly higher. This increase with n indicates a growing deviation from Poissonian behavior. Notably, the $n = 1$ results for both Sn^{1+} and Sn^{2+} exhibit a linear dependence on ion velocity. The enhanced yields obtained from $n = 2$, and especially from $n = 3$, point to an additional emission contribution γ^* with $\gamma^*/\gamma_{KE} \gg 1$, which becomes more pronounced at higher n. Even a small fraction (of less than 10%) of such a γ^* contribution can dominate the high-n peaks. This effect is particularly evident for Sn^{1+}. At lower ion velocities, γ_{KE} approaches zero, causing the intensities of high-n peaks to become negligibly small. As a result, these peaks become highly sensitive to even minor contributions from "external" sources with $\gamma^*/\gamma_{KE} \gg 1$. Conversely, from the perspective of γ^*, the presence of small γ_{KE} contribution leads to a reduction in the effective γ^*.

As can be seen in Fig. 3.12, decreasing the Sn ion velocity (i.e., lower γ_{KE}) is associated with higher values of γ^*. This trend is observed for all three targets. The effect is more pronounced for Sn and stainless steel than for Cu, consistent with the larger γ_{KE} values for Cu. Extrapolating γ_{KE} to zero suggests, based on the $(n+1)C_{n+1}/C_n$ values for $n = 3$, that γ^* approaches a value between 2 and

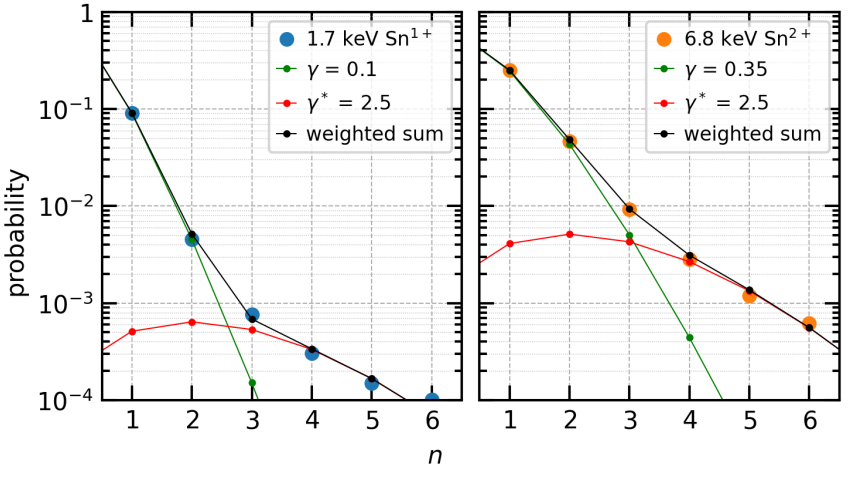

Figure 3.13: The weighted sum of two Poisson distributions (green γ_{KE}, and red γ^*) compared to experimental peak contributions (C_n) for 1.7 keV Sn^{1+} (left panel) and 6.8 keV Sn^{2+} (right panel) onto Sn. Note that the C_1 contribution has been scaled to the Poisson probability at $n = 1$.

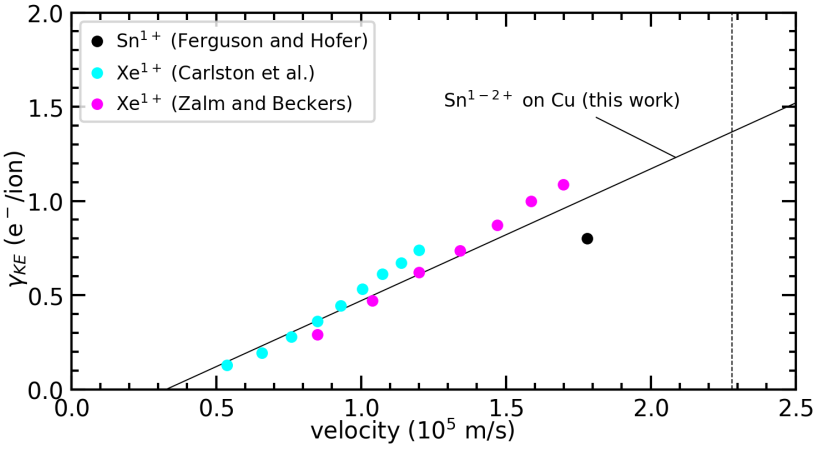

Figure 3.14: Comparison of linear KE trend (black line) on Cu with literature data of Sn^{1+} (single black dot, Ferguson and Hofer [35]) and Xe^{1+} projectile (cyan, Carlston et al. [29]; pink, Zalm and Beckers [21]) in the sub-threshold regime for kinetic emission.

3. This is further supported by Fig. 3.13, which shows that for the lowest and highest energy Sn ions where no PE contributions are expected (1.7 keV Sn^{1+} and 6.8 keV Sn^{2+}, respectively), the measured spectra are accurately reproduced by adding a $\gamma^* = 2.5$ contribution to the γ_{KE} spectrum. For both Sn^{1+} and Sn^{2+} at all energies, the presence of a $\gamma^* = 2.5$ component increases the $n = 2$ intensity by approximately 10 %. Accordingly, a 10 % correction has been applied to the $n = 2$ yield when determining the final KE electron yield γ_{KE}. For all three targets, the threshold velocities for KE-driven electron emission and their proportionality to velocity are summarized in Table 3.3.

	fitting parameters		threshold	
	slope (10^{-5} s/m)	intercept	v_{th} (10^5 m/s)	E_{kin} (keV)
Sn	0.41 ± 0.04	-0.12 ± 0.03	0.30 ± 0.04	0.54 ± 0.14
Cu	0.70 ± 0.06	-0.23 ± 0.04	0.32 ± 0.03	0.64 ± 0.12
SS 304	0.47 ± 0.04	-0.16 ± 0.03	0.34 ± 0.03	0.71 ± 0.12

Table 3.3: Linear fitting parameters ($\gamma = av + b$, with a the slope and b the intercept) and threshold values obtained from the linear fits to the $(n+1)C_{n+1}/C_n$ ratios for $n = 1$ (see Fig. 3.12). The fits are performed on the combined data points for Sn^{1+} and Sn^{2+} for all target materials.

The KE thresholds for electron emission are very similar for all three targets, indicating that the target material is not the most decisive ingredient in determining the KE threshold. In contrast, the slope of the γ_{KE} curve shows a clear material dependence. For Cu, the slope is the largest, exceeding those from stainless steel and Sn by approximately factors of 1.5 and 2, respectively. This suggests that while the threshold seems to be primarily determined by the projectile, the efficiency of electron production above this threshold is more sensitive to the target material.

For comparison, a single literature data point is available for 20 keV Sn^{1+} on Cu from Ferguson and Hofer [35], which is included in Fig. 3.14 alongside the γ_{KE} trend of the present experiment. In addition, the data for Xe^{1+} ions from Carlston et al. [29] and Zalm and Beckers [21] are shown. Xe^{1+}, being a heavy ion with a mass comparable to that of Sn^{1+}, provides a useful reference system. As can be seen in the figure, the Xe^{1+} data follow a similar linear trend with velocity and are in good agreement with the scaling observed for Sn. The literature point for Sn^{1+} lies close to the extrapolated trend of the present data, further supporting the validity of the obtained γ_{KE} dependence. Overall, the close agreement between Sn and Xe yields suggests that KE in this regime is largely governed by ion velocity and mass.

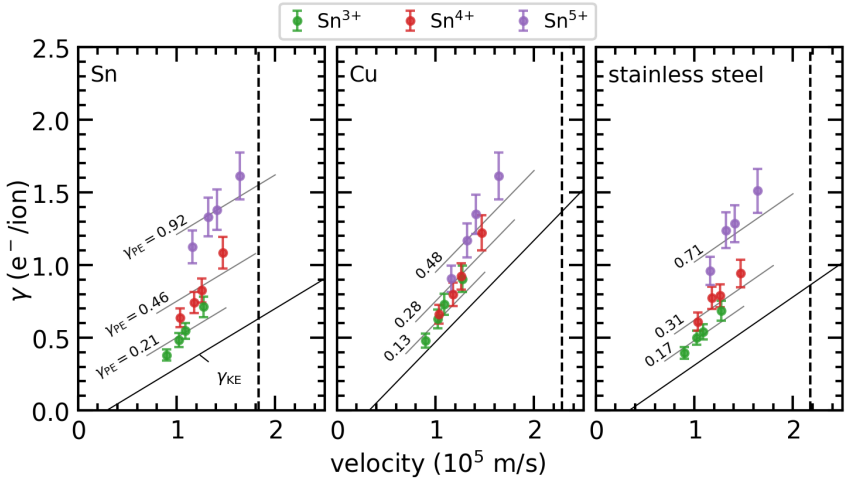

Figure 3.15: Comparison of the KE trend (black line) with the $(n+1)C_{n+1}/C_n$ ratios for $n = 1$ for Sn^{3+}, Sn^{4+}, and Sn^{5+} ions impacting Sn (left panel), Cu (middle panel), and stainless steel (right panel). For each material, trend lines with slopes fixed to the KE trend are fitted to the data, where the vertical offset reflects the PE contribution.

3.6.2 Potential emission

If the contribution of kinetic emission is roughly similar across the charge states, the PE contribution for the higher charge states can be extracted. Fig. 3.15 shows, for all three target materials, the extracted KE trend together with the $(n+1)C_{n+1}/C_n$ ratio for $n = 1$ measured for Sn^{3+}, Sn^{4+}, and Sn^{5+}. Instead of using the corrected apparent average yields, these ratios are considered, as they are least affected by an additional contribution of γ^* (on the order of ~ 2.5) discussed previously.

For each material, trend lines with slopes fixed to those of the corresponding KE curves are drawn through the Sn^{3-5+} data. Overall, these lines describe the data remarkably well, indicating that the velocity dependence of the emission remains governed by the same underlying KE scaling, while PE appears primarily as a constant offset on top of γ_{KE}. This supports the interpretation that the total emission can be described as a KE-driven contribution with an additional PE component that is largely independent of velocity. The vertical offset of the $q \geq 3+$ trend lines relative to the KE curve can therefore be used to extract γ_{PE} for the different charge states.

A clear material dependence is observed. For Sn and stainless steel, the data for Sn^{3+}, Sn^{4+}, and Sn^{5+} show a consistent upward shift relative to the KE trend, with an increasing offset for higher charge states, as expected for PE-driven

emission. In contrast, Cu appears as an outlier. For Sn^{3+} on Cu, the data lie very close to the KE curve, indicating little to no detectable PE contribution. In addition, the offsets for Sn^{4+} and Sn^{5+} are significantly smaller than those for the other materials, suggesting a reduced PE yield on Cu. It should be noted that the Cu target used here was not a well-defined single crystal but rather the sample holder itself, which may influence the PE probabilities and account for the reduced γ_{PE} relative to Sn and stainless steel.

3.7 Conclusion

In this chapter, the electron emission induced by slow Sn^{1-5+} ions impacting Sn, Cu, and stainless steel was investigated. By correcting for counting losses under the assumption of Poisson statistics and by analyzing adjacent peak ratios, the contributions of kinetic and potential emission were disentangled.

A key finding is the presence of non-zero electron yields far below the expected kinetic emission thresholds. The yields for Sn^{1+} and Sn^{2+} exhibit a clear linear dependence on ion velocity, demonstrating that the emission in this regime is dominated by KE processes. The experimentally determined KE threshold velocities, on the order of $\sim 3 \times 10^4$ m/s, are nearly an order of magnitude lower than theoretical predictions. This indicates that KE can occur under conditions previously considered sub-threshold.

Deviations from Poisson statistics were observed, particularly in the high-n tail of the electron spectra. These deviations are attributed to an additional emission component, γ^*, with an effective yield of approximately 2.5. Although its fractional contribution is small ($< 10\%$), it strongly affects the higher-order electron emission events. Removing this contribution allowed for a more reliable determination of KE yields.

For higher charge states (Sn^{3-5+}), an additional small velocity-independent contribution to the yield stemming from PE was identified. By fixing the slope of the velocity dependence to that of KE, the PE contribution could be extracted from the offset of the measured data. For Sn and stainless steel, a clear increase in PE yield with charge state was observed, though the yields remain still small ($\gamma_{PE} < 1$) for Sn^{4+} and Sn^{5+}. In contrast, Cu shows significantly lower γ_{PE} values, about half those for Sn and stainless steel. This difference may be due to the Cu target not being a well-defined single crystal but rather the sample folder itself, potentially affecting the emission characteristics. Further measurements on a well-defined Cu crystal would therefore be valuable for clarifying whether the reduced PE contribution is intrinsic to Cu or a consequence of using untreated OFHC target material.

Overall, the results demonstrate that electron emission in this low-velocity regime is governed by a combination of KE and PE processes, with KE determining the velocity dependence and PE contributing as an additive, largely velocity-independent component. The remarkably low KE thresholds and the role of additional emission channels highlight the need for a refined understanding of electron emission mechanisms at low ion velocities.

Acknowledgments

This work was conducted as part of the research program of the Advanced Research Center for Nanolithography (ARCNL), a public-private partnership of the University of Amsterdam (UvA), Vrije Universiteit Amsterdam, University of Groningen (RuG), the Netherlands Organization for Scientific Research (NWO), and the semiconductor equipment manufacturer ASML. The experiments were performed at the Institute of Applied Physics of the TU Wien.

References

[1] I. Figueiredo, N. Bundaleski, O. Teodoro, K. Jousten, and C. Illgen, "Influence of ion-induced secondary electron emission on the stability of ionisation vacuum gauges", Vacuum **2021**, 109907 (2021).

[2] A. Magnusson, A. Collins, and R. Wirz, "Polyatomic ion-induced electron emission (IIEE) in electrospray thrusters", Aerosp. Sci. J. **7**, 153 (2020).

[3] M. Klosterman, J. Rovey, and D. Levin, "Ion-induced charge emission from unpolished surfaces bombarded by an [Emim][BF4] electrospray plume", J. Appl. Phys. **131**, 243302 (2022).

[4] P. Riccardi, M. Ishimoto, P. Barone, and R. Baragiola, "Ion-induced electron emission from MgO by exciton decay into vacuum", Surf. Sci. **571**, 305–310 (2004).

[5] D. Depla, G. Buyle, J. Haemers, and R. De Gryse, "Discharge voltage measurements during magnetron sputtering", Surf. Coat. Technol. **200**, 14–15 (2006).

[6] N. Schupfer, D. Tshakaya sr, R. Khanal, S. Kuhn, F. Aumayr, S. Figueira de Silva, and H. Winter, "Effect of particle-induced electron emission (PIEE) on the plasma sheath voltage", Plasma Phys. Control. Fusion **48**, 1093 (2006).

[7] G. Kowarik, M. Brunmayr, and F. Aumayr, "Electron emission from tungsten induced by slow, fusion-relevant ions", Nucl. Instrum. Meth. B **267**, 16 (2009).

[8] A. Marcak, C. Corbella, T. De Los Arcos, and A. Von Keudell, "Note: Ion-induced secondary electron emission from oxidized metal surfaces measured in a particle beam reactor", Rev. Sci. Instrum. **86**, 106102 (2015).

[9] H. Hannesdottir and J. Gudmundsson, "The role of the metastable O2(b) and energy-dependent secondary electron emission yields in capacitively coupled oxygen discharges", Plasma Source Sci. Technol. **25**, 055002 (2016).

[10] C. Böhm and J. Perrin, "Retarding-field analyzer for measurements of ion energy distributions and secondary electron emission coefficients in low-pressure radio frequency discharges", Rev. Sci. Instrum. **64**, 31–44 (1993).

[11] E. Cantero, A. Sosa, W. Andreazza, E. Bravin, D. Lanaia, D. Voulot, and C. Welsch, "Design of a compact Faraday cup for low energy, low intensity ion beams", Nucl. Instrum. Meth. A **807**, 86–93 (2016).

[12] H. D. Hagstrum, "Theory of auger ejection of electrons from metals by ions", Phys. Rev. **96** (1954).

[13] H. Hagstrum, "Studies of adsorbate electronic structure using ion neutralization and photoemission spectroscopies", in *Electron and ion spectroscopy of solids*, edited by L. Fiermans, J. Vennik, and W. Dekeyser (Plenum Press, 1978), pp. 273–323.

[14] L. M. Kishinevsky, "Estimation of electron potential emission yield dependence on metal and ion parameters", Rad. Eff. **19**, 23–27 (1973).

[15] R. A. Baragiola, J. Alonso E. V. Ferron, and A. Oliva Florio, "Ion-induced electron emission from clean metals", Surf. Sci. **90**, 240–255 (1979).

[16] N. W. Ashcroft and N. D. Mermin, *Solid state physics* (Saunders, 1976).

[17] J. R. Rumble, ed., *Crc handbook of chemistry and physics* (CRC Press, 2024).

[18] H. B. Michaelson, "The work function of the elements and its periodicity", Journal of Applied Physics **48**, 4729–4733 (1977).

[19] A. Kramida, Y. Ralchenko, J. Reader, and NIST ASD Team, *NIST atomic spectra database (ver. 5.12)*, `https://physics.nist.gov/asd`, National Institute of Standards and Technology, Gaithersburg, MD., (2024).

[20] R. A. Baragiola, E. V. Alonso, and A. Oliva Florio, "Electron emission from clean metal surfaces induced by low-energy light ions", Phys. Rev. B **19** (1979).

[21] P. C. Zalm and L. J. Beckers, "Ion-induced secondary electron emission from copper and zinc", Surface Sci. **152-153**, 135–141 (1985).

[22] G. Lakits, F. Aumayr, M. Heim, and H. Winter, "Threshold of ion-induced kinetic electron emission from a clean metal surface", Phys. Rev. A. **42**, 9 (1990).

[23] R. A. Baragiola and P. Riccardi, "Electron emission from surfaces induced by slow ions and atoms", in *Radiative sputter deposition*, edited by D. Depla and S. Mahieu (Springer, 2008), pp. 43–60.

[24] J. Schwestka, D. Melinc, R. Heller, A. Niggas, L. Leonhartsberger, H. Winter, S. Facsko, F. Aumayr, and R. Wilhelm, "A versatile ion beam spectrometer for studies of ion interaction with 2D materials", Rev. Sci. Instrum. **89**, 085101 (2018).

[25] DREEBIT | Ion Beam Technology, *Dresden ebis-a*, (2023) `http://www.dreebit-ibt.com/product/dresden-ebis-a.html`).

[26] F. Aumayr, G. Lakits, and H. Winter, "On the measurement of statistics for particle-induced electron emission from a clean metal surface", Appl. Surf. Sci. **47**, 139–147 (1991).

[27] G. Lakits, F. Aumayr, and H. Winter, "Statistics on ion-induced electron emission from a clean metal surface", Rev. Sci. Instrum. **60**, 10 (1989).

[28] K. Töglhofer, F. Aumayr, and H. Winter, "Ion-induced electron emission from metal surfaces - insights from the emission statistics", Surf. Sci. **281**, 143–152 (1993).

[29] C. E. Carlston, G. D. Magnuson, P. Mahadevan, and D. E. Harrison, "Electron ejection from single crystals due to 1- to 10-kev noble-gas ion bombardment", Phys. Rev. **139**, A729–A736 (1965).

[30] H. Eder, F. Aumayr, and H. Winter, "Search for projectile charge dependence of kinetic electron emission from clean polycrystalline gold", Nucl. Instrum. Meth. B. **154**, 185–193 (1999).

[31] J. Lörinčík, Z. Šroubek, H. Eder, F. Aumayr, and H. Winter, "Kinetic electron emission from clean polycrystalline gold induced by impact of slow C^+, N^+, O^+, Ne^+, Xe^+, and Au^+ ions", Phys. Rev. B. **62**, 23 (2000).

[32] J. A. Yarmoff, H. T. Than, and Z. Sroubek, "Emission of electrons from clean and modified ru(0001) surfaces by low-energy na^+ bombardment", Phys. Rev. B **65**, 205412 (2002).

[33] M. Minniti, M. Commisso, A. Sindona, E. Sicilia, A. Bonanno, P. Barone, R. A. Baragiola, and P. Riccardi, "Kinetic electron emission from al surfaces by slow ions", Phys. Rev. B **75**, 045424 (2007).

[34] M. Pisarra, M. Commisso, A. Sindona, P. Riccardi, and Z. Sroubek, "Kinetic electron emission from metal surfaces by slow na^+ ions", Nucl. Instrum. and Methods Phys. Res. B **267**, 1721–1724 (2009).

[35] M. M. Ferguson and W. O. Hofer, "On the z_1 dependence of ion-induced kinetic electron emission", Radiat. Eff. Defects Solids **109**, 273–280 (1989).

CHAPTER 4

The voltage-dependent transmission function of a retarding field analyzer

Luc Assink, Emiel de Wit, Fleur Veen, Klaas Bijlsma,
Oscar Versolato, and Ronnie Hoekstra

Nucl. Instrum. and Methods Phys. Res. B. **579**, 166217 (2026)

Abstract

Retarding field analyzers (RFA) are widely used to measure ion energy distributions and fluxes from plasmas, but quantitative flux determination requires accurate knowledge of their grid stack transmission. The dependence of the transmission factor on the barrier voltage is investigated through a combination of experimental measurements and ion trajectory simulations. Experimental results for different ion species reveal a common transmission-voltage relationship independent of ion species, indicating that the effect is intrinsic to the analyzer. Ion trajectories through a four-grid RFA were modeled using SIMION to examine the influence of grid alignment and bias configuration. Without retarding potential, the transmission can be estimated by optical inspection. However, applied voltages introduce electrostatic lensing, which is most pronounced when grids are geometrically aligned. The electron suppressor grid introduces appreciable oscillations in transmission as a function of the voltage just below the ion cutoff voltage. The overall transmission arises from an intricate interplay of lensing, alignment, and grid spacing.

4.1 Introduction

The retarding field analyzer (RFA) is a compact and versatile instrument widely used to measure charged particle fluxes. Its ease of use and reliability have made it a standard tool for measuring ion energy distribution functions (IEDFs), particularly in the fields of plasma and ion beam physics [1–3]. One may think of (industrial) low-temperature plasma generators [4, 5], thermonuclear fusion reactors [6–8], ion beam sources and interactions [9, 10], spacecraft thrusters [11–14], and plasma sources for extreme ultraviolet (EUV) light for photolithography [15–17].

An RFA primarily consists of a Faraday cup (FC) to collect incoming ions (or electrons) and a stack of high-transmission grids (Fig. 4.1). The device owes its name to the retarding field that is created by applying a voltage to one of its electrodes. In this paper, we focus on ions, noting that the same principles apply to electrons with voltages of opposite polarity. The incoming ions are decelerated while passing through the field created by the retarding electrode. The potential on the retarding grid-electrode basically acts as a high-pass energy filter. It allows only ions with a kinetic energy E_{kin} greater than qV_{R} to overcome the potential barrier, where q is the charge state of the ion and V_{R} is the voltage set on the retarding electrode. Ions with insufficient energy are repelled. Differentiation of the measured current with respect to the retarding voltage yields the kinetic-energy distribution of the incoming ions.

The use of gridded electrodes aims to establish near-uniform potentials within the grid stack, thereby improving the energy resolution of the RFA. In practice, perfectly uniform potentials cannot be achieved due to field penetration within the electrodes, as discussed previously by Sakai [18]. However, the grids do intercept a significant fraction of the ions, reducing the measured current. Consequently, corrections are necessary to obtain quantitative ion fluxes from RFA measurements. Despite their wide use, a generic procedure for such corrections remains lacking and is recognized as a challenge in the absolute interpretation of RFA data [19–23].

A first-order correction for transmission losses is to scale the ion flux by the optical transmission value T, of the grid type used. Another widely used approach is the so-called "T^n" or "transmission multiplication rule", in which the optical transmission factors of all n individual grids are multiplied. The difference between these methods is substantial. As is evidenced by the comparison of the transmission values for an RFA with four identical grids of 81 % transmission in either perfect alignment (i.e. only displaced along the optical axis) or all shifted with respect to one another. Assuming a parallel beam with no angular divergence, the transmission of the grid stack is 81 % for perfect alignment of

the four grids, while in the fully misaligned case, a transmission of 43 % (0.81^4) is obtained. Throughout this work, this parallel beam transmission is referred to as the optical transmission. This represents a difference of nearly a factor of two, implying large uncertainties associated with the choice of the transmission correction method.

Both approaches rely on simplified assumptions about the ion trajectories. The optical method assumes straight-line trajectories, while the multiplication method assumes a homogeneous ion flux across all grids. In reality, ions follow neither perfect straight-line trajectories nor uniform spatial distributions. Instead, their trajectories are influenced by the electrode potentials and the geometry of the grid stack, giving rise to electrostatic lensing effects. Such lensing behavior caused by nonuniform fields within a gridded RFA has previously been discussed by Klenzing et al. [24]. Such lensing can focus or deflect ion trajectories, potentially directing a larger fraction of ions onto one of the consecutive grids and thereby altering the fraction of ions intercepted. The magnitude of these lensing effects depends on the voltages applied to the electrodes. Consequently, the transmission factor is voltage-dependent, as will be demonstrated by our experiments and simulations with monoenergetic ion beams. These experiments and simulations will underline the necessity of considering setting-dependent RFA transmission functions.

Recent work by Trottenberg et al. [23] demonstrated that the relative orientation of drilled grids can strongly affect the measured transmission characteristics of an RFA, leading to pronounced non-monotonic features associated with ion focusing and "channeling" phenomena through aligned apertures. Their study considered a grid geometry consisting of circular apertures arranged in a hexagonal pattern, while in the present work square apertures arranged on a square lattice are investigated. The alignment of successive grids was changed either by relative grid rotation (Trottenberg et al. [23]) or, in our case, through lateral translation of the grids. In addition, the grid dimensions (hole size and area, grid thickness, and geometrical transmission) are clearly different between the two. A comparative list of RFA specifications is presented in Table 4.1. These specifications result in different symmetry and transparency of the grid systems used. Together, the two sets of works cover complementary aspects of the role of grid geometry and alignment effects on RFA transmission. It is of note that the ratio between hole side/diameter and the distance between consecutive grids is close to 0.1 for both cases. This quantity is a representative measure for field inhomogeneities.

	this work	Trottenberg et al. [23]
holes	square	circular
hole side/diameter	229 µm	500 µm
grid thickness	25.4 µm	200 µm
single hole area	52.4 $\times 10^3$ µm^2	196 $\times 10^3$ µm^2
hole-hole dist.	254 µm	700 µm
transmission	81%	46%
symmetry	4-fold	6-fold
translation	yes	no
rotation	no	yes

Table 4.1: Comparison between the grid geometry used in the present work and that investigated by Trottenberg et al. [23], including differences in aperture shape, spacing, single-grid transmission, symmetry, and relative grid orientation.

In this work, the dependence of the transmission factor on the retarding voltage is investigated through a combination of experimental measurements and ion trajectory simulations. Experimental results reveal a transmission-voltage relationship that is the same for different ion beams, confirming that this behavior is an intrinsic characteristic of that RFA. To further explore this effect, ion trajectory simulations are performed for multiple grid configurations. The following section outlines the working principles of the RFA, emphasizing transmission and electrostatic lensing, after which the experimental setup and simulation approach are described.

4.2 RFA working principles

This work is based on a four-grid retarding field analyzer equipped with a Faraday cup (FC) for ion collection. We focus specifically on a four-grid configuration, as it corresponds to the RFA used in our experimental measurements. The schematic and working principles of the instrument are shown in Fig.4.1. Ions entering the RFA first pass through a grounded entrance grid (G) after which they encounter a set of two grids (R_1 and R_2) that together form the retarding electrode. The potential applied to these retarding grids defines the threshold energy for ions to reach the FC. Between the retarder and the collector, a suppressor grid (S) is placed that is biased negatively to serve two tasks: i) to repel incoming plasma electrons and ii) to prevent secondary electrons generated in the FC from escaping the FC.

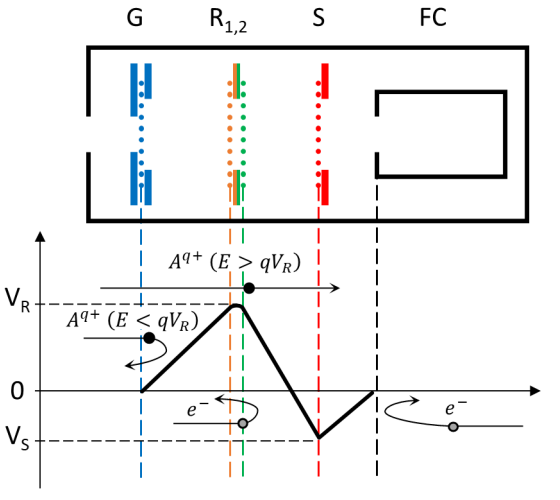

Figure 4.1: Schematic of a four-grid retarding field analyzer. The retarding voltage V_R defines a potential barrier transmitting only ions above a threshold energy. A negative suppressor voltage V_S prevents both plasma and secondary electrons from entering or escaping the Faraday cup.

The main function of the grids is to establish near-uniform electric fields between successive electrodes. This reduces unwanted effects on the ions' trajectories by field gradients stemming from specific, local electrode geometries, such as edges, holes, and connectors. Our grid stack is a commercial one by Kimball Physics (FC-73A), in which the retarding electrode has grids on either side of the retarding electrode plate. The use of a double-gridded retarding electrode aims to enhance the uniformity of the retarding barrier potential between the two grids with the goal of improving the energy resolution with respect to stacks with a single-grid retarding electrode. Nevertheless, ions flying through the center of a grid opening will experience a slightly different electric force compared to those passing close to the grid wires, e.g. Ref. [18].

Each grid effectively divides the beam into multiple smaller beamlets corresponding to ions passing through individual square apertures, cf. Figs. 4.2 and 4.4. These apertures act as weak electrostatic lenses that slightly deflect ion trajectories away from running parallel to the optical axis, introducing electrostatic lensing effects. Depending on the specific grid configuration and applied potentials, these lensing effects can focus or defocus the beam, thereby modifying which ions are intercepted by subsequent grids. As a result, RFAs with identical optical transmissions may still exhibit different effective ion transmissions due to differences in grid configuration. Here, the term grid configuration refers to the relative positioning of the individual grids within the stack, including lateral shifts,

relative rotations, and variations in the spacing between the successive grids. In this work, only lateral shifts are considered. Rotational shifts were previously investigated by Trottenberg et al. [23].

4.3 Research methods

4.3.1 Experimental setup

The ion beam experiments were performed in our crossed-beam setup [9, 25], which is one of the two permanent stations at the ZERNIKELEIF low-energy ion beam facility at the University of Groningen. The ion beams are generated by a 14-GHz electron cyclotron resonance ion source (ECRIS), which can be operated at voltages up to 30 kV. Due to the internal plasma potential, the actual ion energy is approximately 15 eV/q (with q the charge state of the ion) [26] higher than the energy expected from the voltage set to the source. Typical beam energy spreads are 5 eV/q [26]. ECR ion sources are the workhorses for producing high-intensity, highly charged ion beams [27]. We mainly use the source to produce Sn ion beams to support our research on Sn ion interactions with matter, in the context of understanding and improving 13.5-nm EUV sources for photolithography [25, 28]. After extraction from the ECRIS, the desired ion beam is selected using a 110° analyzing magnet with a mass-to-charge resolution of about 0.5 %. The selected ion beam then enters a 10-m central beamline from which it is bent into the crossed-beam setup by means of a 45° bending magnet. On its way from the bending magnet to the gas target, the ion beam is collimated by a set of six apertures, of which the smallest two have a diameter of 1.5 mm. This limits the divergence of the beam to less than 1°. The base pressure in the beamline and station is approximately 1×10^{-8} mbar. Therefore, no appreciable traces of electron capture by the ions are observed in the RFA signals. The ion current is measured with a Keithley 6485 picoammeter.

4.3.2 Optical inspection of a grid stack

The optical transmission of the RFA grid stack was determined using shadowgraphy images taken with a CMOS camera (XIMEA MQ013MG-E2). Due to the camera's limited depth of field, each grid was imaged separately, and an overlay was constructed to visualize the complete grid stack (Fig. 4.2).

Binary images of individual grids were obtained by applying independent thresholds to correct for variations in image brightness and then combined to obtain the stack's transmission pattern. From these binary images, both the grid spacing and wire thickness were derived. The separations between the

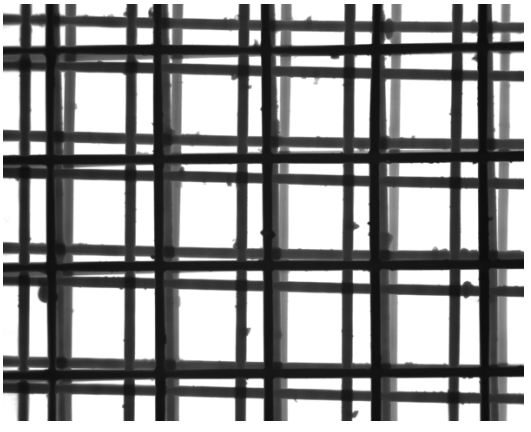

Figure 4.2: The grid configuration of the four-grid RFA. Each grid was photographed separately with a CMOS camera (XIMEA MQ013MG-E2) due to the limited depth of field, and the images were subsequently overlaid to reconstruct the full configuration.

successive electrodes are 2.54 mm (0.1") between the G-grid and the R_1-grid, 0.635 mm (0.025 ") between the two retarding grids (R_1 and R_2), and 1.905 mm (0.075 ") between the R_2-grid and the S-grid. Each grid has 100 pitches per inch (0.254 mm pitch), and a wire diameter of 25.4 µm (0.001 "), matching the single-grid transmission of 81 %. The overlay analysis gives an overall optical transmission of 47 %, slightly above the 43 % expected from multiplicative stacking due to partial overlap of the grid wires (Fig. 4.2). These geometrical parameters will be used in the simulation models.

4.3.3 Simulation approach

The simulations presented here are performed with the software package SIMION [29, 30]. For all nine different grid configurations, the ion trajectories of a 4 keV He^{1+} ion beam flying through an RFA have been simulated by replacing the full geometry of the RFA with the grid stack alone. Prior to those calculations, simulations of the full geometry of the RFA, including the surrounding shield and Faraday cup, were performed for four of these configurations. These calculations required specialized hardware with 128 GB of RAM and simulation times of several weeks per model. For this reason, we evaluated whether simulations restricted to the grid stack alone (10 x 10 mm) could accurately reproduce the behavior of the full geometry. As shown in the top panel of Fig. 4.3, excellent agreement between the two approaches is found.

As the simulation grid size unit in the model, we used 12.7 µm. This value was chosen such that grid wires are composed of two grid units, a minimum

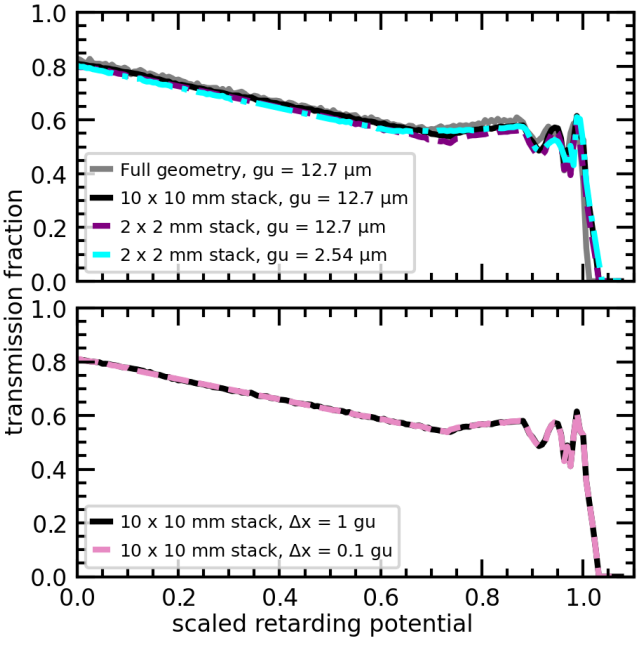

Figure 4.3: Comparison between different numerical settings used in SIMION. The upper panel compares different simulation approaches using the complete enclosed geometry, the full grid-stack (10 x 10 mm), and high-resolution simulations with a spatial discretization of 25.4 µm per grid unit on a reduced grid stack geometry (2 x 2 mm). The lower panel compares the default trajectory integration step (Δx) of 1 grid unit to a reduced trajectory integration step of 0.1 grid unit.

that is required by the software to define solid structures. The chosen resolution represents a compromise between numerical accuracy and computational feasibility, as increasing the spatial resolution rapidly leads to very large memory requirements and simulation times in SIMION. To assess the influence of discretization, additional simulations were performed for a higher spatial resolution of 2.54 µm per grid unit. The results of this discretization check are also included in the top panel of Fig. 4.3. No significant changes in the calculated transmission characteristics are found for the different approaches, indicating that using the grid-stack geometry solely is a valid approach.

As a further validity check, we tested the trajectory integration used by SIMION. We used its default setting, which corresponds to a nominal step length of 1 grid unit (12.7 µm) per integration step. For validation, we performed an additional simulation run (for model 1) with the nominal step length decreased to 0.1 grid units. As can be seen in the lower panel of Fig. 4.3, making the

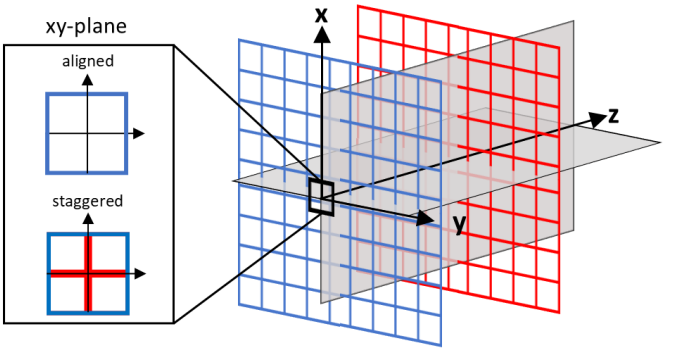

Figure 4.4: Schematic illustration of the aligned (top) and staggered (bottom) multi-grid configurations viewed from the front (xy-plane). In the aligned case, consecutive grids are perfectly positioned behind one another, while in the staggered case, the next grid(s) are laterally offset (by half a cell) so that a wire crossing coincides with the center of the first grid's opening.

trajectory integration step smaller by a factor of 10 yields no difference in the obtained results.

The exact grid configuration of the RFA (see Fig. 4.2) is rather complex due to a slight waviness of individual wires. In SIMION, due to the size of the computational mesh, we are limited to the use of straight grid wires. The dependence of the transmission on the alignment of the wires will be examined using several options for stacking the four grids.

The relative positioning of the individual wires is described using two classes of arrangements (see Fig. 4.4):

- **aligned**: this arrangement will introduce no physical ion obstruction on a consecutive grid for straight-line ion trajectories.
- **staggered**: physical ion obstruction on a consecutive grid (displaced by half a cell) will occur for straight ion trajectories.

Each pair of consecutive grids can be arranged in perfect alignment or staggered. For a four-grid system, this results in eight different RFA configurations. By means of the geometrical transmission of a single grid (81 %), the optical transmission for each configuration can be calculated. An overview of the eight different configurations is shown in Fig. 4.5, along with a ninth configuration resembling the actual RFA depicted in Fig. 4.2. In its second column, Fig. 4.5 presents the overall optical transmission and the relative positioning of each grid with respect to the entrance grid (G).

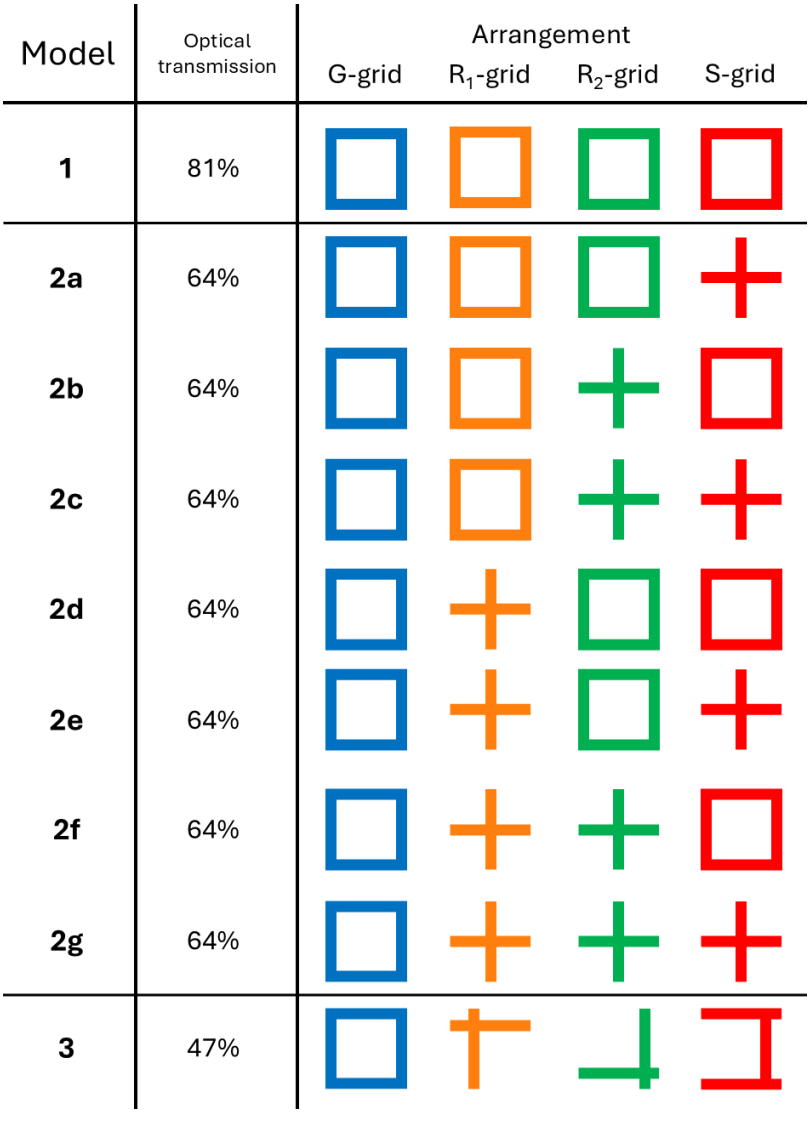

Figure 4.5: Compilation of the grid configurations used in nine simulation models, viewed from the xy-plane (normal to the grid surfaces). In model 1, all grids are aligned, giving an optical transmission of 81 %. In model 2, at least one of the grids is staggered relative to the entrance grids, reducing the optical transmission to 64 %. Model 3 resembles the grid arrangement of the actual RFA depicted in Fig. 4.2 with an optical transmission of 47 %.

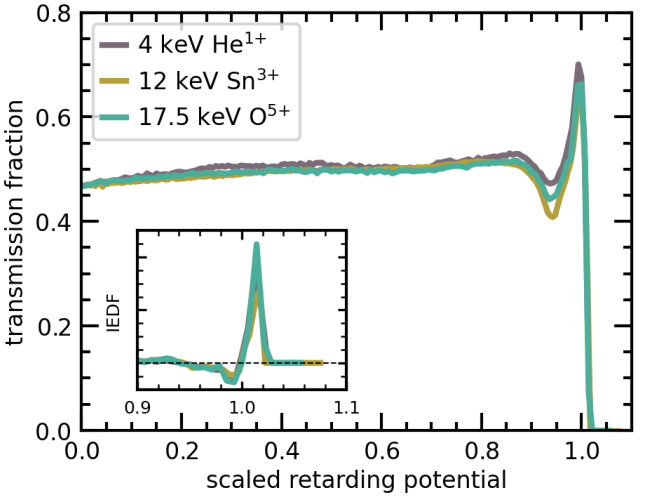

Figure 4.6: Experimental transmission curves for 4 keV He^{1+}, 12 keV Sn^{3+}, and 17.5 keV O^{5+} ion beams. All exhibit the same V–I response: a slight rise in transmission followed by a pronounced dip and peak near the retarding threshold, independent of ion species, charge, or energy. This demonstrates that the transmission function is an intrinsic feature of the RFA. The inset shows the negative derivative of the transmission curves, corresponding to the ion energy distribution functions.

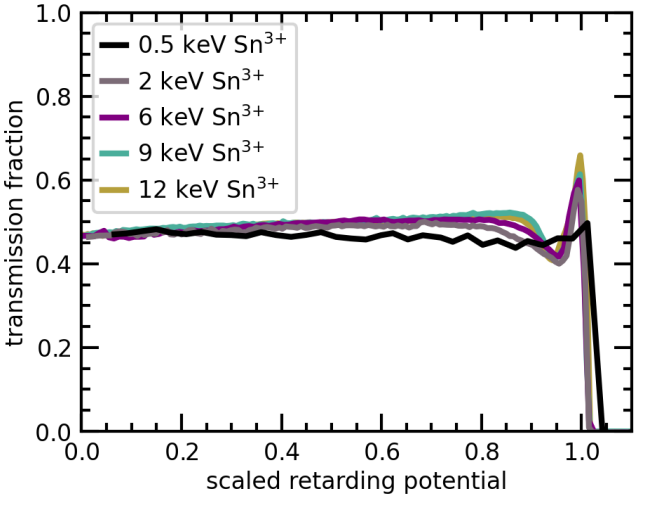

Figure 4.7: Experimental transmission curves for Sn^{3+} beams at various kinetic energies. While higher-energy beams follow the characteristic transmission shape, low-energy beams show deviations caused by the stronger relative influence of the suppressor potential.

It is of note that in the present study, the possible grid configurations are limited to idealized lateral shifts between the successive grids and do not include rotation or waviness of the grid wires. Consequently, the "random" configuration considered here (model 3) does not fully capture the actual grid arrangement as shown in Fig. 4.2.

4.4 Experimental results

The ion transmission as a function of the retarding voltage has been measured for several monoenergetic ion beams. For all experimental data sets the measured $I(V)$ curve was scaled at $V_R = 0\,V$ to the grid stack's optical transmission of 47 % (see Sect. 4.3.2). Because different retarding voltages are required to fully stop ion beams of different energy and charge state, the retarding potential is scaled by a factor of q/E_0, which allows for a direct comparison between different ion beams.

Fig. 4.6 shows the experimental transmission curves for ion beams of 4 keV He^{1+} (gray), 12 keV Sn^{3+} (ochre), and 17.5 keV O^{5+} (turquoise). The same $I(V)$ response is observed for all ion beams. As the retarding voltage is increased, the transmission fraction initially increases slightly. Below the blocking voltage of the ions, the signal exhibits a pronounced dip followed by a sharp peak. The increase in measured current is counterintuitive, since a higher potential should only reduce the transmitted ion current. The resulting dip and peak might therefore produce nonphysical features in the derived energy distribution. The inset of Fig. 4.6 shows the negative derivative of the transmission curves, corresponding to the IEDF. The consistency of $I(V)$ responses for the different ion beams indicates that the observed transmission function is a generic feature of the specific RFA used.

Fig. 4.7 shows the measured transmission curves for an Sn^{3+} ion beam of different energies. While the shape of the curve is retained for the highest energies, it slightly changes if the ion energy is lowered well below 1 keV. A likely explanation for this behavior lies in the fixed suppressor voltage of $-100\,V$ used throughout the measurements. The effect of the fixed suppressor voltage on the transmission function will be discussed in more detail in Sect. 4.5.2.

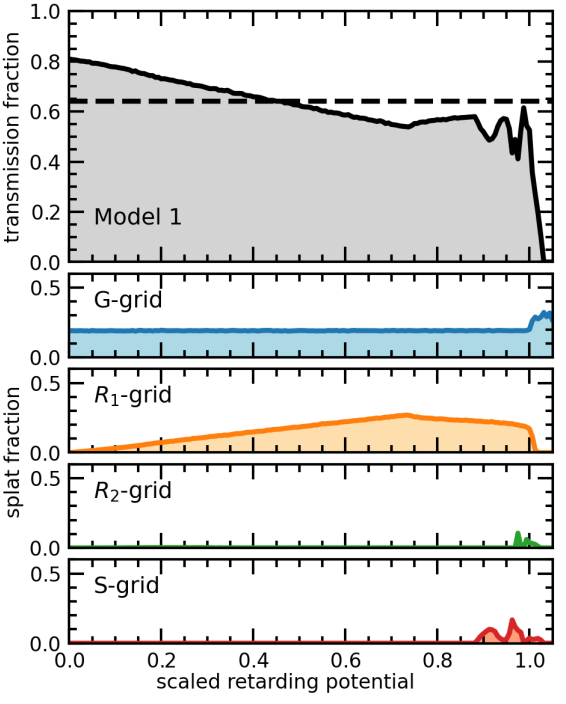

Figure 4.8: Simulation results of the transmission (top row) and splat fraction (lower rows) for a 4 keV He^{1+} beam through an RFA configuration with lined-up grids. The optical transmission of this model is 81 %.

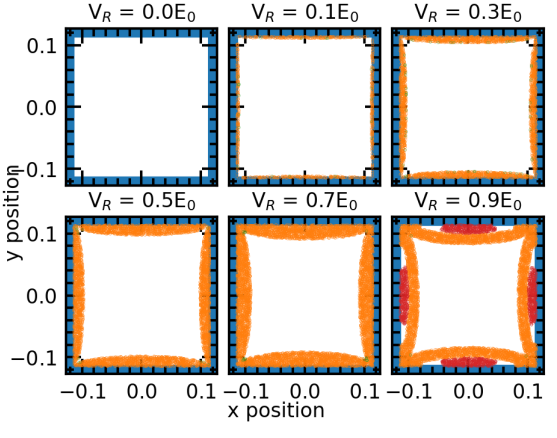

Figure 4.9: Compilation of the xy-position of the 4 keV He^{1+} ions (out of the 10^5 incoming ions) which splat on either the R_1-grid (orange), R_2-grid (green), or S-grid (red), as they pass the entrance grid for different retarding voltages, as obtained from simulations using model 1. Each point represents a single splatted ion, color-coded according to the grid on which they splat. The entrance grid itself is colored in blue.

4.5 Simulation results

The following results are obtained from ion trajectory simulations of 4 keV He^{1+} ions through the different grid-model configurations illustrated in Fig. 4.5. Although the experimental results (Fig. 4.6) showed that the transmission curve is insensitive to the choice of projectile (with keV energy), using 4 keV He^{1+} in the simulations maintains consistency with the experimental dataset. A fixed suppressor voltage of -100 V is used for all simulation models, unless stated otherwise.

4.5.1 Perfect grid alignment (Model 1, $T_{\mathbf{opt}} = 81\%$)

Model 1 has a grid configuration with all its grids perfectly lined up behind each other. The results of the trajectory simulations are presented in Fig. 4.8. The top panel of the figure depicts the fraction of ions that end up in the Faraday cup and represents the ion transmission through the RFA. In the lower panels, each panel corresponds to a specific grid and shows the fraction of ions intercepted by that grid, i.e. the splat fraction.

The ion transmission is strongly affected by the applied retarding voltage and clearly deviates from both the single-grid transmission of 81 % and the 43 % calculated by the transmission multiplication rule. Over the retarding voltage range of 0 to 4 kV, the average ion transmission is 64 %, as indicated by the black dashed line.

Ions flying into the detector perpendicular to the grids will only be obstructed by the first grid, the entrance grid. Therefore, when no bias is applied to any one of the grids, an ion transmission equal to the single-grid transmission of 81 % is expected. This value is reproduced by the simulations. At low barrier voltages, the transmission decreases smoothly to approximately 55 % at about three-quarters of the bias needed to fully block the ions. At high barrier voltages, the transmission starts to show irregular wiggles before it fully drops to zero; see the top panel of Fig. 4.8. The figure shows that the decreasing trend in transmission is caused by an increased splatting on the R_1-grid. The wiggles are by and large related to ions hitting the suppressor grid (S-grid), and to a lesser extent the second retarding grid (R_2-grid).

For a selection of retarding voltages, the xy-positions of obstructed ions as they pass through the entrance grid are shown in Fig. 4.9. Each point in these figures represents a single splatted ion, color-coded according to the grid on which it splatted (see Fig. 4.5). It is shown that the initial smooth decrease in transmission due to an increasing number of ions splatting on the first retarding

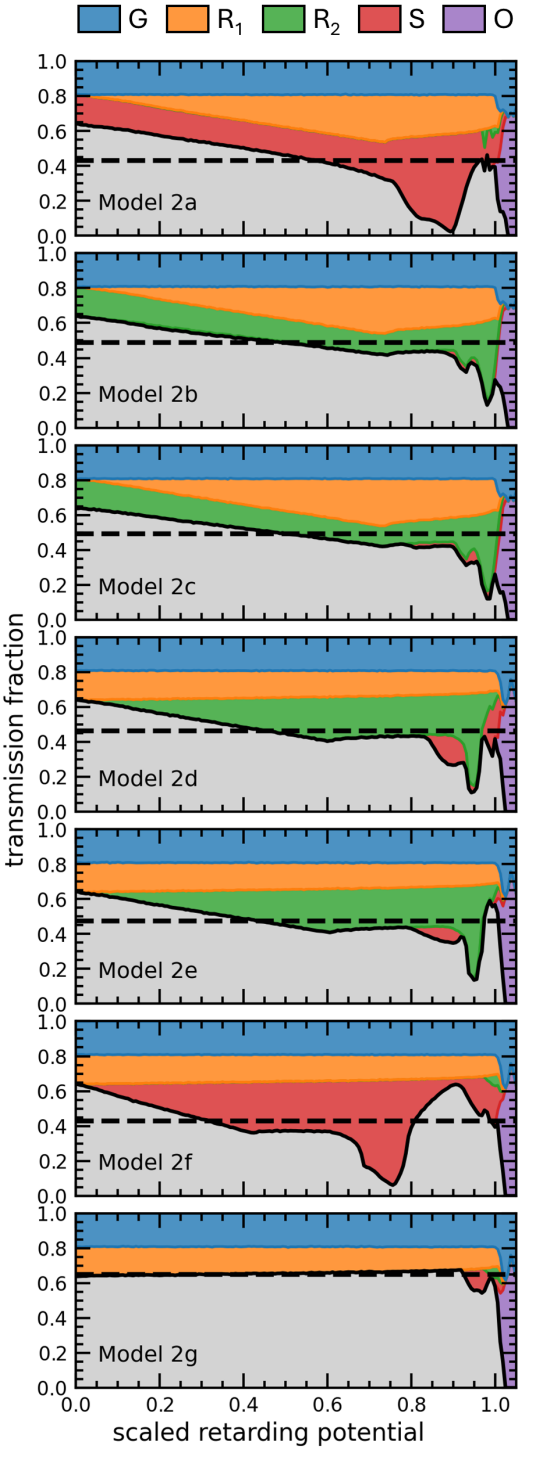

Figure 4.10: Compilation of simulation results for the transmission (gray shaded area) through all the different model configurations with the same optical transmission of 64 %. For each model, the fraction of the back-reflected ions that end up outside (O) the RFA is represented by the purple areas.

grid (R_1-grid), as shown in Fig. 4.8, stems from lensing effects at the entrance grid (G-grid).

4.5.2 Staggered grid alignments (Models 2, $T_{\mathbf{opt}} = 64\%$)

The simulation results for staggered configurations (models 2a–g, see Fig. 4.5) are shown in Fig. 4.10. For clarity, the ion transmission (gray area) is plotted together with the splat fractions of the individual grids (colored areas). Note that all seven configurations of model 2 have the same optical transmission of 64 %. To make sure that together all contributions add up to unity, the ions which at $qV_R/E_0 > 1$ get back-reflected and end up outside (O) of the RFA are represented by the purple area.

Except for configuration 2g, all transmission curves show a behavior similar to model 1: an initial decrease in ion transmission (from 64 %to about 40 %) followed by the occurrence of wiggles just below the drop-off voltage. Below, we discuss the recurring features in the transmission curves (Fig. 4.10) and relate them to the way the grids are consecutively stacked (see Fig. 4.5).

Low barrier voltages ($qV_R/E_0 < 0.6$)

The initial decrease in ion transmission is associated with an increased splatting on the R_1-grid (orange area) in configurations 2a–c, where R_1 is aligned with the entrance grid, as in model 1. In 2d and 2e, the R_1-grid is staggered, leading to a constant splatting fraction on R_1. The first grid aligned to the entrance grid is R_2, and accordingly the decrease in ion transmission originates from splatting on the R_2-grid. In 2f, only the suppressor (S) grid is aligned, while both retarding grids are staggered; here, the decrease in ion transmission results from increased splatting of the S-grid (red area). These findings indicate that the initial decrease in ion transmission arises whenever at least one consecutive grid is aligned with the entrance grid. The voltage at which this decreasing trend stops is determined by the distance between the entrance grid and the first aligned grid. Since the R_2-grid is positioned further downstream, and the suppressor even further, a smaller potential gradient is sufficient to produce comparable focusing and splatting effects at larger separations. In 2g, where all grids are staggered with respect to the entrance grid, no such decrease is observed.

The transmission behavior for low barrier voltages across configurations 2a–g is largely determined by which grids are aligned with the entrance grid and how subsequent grids are staggered. An initial transmission drop consistently appears whenever at least one grid is directly aligned, while configurations with all grids staggered (e.g., 2g) avoid this feature.

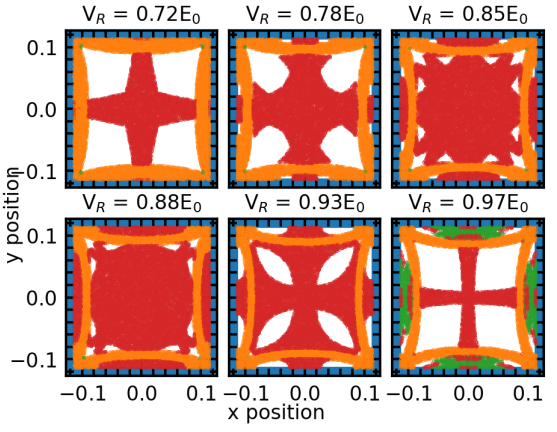

Figure 4.11: Compilation of the xy-position of the ions (out of the 10^5 incoming ions) which splat on either the R_1-grid (orange), R_2-grid (green), or S-grid (red), as they pass through the entrance grid for different retarding voltages, as obtained from simulations using model 2a. Each point represents a single splatted ion, color-coded according to the grid on which they splat. The entrance grid itself is colored in blue. For these simulations, a total of 10^5 incoming ions are used.

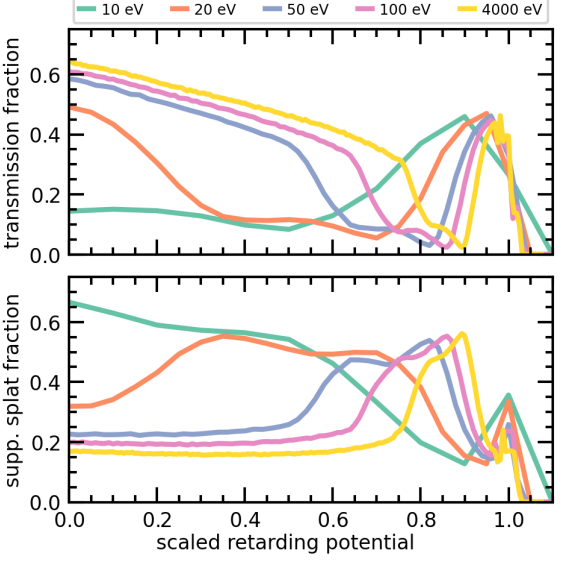

Figure 4.12: Simulation results of the transmission (top panel) and splat fraction on the suppressor grid (bottom panel) for ions with energies of 4000, 100, 50, 20, and 10 eV flying through RFA model 2a. For all simulations, the suppressor voltage is −100 V.

High barrier voltages ($qV_R/E_0 > 0.6$)

Ion splatting on the suppressor grid determines the wiggle structure in model 2a and model 2f. In these cases, the suppressor grid is staggered while the two retarding grids are aligned (see Fig. 4.5). For model 2a, the xy-positions of the splatted ions as they pass through the entrance grid are shown in Fig. 4.11 for a selection of high barrier voltages. At voltages between 80–90 % of the blocking voltage, nearly all ions not intercepted by the first retarding grid are focused onto the suppressor. This causes the ion transmission to drop to almost 0 in that voltage range.

Fig. 4.10 also shows that the oscillatory features in configurations 2b–e are primarily driven by splatting on the second retarding grid when it is staggered relative to the first. The oscillations are weakest in 2g, where both retarding grids and the suppressor grid are aligned. Overall, pronounced oscillations in ion transmission occur when either the second retarding grid or the suppressor grid is staggered with respect to the first retarding grid.

For high barrier voltages, the presence and strength of oscillations depend on the interplay between the retarding grids and the suppressor grid: oscillations are strongest when one of these is staggered relative to its predecessor, and weakest when they are all aligned. These general trends highlight how grid alignment governs both the baseline transmission level and the detailed shape of the transmission curves. Remarkably enough, the highest and most constant transmission is found for configuration 2g (see Fig. 4.10) in which neither grid R_1, R_2, nor S is aligned with the entrance grid.

The effect of the suppressor

So far, we have seen that the RFA transmission can be well represented by a single common function using a scaled argument of qV_R/E_0. However, this neglects possible effects of the suppressor voltage. The suppressor is held at a constant value in this case of -100 V, and this voltage becomes increasingly significant for lower-energy beams, as was already indicated in Sect. 4.4. Using model configuration 2a, Fig. 4.12 (top panel) presents simulated transmission results for ions with kinetic energies from 4000 eV down to 10 eV. In addition to the transmission function, the splat fraction on the suppressor grid is shown to highlight its contribution.

First of all, between $qV_R/E_0 = 0.6$ and 0.9, the link between decreased transmission and increased suppressor splatting is clearly visible. The precise width of the range depends on the energy of the ions: the lower the ion energy,

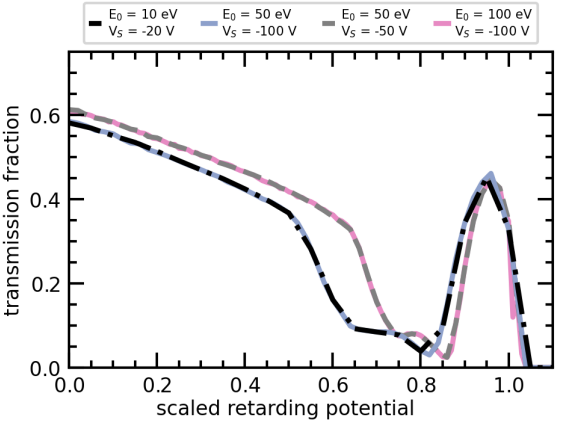

Figure 4.13: Comparison of simulation transmission curves for different combinations of ion beam energy (E_0) and suppressor voltage (V_S). The curves corresponding to $V_S = -100\,\mathrm{V}$ are identical to those shown in Fig. 4.12 and are included here for direct comparison of similar $|qE_0/V_S|$ values.

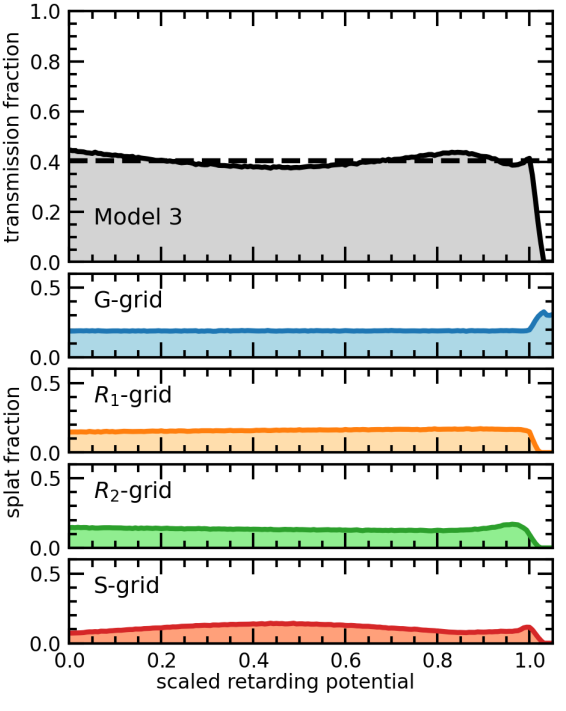

Figure 4.14: Simulation results of the transmission (top row) and splat fractions (lower rows) for ions through a model that resembles the actual RFA used in our experiments(see Fig. 4.2). The optical transmission of this stack configuration is 47 %.

the earlier the loss in transmission starts. In addition, there is a slow shift of the transmission peak towards lower potentials with decreasing ion energy. This signals the enhanced effect of the negative suppressor voltage on the potential at the position of the second retarder grid (R_2) when the maximum retarder voltage needed to block the ions gets lower for low-energy incoming ions. Together with the suppressor voltage constituting an increasing contribution to the energy of the ions, this turns the retarder - suppressor system into a strong electrostatic lens.

In practice, this behavior implies that a fundamental trade-off in the design and operation of retarding field analyzers is required for low-energy ions ($E_0 \ll 100\,\mathrm{eV}$). The suppressor potential is indispensable for minimizing secondary electrons from escaping the FC. However, when kept constant at a relatively high value, it can disproportionately affect the transmission of low-energy ions. As a rule of thumb, Fig. 4.12 suggests that if $|qE_0/V_S| > 1$, the effect is not yet significant.

At smaller ratios of $|qE_0/V_S|$ the common transmission curve needs to be adjusted or one needs to accept that the absolute current measurement is slightly higher due to secondary electrons escaping from the FC. This effect is likely negligibly small, as for low-energy ions and in particular for singly charged ions the secondary electrons have energies well below 20 eV. For low-energy measurements, a suppressor voltage of $-100\,\mathrm{V}$ is therefore typically not needed. We investigated whether similar transmission curves are obtained for identical $|qE_0/V_S|$ ratios at lower ion beam energies and correspondingly reduced suppressor voltages. Fig. 4.13 compares the cases of 50 eV and 100 eV ion beams with a suppressor voltage of $-100\,\mathrm{V}$ (corresponding to $|qE_0/V_S|$ ratios of 0.5 and 1, respectively), as presented in Fig. 4.12, with the combinations of 10 eV and $-20\,\mathrm{V}$ ($|qE_0/V_S| = 0.5$) and 50 eV with $-50\,\mathrm{V}$ ($|qE_0/V_S| = 1$). It is observed that the transmission curves overlap closely when the same $|qE_0/V_S|$ ratio is maintained, indicating that the transmission behavior is primarily governed by this ratio rather than the absolute suppressor voltage.

4.5.3 Random grid alignment (Model 3, $T_{\mathrm{opt}} = 47\%$)

Model 3 has a grid configuration that resembles the actual RFA shown in Fig. 4.2. None of the grids are either aligned or staggered with respect to the entrance grid. The results of the trajectory simulations are shown in Fig. 4.14.

From the figure, it is seen that now, with the grids arranged randomly rather than in a strictly aligned or staggered manner, the transmission curve becomes noticeably flatter. No single grid dominates the loss of ions by splatting, and their contributions are more evenly spread out over the retarder voltage range.

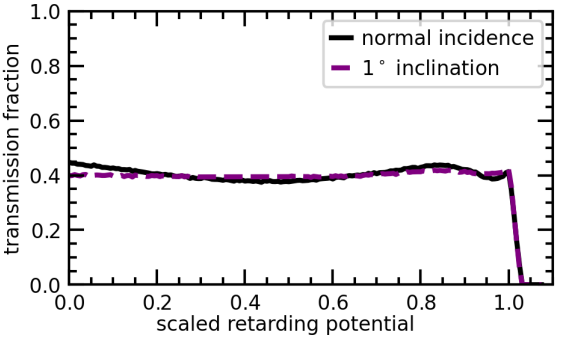

Figure 4.15: Simulated transmission characteristics for the "random" grid configuration (model 3) for a 4 keV He^{1+} ion beam at normal incidence (black solid line) and at 1° inclination (purple dashed line) with respect to the grid normal.

Consequently, the characteristic initial drop and oscillatory structures seen in the ordered configurations are largely suppressed. This suggests that randomization effectively averages out the grid-specific effects, leading to a smoother and more uniform transmission behavior. These findings are consistent with the experimental results shown in Fig. 4.6, which exhibit only a slight change in transmission at low barrier voltages. However, the pronounced dip and peak present in the experimental figures are not reproduced by the simulations. This discrepancy may partly arise from the simplified nature of the simulation model with randomly aligned grids, which only approximates the complex grid stack configuration illustrated in Fig. 4.2.

In addition, another factor might be beam divergence. The maximum angle defined by the collimating diaphragms in our experimental setup is approximately 1°. To assess the effect of a small inclination angle of the incoming beam, an additional simulation was performed and is shown in Fig. 4.15. It appears that the inclusion of a small inclination angle in the incoming beam even further flattens the transmission curve.

Both non-ideal alignment and beam divergence have the tendency to flatten the transmission curve of an RFA, implying that RFA design should not aim for perfect grid alignment. This complements the work of Trottenberg et al. [23] who reached the same conclusion for rotational grid alignment of grids with circular holes.

4.6 Conclusion

In this work, the voltage-dependent transmission of a four-grid retarding field analyzer has been investigated through a combination of monoenergetic ion-beam experiments and detailed ion-trajectory simulations. Experimentally, all investigated ion species and charge states experience the same characteristic transmission-voltage response when the retarding voltage is scaled by qV_R/E_0, demonstrating that the observed behavior is an intrinsic property of the analyzer rather than a feature of the incoming beam. Initially, the transmission changes only weakly with retarding voltage, followed by a pronounced dip and sharp peak just below the cutoff voltage. At lower ion energies, deviations from this universal curve occur due to the increasing relative influence of the fixed suppressor potential.

The simulations reproduce the essential features of the measured transmission curves and provide a physical explanation of their origin. They show that the transmission is affected by electrostatic lensing effects arising from the grid apertures and their relative alignment. As a retarding voltage is applied, these lensing effects slightly bend ion trajectories, particularly those passing through the grid near the grid wires. This enhances the probabilities of interception by the subsequent grid(s). Which one of the grids that dominates the ion loss depends on the relative alignment of consecutive grids. In particular, aligned grid pairs promote voltage-dependent focusing that leads to systematic transmission losses, while staggered or randomly aligned configurations tend to suppress such effects.

Near the cutoff voltage, the suppressor grid plays a decisive role in shaping the transmission function. For certain grid configurations, ions that pass the retarding grids are strongly focused onto the suppressor, producing oscillatory features in the transmission curve. These oscillations are most pronounced when the suppressor or second retarding grid is staggered with respect to its predecessor. At low ion energies, the fixed suppressor voltage significantly alters the effective retarding field, shifting and distorting the transmission curve and imposing practical constraints on absolute flux measurements.

Overall, the results demonstrate that RFA transmission cannot be adequately described by simple optical transparency estimates or by multiplicative transmission rules. Instead, transmission is a voltage-dependent function determined by an interplay of grid geometry, alignment, spacing, and electrode biasing. Accurate quantitative interpretation of RFA measurements therefore requires explicit considerations of this transmission function, particularly when deriving the ion energy distribution function or measuring absolute ion fluxes. These findings underscore the importance of analyzer-specific calibration or simulation-based

correction methods and provide clear guidelines for the design and operation of RFAs with improved and more stable transmission characteristics.

Acknowledgments

This work was conducted as part of the research program of the Advanced Research Center for Nanolithography (ARCNL), a public-private partnership of the University of Amsterdam (UvA), Vrije Universiteit Amsterdam, University of Groningen (RuG), the Netherlands Organisation for Scientific Research (NWO) and the semiconductor equipment manufacturer ASML. The experiments were performed at the ZERNIKELEIF facility operated by the Zernike Institute for Advanced Materials at the University of Groningen.

References

[1] W. B. Hanson, D. R. Zuccaro, C. R. Lippincott, and S. Sanatani, "The retarding-potential analyzer on Atmosphere Explorer", Radio Sci. **8**, 333–339 (1973).

[2] R. A. Pitts, R. Chavan, S. J. Davies, S. K. Erents, G. Kaveney, G. F. Matthews, G. Neill, and J. E. Vince, "Retarding field energy analyzer for the JET plasma boundary", Rev. Sci. Instrum. **74**, 4644–4657 (2003).

[3] D. Gahan, B. Dolinaj, and M. B. Hopkins, "Retarding field analyzer for ion energy distribution measurements at a radio-frequency biased electrode", Rev. Sci. Instrum. **79**, 033502 (2008).

[4] F. Schlichting and H. Kersten, "A retarding field thermal probe for combined plasma diagnostics", EPJ tech. instrum. **10** (2023).

[5] S. W. Tang and W. Gekelman, "Design of a retarding field energy analyzer for the large plasma device", EPJ tech. instrum. **52** (2024).

[6] S. Kagaya, H. Takahashi, T. Seino, K. Yoshimura, R. Nishimura, A. Kanno, Y. Takahashi, T. Hara, T. Oishi, A. Matsuyama, and K. Tobita, "Determination of parallel and perpendicular ion temperatures based on selective ion transmission in a retarding field analyzer", Plasma Fusion Res. **19**, 1201021 (2024).

[7] Y. Damizia, S. Elmore, P. Ryan, S. Allan, F. Federici, N. Osborne, J. W. Bradley, and the MAST-U Team, "First ion temperature measurements in the MAST-U divertor via retarding field energy analyzer", Nucl. Mater. Energy **43**, 101912 (2025).

[8] B. Zhao, D. C. Donovan, J. Ren, and M. D. Phillips, "Novel data interpretation method for DIII-D divertor retarding field energy analyzer with 3-D particle-in-cell simulations", Rev. Sci. Instrum. **95**, 073512 (2024).

[9] K. Bijlsma, L. Oltra, E. de Wit, L. Assink, I. Rabadan, L. Méndez, and R. Hoekstra, "Electron capture from molecular hydrogen by metastable Sn^{2+*} ions", Atoms **12**, 9 (2024).

[10] P. K. Saha, D. Roy, and M. Chakraborty, "Generation of supersonic ion beams in the down stream of multiple double layer", Phys. Lett. A **545**, 130486 (2025).

[11] S. Balachandran Nair, A. Chandrika Sreekantan, and R. Sudharshan Kaarthik, "Metrological evaluation of a programmable gain current-sensing digitizer suitable for retarding potential analyzers", IEEE Sens. J. **23**, 29073–29083 (2023).

[12] A. Caldarelli, F. Filleul, R. Boswell, C. Charles, N. Rattenbury, and J. Cater, "Data processing techniques for ion and electron-energy distribution functions", Phys. Plasmas **30**, 040501 (2023).

[13] A. Caldarelli, R. Andriulli, F. Ponti, J. Cater, and N. Rattenbury, "Effect of input power on plasma expansion and ion acceleration in a radio-frequency plasma thruster", Acta Astronaut. **226**, 521–530 (2025).

[14] A. Thomas and K. Lemmer, "Time-resolved ion energy measurements using a retarding potential analyzer for electric propulsion applications", Rev. Sci. Instrum. **95**, 023505 (2024).

[15] L. Poirier, A. C. Lassise, R. Hoekstra, J. Sheil, and O. O. Versolato, "Laser-intensity dependence of ion emission from Nd:YAG-laser-produced plasma expanding into vacuum", Phys. Plasmas **30**, 083505 (2023).

[16] S. Rai, K. I. Bijlsma, L. Poirier, E. de Wit, L. Assink, A. C. Lassise, I. Rabadan, L. Méndez, J. Sheil, O. O. Versolato, and R. Hoekstra, "Evidence of production of keV Sn^{+} ions in the H_2 buffer gas surrounding a Sn-plasma EUV source", Plasma Sources Sci. Technol. **32**, 035006 (2023).

[17] J. Sheil, L. Poirier, A. C. Lassise, S. Schouwenaars, N. Braaksma, A. Frenzel, R. Hoekstra, and O. O. Versolato, "Power-law scaling relating the average charge state and kinetic energy in expanding laser-driven plasmas", Phys. Rev. Lett. **133**, 125101 (2024).

[18] Y. Sakai and I. Katsumata, "An energy resolution formula of a three plane grids retarding field energy analyzer", Jpn. J. Appl. Phys. **24**, 337–341 (1985).

[19] D. Gahan, B. Dolinaj, and M. B. Hopkins, "Comparison of plasma parameters determined with a Langmuir probe and with a retarding field energy analyzer", Plasma Sources Sci. Technol. **17**, 035026 (2008).

[20] T. Baloniak, R. Reuter, C. Flötgen, and A. von Keudell, "Calibration of a miniaturized retarding field analyzer for low-temperature plasmas: geometrical transparency and collisional effects", J. Phys. D: Appl. Phys. **43**, 055203 (2010).

[21] K. Denieffe, C. M. O. Mahony, P. D. Maguire, D. Gahan, and M. B. Hopkins, "Retarding field energy analyser ion current calibration and transmission", J. Phys. D: Appl. Phys. **44**, 075205 (2011).

[22] T. van de Ven, C. A. de Meijere, R. M. van der Horst, M. van Kampen, V. Y. Banine, and J. Beckers, "Analysis of retarding field energy analyzer transmission by simulation of ion trajectories", Rev. Sci. Instrum. **89**, 043501 (2018).

[23] T. Trottenberg, F. Bansemer, M. Hesse, H. Kersten, J. Laube, V. Schneider, B. Schuster, L. Seimetz, and R. F. Wimmer-Schweingruber, "The role of grid geometry and relative orientation in the performance of a retarding potential analyzer", AIP Adv. **15**, 035030 (2025).

[24] J. H. Klenzing, G. D. Earle, and R. A. Heelis, "Errors in ram velocity and temperature measurements inferred from satellite-borne retarding potential analyzers", Phys. Plasmas **15**, 062905 (2008).

[25] K. Bijlsma, E. de Wit, J. L. Pascual, A. Kleinsmit, E. Lalkens, L. Assink, M. Salverda, L. Méndez, O. O. Versolato, I. Rabadán, and R. Hoekstra, "Electron capture in low-energy collisions of Sn^{3+} ions with H_2 and D_2", Phys. Rev. A **112**, 052806 (2025).

[26] G. Lubinski, Z. Juhász, R. Morgenstern, and R. Hoekstra, "State-selective electron-capture cross section measurements for low-energy collisions of He-like ions on H_2", J. Phys. B: At. Mol. Opt. Phys. **33**, 5275–5296 (2000).

[27] R. Geller, *Electron cyclotron resonance ion sources and ecr plasmas* (Springer-Verlag GmbH, 1996).

[28] O. O. Versolato, J. Sheil, S. Witte, W. Ubachs, and R. Hoekstra, "Microdroplet-tin plasma sources of EUV radiation driven by solid-state-lasers", J. Opt. **24**, 054014 (2022).

[29] D. A. Dahl, J. E. Delmore, and A. D. Appelhans, "SIMION PC/PS2 electrostatic lens design program", Rev. Sci. Instrum. **61**, 607 (1998).

[30] D. A. Dahl, "SIMION for the personal computer in reflection", Int. J. Mass Spectrom. **200**, 3–25 (2000).

CHAPTER 5

The open retarding field analyzer

Lennart Tinge, Luc Assink, Sjoerd Buitjes, Ciska van Elsberg,
Mart Salverda, Oscar Versolato, and Ronnie Hoekstra

In preparation

Abstract

Retarding field analyzers are widely used for ion energy measurements, but their performance is often limited by the presence of grids, which can introduce transmission uncertainties and produce secondary electrons when hit by intercepted ions. In this chapter, an open retarding field analyzer (oRFA) is presented, in which the grids are removed and replaced by a carefully designed electrode geometry to establish a well-defined retarding field. The design of the oRFA is discussed, with particular emphasis on maintaining field uniformity in the absence of grids. Ion trajectory simulations show that a sufficiently uniform potential barrier can be achieved, which is essential for preserving energy resolution. The performance of the oRFA is experimentally tested using a 5 keV He^{1+} ion beam, demonstrating good agreement with simulations: a constant transmission and a sharp transmission cutoff. A direct comparison with a conventional gridded RFA reveals that the oRFA resolved the drawbacks of a gridded RFA. Simulations show that the oRFA maintains a step-like transmission behavior down to 10 eV. These results demonstrate that gridless operation is feasible without compromising energy resolution. The oRFA therefore offers a robust alternative to conventional RFAs for ion energy measurements in a wide range of plasma conditions.

5.1 Introduction

Laser-produced plasma (LPP) sources, such as those based on Sn for EUV lithography, generate ion populations characterized by a broad distribution of both charge states and kinetic energies. These distributions play a crucial role in determining the interaction of the plasma with its surroundings and the overall energy balance of the system, making their accurate characterization essential. A variety of diagnostic techniques exist for ion characterization [1–3]. Current-collecting detectors such as Faraday cups provide only the total collected charge, integrated over all energies and charge states. Time-of-flight methods enable reconstruction of kinetic energy from arrival time using the near-instantaneous generation of all ions at laser impact, but do not inherently distinguish between charge states. More advanced techniques, such as electrostatic analyzers [4, 5] or Thomson parabola spectrometers [3], provide improved selectivity, but typically at the expense of increased system complexity, size, and sensitivity to alignment and operating conditions.

Within this landscape of diagnostic techniques, retarding field analyzers (RFAs) offer a practical balance between simplicity and energy selectivity. Operating as high-pass energy filters, RFAs enable controlled reconstruction of ion energy distributions, particularly when combined with time-resolved techniques [6, 7]. In contrast to detector systems based on microchannel plates or channeltrons, RFAs can be implemented using Faraday cups, allowing operation under relatively high background pressures (as in Chapter 1) and making them suitable for a broad range of experimental conditions. Their compactness and geometric flexibility further enable angularly resolved measurements without significantly increasing experimental complexity.

Despite these advantages, conventional RFAs typically rely on multiple grids to establish a near-perfect uniform retarding field. The grids introduce complications, such as uncertainties in transmission and contributions from secondary electrons to the measured currents. Such electrons may be generated by ions, photons, and electrons interacting with the grid surfaces. Although a dedicated suppressor grid is commonly employed to prevent these electrons from contributing to the signal, electrons generated on the suppressor grid itself cannot be effectively suppressed. As demonstrated in Chapter 3, the yield of ion-induced electron emission depends on both the charge state and kinetic energy of the incident Sn ions, and it was shown that measurable electron emission persists even below the expected thresholds for electron emission. As a result, the measured current can include contributions that are not directly proportional to the transmitted ion flux, complicating quantitative interpretation. In addition, as shown in Chapter 4, the ion transmission of a gridded retarding field analyzer depends on the applied

retarding voltage and is therefore not equal to the optical transmission of the grids. A significant fraction of ions is intercepted by the grids, with the exact losses depending on grid alignment. In particular, certain alignments can lead to enhanced interception at the suppressor grid, which in turn enhances the production of ion-induced electron emission, further contributing to the measured signal. Removing the grids appears as a natural strategy to mitigate these limitations. However, this simplification generally comes at the cost of reduced energy resolution.

Gridless and simplified RFA concepts have been explored extensively over the past decades. A prominent example is found in plasma propulsion and thruster diagnostics [8–10], where instruments are required to operate under extreme conditions of high particle fluxes and energetic ion bombardment. In such environments, grids are prone to rapid degradation due to sputtering and can introduce additional measurement artifacts, making gridless designs desirable. A wide range of alternative RFA configurations has been proposed [8–13]. These include simplified geometries with only a few electrodes [14], in some cases using the Faraday cup itself as the retarding element [10, 15], as well as designs that incorporate lens-type electrodes to partially recover energy selectivity by controlling particle trajectories [12, 13]. Fundamentally different gridless concepts have also been proposed [11].

In this chapter, we introduce and evaluate an open retarding field analyzer (oRFA). Other gridless designs, motivated by preventing grids from affecting (electron) flux measurements, often suffered from reduced energy resolution. The present open design specifically aims to retain the energy resolution of our conventional gridded RFAs. In the following, the research approach, including the experimental setup and ion trajectory simulations, is identical to that described in Chapter 4 and will therefore not be repeated here. Instead, the focus is placed on the conceptual design and performance of the oRFA. We first discuss the design considerations underlying the analyzer and its practical implementation. Subsequently, the simulated and experimentally measured transmission characteristics of the oRFA are presented and directly compared to those of the conventional gridded RFA introduced in Chapter 4, enabling a systematic evaluation of the impact of removing the grids.

5.2 Design of the open RFA

In the present design, the aim is to retain sufficient ion current and maintain an energy resolution of $\sim 1\,\%$ comparable to the conventional gridded RFA discussed in Chapter 4. The energy resolution of an RFA is governed by the uniformity of

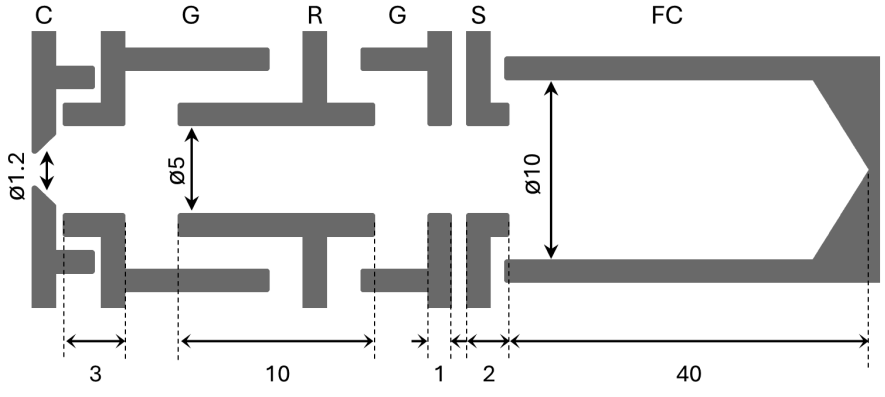

Figure 5.1: Schematic representation of the open retarding field analyzer (oRFA), showing the arrangement of cylindrical electrodes and their respective dimensions (in mm). The analyzer consists of an entrance cap (C) with a collimating aperture, followed by a grounded electrode (G), a retarding electrode (R), a second grounded electrode (G), and a suppressor electrode (S) positioned in front of a Faraday cup (FC).

the retarding potential within the holes of the grids (gridded RFA) or the open electrode in the case of an open RFA. This relationship was already discussed in the 1980s by Sakai and Katsumata [16], who showed that the resolution depends on the length and diameter of the retarding electrode, as well as the distances to the neighboring grounded electrodes. To ensure a sufficient ion signal in LPP applications, the aperture must remain on the order of millimeters, comparable to that of the conventional gridded RFAs. To prevent ion interception at the electrodes, the electrode diameter must be significantly larger than the opening aperture. This geometric constraint implies that the electrodes must be sufficiently long in order to achieve a well-defined and uniform retarding potential along the axis, while maintaining adequate energy resolution.

Fig. 5.1 presents a simplified schematic of the oRFA, together with the respective diameters and lengths of the different electrodes. The design relies on a carefully arranged set of cylindrical electrodes. The analyzer consists of an entrance cap with a collimating aperture, followed by a sequence of electrodes: a ground electrode (G), a retarder electrode (R), a second ground electrode (G), and a suppressor electrode (S) positioned in front of a Faraday cup detector (FC). The overall dimensions of the oRFA are chosen such that the analyzer remains compatible with fitting in a standard CF40 vacuum tube. This ensures that the oRFA can directly replace (or vice versa) our conventional gridded

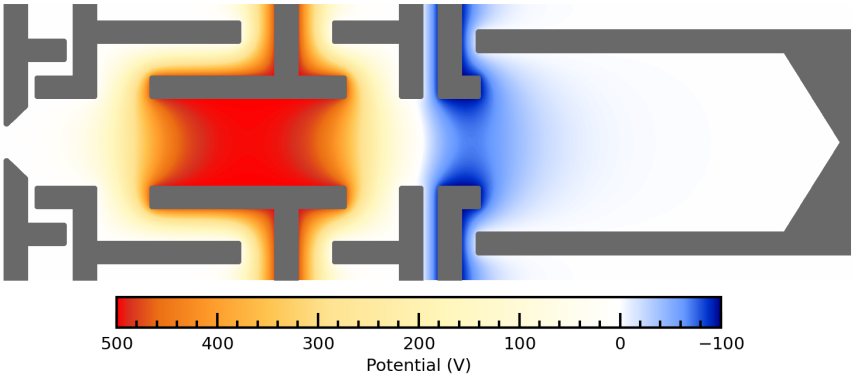

Figure 5.2: Illustration of the potential field lines within the SIMION model of the oRFA. The retarding electrode voltage was set to 500 V and the suppressor voltage to −100 V. The field lines in the retarding electrode show little variation in the center of the electrode, indicating a uniform potential barrier.

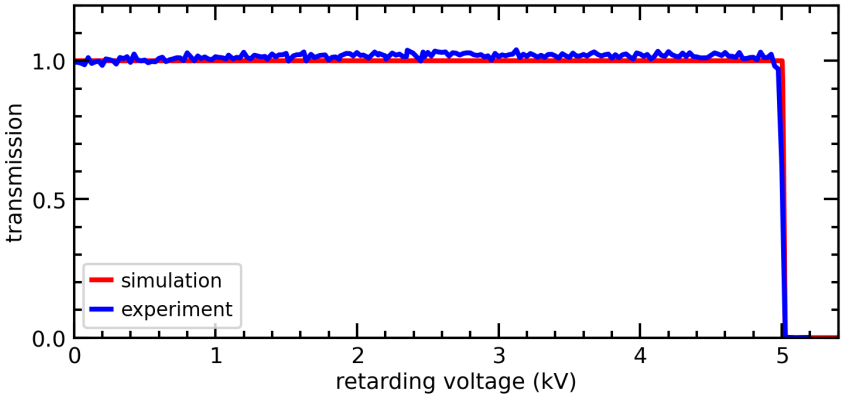

Figure 5.3: Ion transmission of the open retarding field analyzer (oRFA) for a 5 keV He^{1+} ion beam as a function of the retarder voltage. The experimental transmission (blue) is compared to the simulated transmission (black). In both cases the suppressor voltage is fixed at −100 V.

RFA (Chapters 1 and 4), enabling one-to-one comparison measurements without requiring modifications to the experimental setup.

Fig. 5.2 shows a cross section of the potential landscape of the oRFA as obtained from the SIMION software package, for a set retarding voltage of 500 V and a suppressing voltage of −100 V. It demonstrates that the potential in the central region of the retarding electrode is nearly constant across the radial direction, indicating that ions traversing this region experience a well-defined and uniform energy barrier. This results in an expected energy resolution of the analyzer of better than 1%. A key aspect of the design is the inclusion of a second ground electrode positioned between the retarder and suppressor electrodes. This intermediate electrode effectively decouples the two regions, ensuring that the respective electric fields do not significantly influence one another despite the large potential difference. As a result, distortion of the retarder field by the suppressor field (and vice versa) is minimized. Consequently, ions traveling through the oRFA encounter a nearly ideal retarding potential across a broad range of ion energies.

5.3 Results

Fig. 5.3 shows the transmission of the oRFA for a 5 keV He^{1+} ion beam. The experimentally obtained transmission (blue) is compared to the simulated transmission obtained from ion trajectory simulations (black). The simulated transmission exhibits the expected ideal high-pass filter behavior, with 100 % transmission below the cutoff and an abrupt transition to zero at a retarding voltage of 5 kV. This sharp edge reflects the nearly uniform retarding field that is achieved with the optimized electrode geometry of the oRFA. The experimental transmission closely follows the simulated curve over the entire range of retarding voltages. Below the cutoff voltage, a flat transmission plateau is observed, demonstrating that ion losses within the analyzer are negligible. The cutoff region is slightly broadened compared to the simulation, which can most likely be attributed to a small, finite energy spread of the ion beam. Nevertheless, the transition remains sharp, confirming that the oRFA preserves a high energy resolution even in the absence of grids.

In Fig. 5.4, the experimentally obtained transmission function of the open RFA (blue) is compared to the transmission of a conventional gridded RFA (green), as presented in Chapter 4. Measurements were performed using He^{1+} ion beams, with an energy of 5 keV for the oRFA and 4 keV for the gRFA. To allow direct comparison, the retarding potential is expressed as a scaled potential, defined as the ratio of the applied retarding voltage and the ion energy. A value of unity,

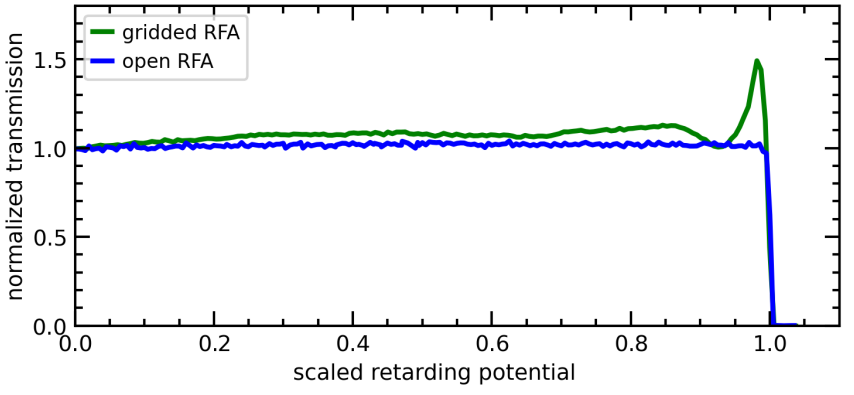

Figure 5.4: Comparison of the measured transmission function of the open RFA (blue, 5 keV He^{1+}) and the gridded RFA (green, 4 keV He^{1+}), shown as a function of the scaled retarding potential, i.e., the retarding voltage is normalized to the ion energy. The transmission is normalized to the ion current at zero retarding voltage. In both cases the suppressor voltage is fixed at −100 V.

therefore, corresponds to the cutoff voltage for each respective beam energy. The transmission on the vertical axis is scaled similarly by normalizing the measured current to the current at zero retarding voltage. A clear difference is observed between the two analyzer responses. The oRFA transmission remains close to unity over the entire range below the cutoff, without exhibiting significant variations as a function of retarding potential. This indicates that the transmission is largely independent of the applied voltage and that no additional structure is introduced by the analyzer itself. This behavior contrasts strongly with the gRFA, where the transmission can increase by up to 50 % relative to its optical transmission and exhibits pronounced structure near the cutoff point. Such variations are absent in the oRFA response, demonstrating that the transmission remains stable and does not depend on the retarding potential. The absence of these unwanted features indicates that the mechanisms responsible for transmission distortions in the gRFA are absent in the open RFA design, resulting in a response that perfectly matches the intended high-pass energy filtering.

As discussed in Chapter 4, the voltage-dependent transmission of the gridded RFA becomes increasingly energy dependent when the ion energy approaches the magnitude of the fixed suppressor voltage (i.e. −100 V). In this regime, the suppressor field no longer acts as a minor correction but starts to significantly influence ion trajectories. As a result, the measured transmission function is no longer solely determined by the retarding potential, but also depends on the ion

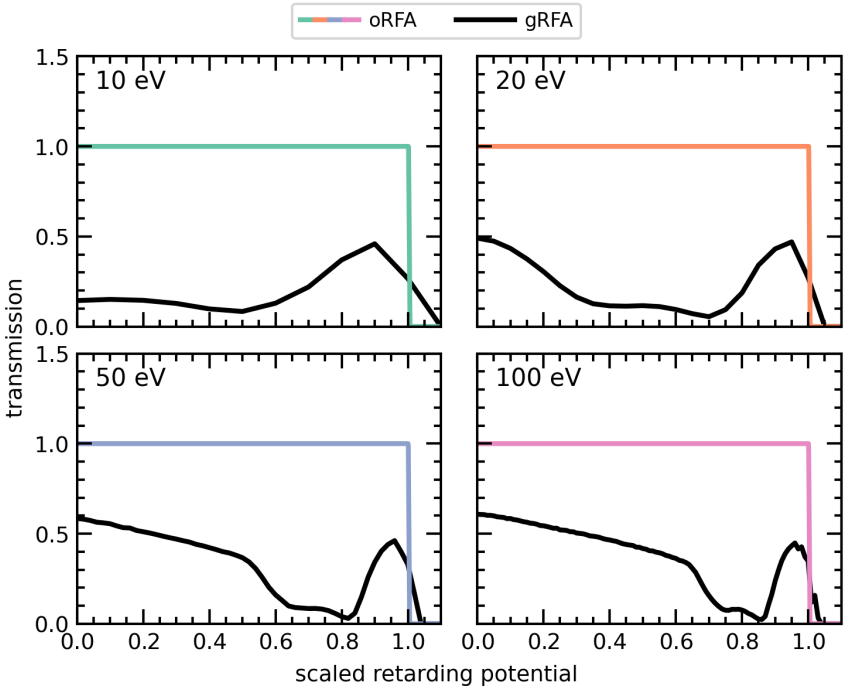

Figure 5.5: Simulated ion transmission of the open RFA (colored) and gridded RFA (black) for monoenergetic ion beams with energies of 10, 20, 50, and 100 eV. The retarding potential is scaled to the ion energy. In all cases, the suppressor voltage is fixed at −100 V.

energy itself. Fig. 5.5 shows the simulated transmission functions of the oRFA and the gRFA for low-energy monoenergetic ion beams with energies of 10, 20, 50, and 100 eV. The retarding potential is scaled to the ion energy, such that unity corresponds to the cutoff voltage. The oRFA transmission functions are basically not affected by the suppressor voltage, even at ion energies as low as 10 eV. Therefore, the oRFA is superior to the gRFA, for which the transmission function becomes increasingly distorted and structured towards lower ion energies. Furthermore, the effective cutoff shifts to higher retarding voltages, implying that the retarding field is no longer solely determining the energy threshold, but is influenced by the suppressor field. This degrades the energy resolution of the analyzer. All these effects are not observed in the oRFA. This can be attributed to the addition of an extra ground electrode between the retarder and the suppressor electrodes, which effectively shields the retarding region from the suppressor field.

5.4 Conclusion

In this chapter, an open retarding field analyzer has been introduced as an alternative to conventional gridded RFAs. The design removes the use of grids and instead relies on a carefully optimized electrode geometry to establish a well-defined retarding field. As discussed, this requires careful consideration of the electrode configuration, since grids in traditional RFAs play a key role in enforcing field uniformity. The presented design demonstrates that, by appropriate shaping and shielding of the electrodes, a sufficiently uniform retarding potential can be achieved without the use of grids.

The performance of the oRFA has been validated through a combination of ion trajectory simulations and experiments using a 5 keV He^{1+} ion beam. The measured transmission closely follows the simulated responses, exhibiting a flat, 100 % transmission below the cutoff and a sharp transition at the expected retarding voltage. This agreement confirms that the oRFA provides a well-defined energy filtering characteristic while maintaining a high energy resolution. A comparison with the transmission behavior of a conventional gridded RFA, as presented in Chapter 4, highlights the impact of removing grids. The oRFA transmission remains constant over the full range below the cutoff and does not exhibit voltage-dependent variations that are characteristic of gridded designs. This demonstrates that the open geometry effectively removes mechanisms that lead to transmission distortions, resulting in a response that reflects a perfect high-pass filter. Furthermore, simulations for low ion energies show that the oRFA response remains constant over a wide energy range. In contrast to gridded RFAs, where the transmission becomes increasingly energy-dependent when the ion energy approaches the suppressor voltage, the oRFA maintains the energy-independent transmission function and a well-defined cutoff till energies as low as 10 eV. This is due to the inclusion of a ground electrode between the retarder and suppressor electrodes, which effectively decouples the retarding field from the suppressor field.

Overall, the results demonstrate that gridless operation outperforms gridded operation. By eliminating both voltage-dependent and energy-dependent transmission effects associated with grids, the oRFA provides a more stable and interpretable response. This makes it the diagnostic of choice for ion energy measurements in a wide range of plasma environments. Future work should focus on applying the oRFA in laser-produced plasma experiments to assess its performance under harsh operating conditions.

Acknowledgments

This work was conducted as part of the research program of the Advanced Research Center for Nanolithography (ARCNL), a public-private partnership of the University of Amsterdam (UvA), Vrije Universiteit Amsterdam, University of Groningen (RuG), the Netherlands Organisation for Scientific Research (NWO) and the semiconductor equipment manufacturer ASML. The experiments were performed at the ZERNIKELEIF facility operated by the Zernike Institute for Advanced Materials at the University of Groningen.

References

[1] W. Demtröder and W. Jantz, "Investigation of laser-produced plasmas from metal-surfaces", Plasma Phys. **12**, 691 (1970).

[2] R. Dinger, K. Rohr, and H. Weber, "Ion distribution in laser-produced plasma on tantalum surfaces at low irradiances", J. Phys. B **13**, 2301 (1980).

[3] S. Fujioka, H. Nishimura, K. Nishihara, M. Murakami, Y. G. Kang, Q. Gu, K. Nagai, T. Norimatsu, N. Miyanaga, Y. Izawa, K. Mima, Y. Shimada, S. Sunahara, and H. Furukawa, "Properties of ion debris emitted from laser-produced mass-limited tin plasmas for extreme ultraviolet light source applications", Appl. Phys. Lett. **87**, 241503 (2005).

[4] A. O'Conner, O. Morris, and E. Sokell, "Angular and energy distribution of Sn ion debris ejected from a laser-produced plasma source, for laser power densities in the range suitable for extreme ultraviolet lithography", J. Appl. Phys. **107**, 073301 (2011).

[5] L. Poirier, A. Bayerle, A. Lassise, F. Torretti, R. Schupp, L. Behnke, Y. Mostafa, W. Ubachs, O. O. Versolato, and R. Hoekstra, "Cross-calibration of a combined electrostatic and time-of-flight analyzer for energy- and charge-state-resolved spectrometry of tin laser-produced plasma", Appl. Phys. B **128**, 1 (2021).

[6] P. Yeates, C. Fallon, E. T. Kennedy, and J. T. Costello, "Charge resolved electrostatic diagnostic of colliding copper laser plasma plumes", Phys. Plasmas **18**, 103104 (2011).

[7] L. Poirier, A. C. Lassise, Y. Mostafa, L. Behnke, N. Braaksma, L. Assink, R. Hoekstra, and O. O. Versolato, "Energy-and charge-state-resolved spectrometry of tin laser-produced plasma using a retarding field energy analyzer", Appl. Phys. B **128**, 053302 (2021).

[8] S. Falabella and A. W. Molvik, "Ion temperature measurements on TMX-U using a gridless electrostatic analyzer", Rev. Sci. Instrum. **61**, 1892–1899 (1990).

[9] C. M. Marrese, N. C. Majumdar, J. M. Haas, G. J. Williams, L. B. Ring, and A. D. Gallimore, "Development of a single-orifice retarding potential analyzer for hall thruster plume characterization", in Iepc 97-066, 25th international electric propulsion conference (1997).

[10] F. G. Hey, M. Vaupel, C. Groll, M. Tajmar, A. Sell, K. Eckert, D. Weise, N. Saks, and U. Johann, "Development of a gridless retarding potential analyser", in Proceedings of the 35th international electric propulsion conference (2017).

[11] T. W. Shyn, W. E. Sharp, and P. B. Hays, "Gridless retarding potential analyzer for use in very-low-energy charged particle detection", Rev. Sci. Instrum. **47**, 1005–1015 (1976).

[12] S. D. Johnson, M. M. El-Gomati, and L. Enloe, "High-resolution retarding field analyzer", J. Vac. Sci. Technol. B **21**, 350–353 (2003).

[13] J. Hwang, K. Kim, T. Ogawa, B. Cho, D. Kim, and I. Park, "Study and design of a lens-type retarding field energy analyzer without a grid electrode", Ultramicroscopy **209**, 112880 (2020).

[14] H. C. Paulini and U. Littmark, "A simple and compact retarding field energy analyzer for the characterization of broad ion beams of low energy", Nucl. Instrum. Methods Phys. Res. B: Beam Interact. Mater. At. **58**, 260–265 (1991).

[15] N. R. Lobanov, T. Tunningley, and P. Linardakis, "High-resolution grid-less retarding potential analyser and its application for sputter negative ion source", Nucl. Instrum. Methods Phys. Res. A: Accel. Spectrom. Detect. Assoc. **1050**, 168169 (2023).

[16] Y. Sakai and I. Katsumata, "An energy resolution formula of a three plane grids retarding field energy analyzer", Jpn. J. Appl. Phys. **24**, 337–341 (1985).

CONCLUSION & OUTLOOK

Optimization of EUV source modeling critically depends on the ability to accurately predict the interactions of energetic Sn ions ejected from the laser-produced plasma generating the EUV light. As outlined in this work, model input requires a detailed and reliable atomic-scale description of slow heavy ion interactions with both gases and solid surfaces. However, such a description was yet incomplete, with relevant cross sections largely unknown, and commonly used models rely on simplified assumptions that are not always justified. These limitations raised the central question addressed in this thesis: *to what extent can the required data on the atomic-scale interactions of slow heavy Sn ions under EUV source conditions be obtained in dedicated experiments?*

This thesis addressed this question by combining both experimental and modeling efforts across two types of interactions relevant for EUV source operation: (i) ion–gas interactions, which govern the slowing down and charge-state evolution of Sn ions in the hydrogen buffer gas, and (ii) ion–surface interactions, which determine how ions interact with plasma-facing components, leading to processes such as scattering, sputtering, and electron emission. In addition to these collision processes, accurate characterization of the emitted ion distributions is essential, as they form the starting point for any quantitative description of these interactions. Therefore, the development and assessment of diagnostic tools, in particular retarding field analyzers, constitute a crucial third pillar of this work.

In the following, the conclusions of the individual chapters are summarized. Together, these findings are used to address the central question of this thesis. Finally, an outlook is provided, focusing on both the remaining open questions and the development of improved diagnostic approaches relevant for EUV lithography source applications.

In Chapter 1, we consider the energy-loss mechanisms governing ion-gas interaction of Sn^{1+} ions in H_2. At present, a consistent description remains lacking: existing modeling efforts attempt to reproduce the limited experimental data available, yet do not converge to a unified picture. This reflects both the scarcity of experimental benchmarks and the incomplete nature of the current atomic-scale description. To advance this understanding, we investigated the stopping of keV Sn^{1+} ions in H_2. Stopping cross sections were obtained over an energy range from approximately 0.1 to 3 keV. A clear transition in the energy dependence was observed around 600 eV, from an approximately linear scaling (αE) at low energies to a weaker dependence ($\alpha E^{0.35}$) at higher energies. Based on stopping theory, we attributed this behavior to a transition between two distinct nuclear stopping regimes: a shift from hard-sphere-like interactions at low energies to a regime at slightly higher energies, where atomic collisions are governed by screened Coulomb potentials. In addition, results from a new semi-classical collision model were presented, showing very good agreement with the experimental data across the full energy range. In contrast to previously used approaches, this model explicitly retains the molecular structure of H_2 in the stopping calculations. This underlines the importance of incorporating system-specific interaction potentials and the molecular nature of H_2 to accurately describe stopping in the keV energy

In Chapter 2 and 3, we investigated ion–surface interactions of slow heavy Sn ions. Here, too, conventional descriptions prove insufficient. In Chapter 2, we addressed the apparent absence of a distinct single-collision peak in keV heavy-ion scattering, which is expected based on the binary collision approximation. We examined whether surface roughness could account for this absence through a combined experimental and simulation study. While surface roughness was found to influence spectral features, it could not explain the absence of the single-collision peak. Simulations showed that even small local surface inclinations modify spectral shapes, but are insufficient to account for the observed suppression. These results indicate that scattering of slow heavy ions cannot be described within a purely binary framework, but instead involves inherently multi-body interactions.

In Chapter 3, we further demonstrated that conventional expectations for ion-induced electron emission also break down in this regime. We investigated electron emission induced by Sn^{1-5+} ions impacting different surfaces at velocities where kinetic emission is expected to be absent. For Sn^{1+} and Sn^{2+}, potential energy-driven electron emission is also expected not to be possible. Nevertheless, a clear and finite electron yield was detected. The electron yield increases approximately linearly with ion velocity, the common trend in KE-driven

electron emission. This demonstrates that, for heavy ions, KE electron emission begins well below the commonly assumed threshold velocities observed for lighter ions. For higher charge states (Sn^{3-5+}), an additional velocity-independent contribution to the yield was identified, attributed to PE. By separating this contribution from the velocity-dependent KE component, we showed that PE remains relatively small, but increases with charge state. A material dependence was observed, with Cu exhibiting the highest overall yields, while Sn and stainless steel had comparable electron yields, roughly half that of Cu. Together, these findings reinforce that ion-surface interactions in this regime are governed by a complex interplay of mechanisms, including many-body effects that are not captured by simplified models.

In Chapter 4 and 5, we focused on the reliability of the RFA, the commonly used diagnostic tool for LPP Sn ion distribution measurements. In Chapter 4, we showed that the transmission of a conventional gridded RFA is both voltage- and energy-dependent. Grid-induced electrostatic lensing can enhance ion interception on specific grids, resulting in pronounced dips and peaks in measured ion currents. These effects depend sensitively on grid alignment and are reduced, but not eliminated, by "random" alignment of the grids. This hampers an accurate determination of ion energy distributions. It is of note that these findings do not affect the validity of the results in Chapter 1, since relative shifts in the cutoff of the energy distributions were used.

In Chapter 5, we present a gridless RFA design circumventing most of the limitations of gridded RFAs. Both simulations and experiments demonstrate that this oRFA exhibits a constant transmission function, independent of analyzer voltage. Moreover, the transmission remains stable in the low-energy regime, where conventional gridded RFAs show strong energy dependence. The oRFA design significantly improves the reliability of ion diagnostics under EUV-related conditions. All gridded RFAs at our LPP sources at ARCNL are being replaced by open RFAs.

These limitations raised the central question addressed in this thesis: *to what extent can the required data on the atomic-scale interactions of slow heavy Sn ions under EUV source conditions be obtained in dedicated experiments?*
Taken together, the findings presented in this thesis demonstrate that commonly employed simplified descriptions are insufficient to capture the complexity of slow heavy-ion interactions. Rather than being governed by a single dominant mechanism, the observed behavior arises from the interplay of multiple coupled (many-body) processes, including elastic scattering and inelastic electronic pro-

cesses. This complexity is evident in both ion–gas and ion–surface interactions. Consequently, while important aspects of ionic interactions can now be described with improved accuracy, a fully reliable and complete atomic-scale picture has not yet been achieved, though it is within reach.

Outlook

Several open questions and promising directions for future research remain. For ion–gas interactions, additional stopping studies are essential. The stopping experiments presented in this thesis were performed using ions emitted from an LPP source. Future measurements using monoenergetic ion beams would provide valuable benchmark data with improved control over the initial collision conditions. This includes: (i) extracting stopping cross sections for Sn^{2+} ions to gain insight into the role of charge state during ion transport through the hydrogen buffer gas, and (ii) stopping in partially charged target environments, as collisions in EUV source conditions do not necessarily occur exclusively with neutral species. In parallel, additional calibration and validation of stopping models remain important. In particular, stopping measurements for Sn ions on atomic targets, like He, could serve as a valuable benchmark for further refinement on the recently developed stopping code.

For ion–surface interactions, under EUV source conditions, energetic ions are expected to be strongly decelerated by the buffer gas before even reaching plasma-facing components, such that many ions ultimately impact surfaces in the (1–100) eV-energy regime. The interaction mechanisms in this low-energy regime remain poorly understood and should therefore be investigated in more detail. In particular, scattering, neutralization, and electron emission by slow heavy ions would be highly relevant. However, detection of interaction products, in particular neutrals, remains challenging. On top of that, in situ studies of implantation processes in relevant source environments require major advances in experimental techniques. The development of such experimental techniques seems a necessary step toward a more complete understanding of ion–surface interactions in EUV environments.

Finally, continuing to push for the best diagnostic techniques remains crucial, as accurate characterization of emitted ion distributions is the input to all model simulations. Taken together, continued advances in experimental techniques, diagnostics, and modeling efforts will be essential to complete the atomic-scale picture required for the further optimization of EUV lithography sources.

NEDERLANDSE SAMENVATTING

ZWAARGEWICHTEN: Interacties van tin-ionen uit EUV-bronplasma

Computerchips vormen de basis van vrijwel alle moderne elektronische apparaten, van smartphones en laptops tot auto's en medische apparatuur. De voortdurende toename in hun rekenkracht heeft de digitale revolutie mogelijk gemaakt en vormt de drijvende kracht achter nieuwe technologieën, zoals kunstmatige intelligentie. Binnen een computerchip zijn het de transistoren die de berekeningen uitvoeren. Hoe meer transistoren op een chip passen, hoe groter de rekenkracht.

Deze transistoren worden op een chip aangebracht met behulp van fotolithografie, een technologie waarbij met licht minuscule patronen op een siliciumwafel worden geprojecteerd. Voortdurende ontwikkelingen binnen deze technologie maken het mogelijk om steeds kleinere transistoren te printen, waardoor er meer op dezelfde chip passen. Daarbij is de golflengte van het gebruikte licht de belangrijkste factor. Hoe korter de golflengte, hoe kleiner de transistoren die gemaakt kunnen worden.

De chipindustrie is in de loop der jaren dan ook meerdere keren overgestapt op licht met een kortere golflengte, van zichtbaar licht naar licht dat voor het menselijk oog onzichtbaar is. Het zichtbare deel van het lichtspectrum loopt van ongeveer 400 tot 700 nanometer (nm). Aan de kortgolvige kant bevindt zich violet licht, met een golflengte van ongeveer 400 nm. Licht met een nog kortere golflengte is voor het menselijk oog onzichtbaar en wordt daarom ultraviolet ("voorbij violet") genoemd. Dit ultraviolette deel van het spectrum strekt zich grofweg uit van 100 tot 400 nm. Tegen het einde van de vorige eeuw maakten de meest geavanceerde lithografiemachines al gebruik van diep ultraviolet (DUV) licht met een golflengte van 193 nm, waarmee aanzienlijk kleinere transistoren konden worden vervaardigd dan met zichtbaar licht mogelijk was.

Al in de jaren negentig werd er gezocht naar manieren om voor de volgende generatie lithografiemachines nog kortere golflengten te gebruiken. Bij zulke extreem korte golflengten wordt staling echter door vrijwel alle materialen geabsorbeerd, inclusief lucht. Dit betekende dat de lithografiemachine grondig moest worden herontworpen. Lenzen moesten plaatsmaken voor spiegels en het hele proces moest zich voortaan in vacuüm afspelen. Na tientallen jaren van onderzoek en ontwikkeling leidde dit uiteindelijk toch tot een nieuwe generatie lithografiemachines die gebruikmaken van extreem ultraviolet (EUV) licht met een golflengte van slechts 13,5 nm. Het duurde echter tot ongeveer 2018–2019 voordat de technologie volwassen genoeg was om op grote schaal te worden ingezet in de chipproductie. Tot op de dag van vandaag is het Nederlandse ASML het enige bedrijf ter wereld dat zulke machines kan bouwen. Dankzij deze unieke en uiterst geavanceerde technologie kunnen transistoren verder worden verkleind, waardoor er meer dan ooit tevoren op een computerchip passen.

Een van de technologische hoogstandjes van de nieuwste generatie lithografiemachines is de EUV-lichtbron. Om dit licht te maken, wordt een microscopisch klein druppeltje tin (Sn) meermaals beschoten met een krachtige laser. Het tin absorbeert de laserenergie, waardoor veel elektronen van de tinatomen loskomen. Een atoom dat één of meerdere elektronen verliest, wordt een positief geladen ion. Zo ontstaat een lasergeproduceerd plasma: een "soep" van tin-ionen en vrije elektronen. Een plasma is een extreem hete toestand van materie, vergelijkbaar met wat je in de zon aantreft.

Het licht zelf ontstaat op een net iets andere manier. Elektronen die nog wél aan de tin-ionen gebonden zijn, kunnen door de laserenergie naar een hogere energietoestand worden gebracht. Vallen ze vervolgens terug naar een lagere energietoestand, dan zenden de tin-ionen licht uit. Tin is voor dit proces bijzonder geschikt: veel van deze overgangen leveren licht op met een golflengte van ongeveer 13,5 nm.

Dit licht wordt opgevangen door een schotelvormige opvangspiegel, die het doorstuurt naar de volgende onderdelen van de machine. Het plasma produceert echter niet alleen het gewenste EUV-licht: er komen ook energetische tindeeltjes vrij. Worden deze niet tegengehouden, dan kunnen ze aanzienlijke schade toebrengen aan de opvangspiegel, met directe gevolgen voor de prestaties, levensduur en betrouwbaarheid van de lichtbron. Om dit te voorkomen wordt de lichtbron gevuld met een buffergas van waterstof. Op weg naar de spiegel botsen de tindeeltjes met de waterstofmoleculen, waardoor ze worden afgeremd en de spiegel niet meer kunnen bereiken.

Maar hoeveel waterstof is hiervoor eigenlijk nodig? En hoeveel schade richten deze tindeeltjes aan wanneer ze de spiegel toch weten te bereiken? Vragen als deze zijn alleen te beantwoorden met complexe simulatiemodellen, en die staan of vallen met een gedetailleerde en betrouwbare atoomfysische beschrijving van hoe deze zware tin-ionen wisselwerken met zowel gassen als vaste stoffen. Die beschrijving is op dit moment nog verre van compleet. Een beter begrip van deze interacties kan daarom ook bijdragen aan een verdere optimalisatie van de EUV-lichtbron, al is het verkrijgen van die kennis allesbehalve eenvoudig.

Dit brengt ons bij de centrale onderzoeksvraag van dit proefschrift: in welke mate kunnen de benodigde gegevens over atomaire-schaal-interacties van langzame, zware Sn-ionen onder EUV-bronomstandigheden worden verkregen met gerichte experimenten? Om deze vraag te beantwoorden zijn experimentele en modelleringsstudies uitgevoerd naar twee relevante interacties: (i) ion-gasinteracties, die verantwoordelijk zijn voor de afremming van tin-ionen in het waterstofbuffergas, en (ii) ion-oppervlakte-interacties, die bepalen hoe

ionen reageren met aan het plasma blootgestelde componenten. Daarnaast is een nauwkeurige karakterisering van de uitgezonden ionenenergieverdeling onmisbaar, aangezien deze het uitgangspunt vormt voor elke kwantitatieve beschrijving van deze interacties. De ontwikkeling en evaluatie van diagnostische instrumenten vormden dan ook een derde essentiële pijler van dit werk.

Ion-gasinteracties

Het overgrote deel van de Sn-ionen die het lasergeproduceerde tinplasma uitzendt, is hooggeladen (typisch met ladingstoestanden tussen 4+ en 8+) en heeft energieën van enkele honderden eV tot meerdere keV. Op weg door het buffergas botsen deze ionen met de H_2-moleculen. Bij zo'n botsing geeft het Sn-ion een deel van zijn energie af aan het waterstof. Ook kan het één of twee elektronen van het H_2-molecuul 'afpakken'. Door het grote massaverschil is de energieoverdracht bij een botsing relatief klein, terwijl elektroneninvangst juist vaak voorkomt. Daardoor vindt de ladingsoverdracht, vereenvoudigd gezegd, plaats voordat de Sn-ionen sterk worden afgeremd. Lange tijd werd aangenomen dat de ladingsoverdracht stopt bij Sn^{2+}, omdat verdere elektroneninvangst energetisch ongunstig is. Recent onderzoek heeft echter laten zien dat ook aanzienlijke hoeveelheden Sn^{1+}-ionen worden gevormd. Hierdoor is het afremvermogen van H_2-moleculen voor Sn^{1+}-ionen van direct belang geworden.

Over dit botsingssysteem is echter nog weinig bekend. Tot voor kort was er maar één experimentele studie naar het afremvermogen van H_2 voor Sn^{1+}-ionen. Deze studie liet zien dat de metingen sterk afwijken van de voorspellingen van het veelgebruikte SRIM-model. Er zijn verschillende redenen om aan de betrouwbaarheid van SRIM te twijfelen in dit specifieke geval. SRIM beschrijft een waterstofmolecuul namelijk als twee onafhankelijke waterstofatomen, het houdt geen rekening met de ladingstoestand van het projectiel en gebruikt een algemene ZBL-interactiepotentiaal. Belangrijke eigenschappen van het specifieke botsingssysteem blijven hierdoor waarschijnlijk buiten beeld.

In hoofdstuk 1 zijn nieuwe resultaten voor het afremvermogen van H_2 voor Sn^{1+}-ionen gepresenteerd. Experimentele resultaten zijn verkregen door te meten hoe een karakteristieke afsnijding in het vluchttijdsignaal verschuift bij verschillende waterstofdrukken. Hieruit werd de werkzame stopdoorsnede bepaald. De metingen laten zien dat het afremvermogen systematisch lager ligt dan de eerder beschikbare waarden. Tegelijkertijd liggen de nieuwe resultaten tussen de voorspellingen van recent gepubliceerde modellen, die onderling sterk verschillen.

Onze metingen laten daarnaast zien dat het afremvermogen van H_2 voor Sn^{1+}-ionen rond 600 eV een duidelijke overgang vertoont: van een vrijwel lineaire

energieafhankelijkheid bij lage energieën naar een zwakkere afhankelijkheid bij hogere energieën. Deze overgang kan worden verklaard door een overgang tussen twee regimes van nucleaire stopkracht. Ons semi-klassieke botsingsmodel reproduceert de experimentele resultaten bovendien zeer nauwkeurig over het volledige energiebereik. Het model houdt expliciet rekening met de moleculaire structuur van H_2 en gebruikt interactiepotentialen die specifiek voor dit systeem zijn bepaald. De resultaten laten daarmee zien dat deze details belangrijk zijn voor het beschrijven van het afremvermogen in het keV-energiebereik. Tegelijkertijd laat het verschil met de eerdere studies zien dat aanvullende metingen nodig zijn om het afremvermogen van H_2 voor Sn^{1+}-ionen definitief vast te stellen en de verschillende theoretische modellen verder te testen.

Ion-oppervlakte-interacties

Wanneer een ion op een oppervlakte inslaat, kan het energie verliezen door elastische verstrooiing of inelastische elektronische processen. Conventionele modellen beschrijven elastische verstrooiing meestal goed, maar zijn doorgaans minder betrouwbaar voor zware ionen bij lage energieën. Eerdere experimenten lieten zien dat een duidelijke enkelvoudige-verstrooiingspiek, zoals voorspeld door binaire botsingsmodellen, ontbreekt in gemeten energieverdelingen. Een mogelijke verklaring was dat oppervlakteruwheid ionen bij bepaalde verstrooiingshoeken geometrisch kan blokkeren.

In hoofdstuk 2 is deze hypothese getest met behulp van argon (Ar), krypton (Kr) en xenon (Xe) in dezelfde ladingstoestand en met dezelfde kinetische energie. De ionen verschillen daarmee in massa en snelheid. Als oppervlakteruwheid verantwoordelijk is voor het blokkeren van ionbanen, zou dit voor alle drie de ionen moeten optreden. Voor Ar en Kr werd een duidelijke enkelvoudige-verstrooiingspiek gemeten, terwijl deze voor Xe sterk was onderdrukt. Simulaties lieten zien dat kleine lokale hellingen van het oppervlak het verstrooiingspatroon beïnvloeden, maar niet genoeg om de waargenomen onderdrukking te verklaren. Oppervlakteruwheid beïnvloedt de gemeten energieverdelingen dus wel, maar verklaart niet het volledig verdwijnen van de enkelvoudige-verstrooiingspiek. De interactie van langzame, zware ionen met oppervlakken lijkt daarom niet volledig met een binair botsingsmodel te kunnen worden beschreven. Veeldeeltjesinteracties lijken hierbij een belangrijke rol te spelen.

Naast verstrooiing kunnen ionen bij een botsing met een oppervlak ook elektronen vrijmaken. Dit proces, ion-geïnduceerde elektronenemissie, vormt een belangrijke energieverliesroute. In hoofdstuk 3 is onderzocht of de conventionele beschrijving van dit proces ook geldig is voor langzame, zware ionen.

Ion-geïnduceerde elektronenemissie werd gemeten voor Sn^{1+}–Sn^{5+} die inslaan op roestvrij staal, koper en tin. Uit de metingen bleek dat Sn^{1+}- en Sn^{2+}-ionen elektronen vrijmaken bij energieën ver onder de door bestaande modellen voorspelde drempel. De elektronenopbrengst neemt ongeveer lineair toe met de ionensnelheid, wat kenmerkend is voor kinetische elektronenemissie. Kinetische elektronenemissie treedt bij zware ionen dus al op bij veel lagere snelheden dan doorgaans wordt aangenomen.

Voor Sn^{3+}–Sn^{5+} werd daarnaast een snelheidsonafhankelijke bijdrage aan de elektronenopbrengst waargenomen. Deze is toegeschreven aan potentiële elektronenemissie, waarbij de potentiële energie van het ion vrijkomt tijdens neutralisatie aan het oppervlak. Door deze bijdrage te scheiden van de snelheidsafhankelijke component bleek dat de potentiële emissie duidelijk toeneemt met de ladingstoestand. Ook werd een duidelijke materiaalafhankelijkheid gevonden: koper geeft de hoogste elektronenopbrengst, terwijl tin en roestvast staal vergelijkbare opbrengsten geven. Deze resultaten laten zien dat zowel de eigenschappen van het ion als die van het oppervlak een belangrijke rol spelen bij ion-geïnduceerde elektronenemissie bij lage energieën.

Diagnostische ioneninstrumentatie

De retarding field analyzer (RFA) is een diagnostisch instrument waarmee de energieverdeling van geladen deeltjes uit een plasma kan worden bepaald. Ook de energieverdeling van tin-ionen uit een lasergeproduceerd plasma kan hiermee worden gemeten. Omdat de RFA in dit werk alleen voor ionenmetingen is gebruikt, wordt de werking hier vanuit het perspectief van ionendetectie beschreven.

Een RFA bestaat doorgaans uit meerdere elektroden met afzonderlijke spanningen, gevolgd door een Faraday cup (FC) waarin de deeltjesstroom wordt gemeten. Door een spanning aan te leggen op de afremelektrode kunnen alleen ionen met voldoende kinetische energie deze elektrode passeren en de FC bereiken. Een onderdrukkingselektrode voorkomt daarnaast dat elektronen de FC binnenkomen of verlaten, zodat de gemeten stroom uitsluitend afkomstig is van de ionen.

Conventionele RFA's maken gebruik van fijnmazige metalen gaasjes om een goed gedefinieerd elektrisch veld te creëren. In hoofdstuk 4 is echter aangetoond dat deze gaasjes de ionentransmissie sterk afhankelijk maken van de afremspanning en ionenenergie. Door elektrostatische lenswerking kunnen de openingen in een gaasje ionen focusseren of defocusseren, waardoor deze met grotere kans door volgende gaasjes worden onderschept. Dit veroorzaakt pieken en dalen in de gemeten ionenstroom die niet afkomstig zijn van de werkelijke ionenenergieverdeling. De effecten zijn bovendien sterk afhankelijk van de onderlinge uitlijning van

de gaasjes, waardoor elke RFA met gaasjes een unieke 'vingerafdruk' heeft. Dit bemoeilijkt een nauwkeurige bepaling van de ionenenergieverdelingen.

In hoofdstuk 5 werd een nieuw RFA-ontwerp onderzocht: de open RFA (oRFA), een RFA zonder gaasjes. Zowel simulaties als metingen toonden aan dat de oRFA een constante ionentransmissie heeft, ook in het lage-energiegebied waar conventionele RFA's een sterke energieafhankelijkheid vertonen. Hierdoor kan de gemeten ionenstroom rechtstreeks worden gerelateerd aan de onderliggende ionenenergieverdeling, zonder complexe transmissiecorrecties. Dit maakt een betrouwbaardere bepaling van ionenenergieverdelingen onder EUV-relevante omstandigheden mogelijk.

De praktische waarde van het ontwerp blijkt uit het feit dat de conventionele RFA's bij de lasergeproduceerde plasmabronnen van ARCNL inmiddels worden vervangen door open RFA's. De ontwikkeling biedt daarmee niet alleen een verbetering van de diagnostiek van EUV-plasma's, maar ook een direct toepasbare oplossing voor toekomstige experimenten.

De resultaten van dit proefschrift laten zien dat veelgebruikte vereenvoudigde beschrijvingen onvoldoende zijn om de complexiteit van interacties van deze langzame zwaargewichten te vatten. Het waargenomen gedrag wordt niet gedomineerd door één enkel mechanisme, maar ontstaat juist uit een samenspel van meerdere processen, waaronder elastische verstrooiing en inelastische elektronische processen. Deze complexiteit manifesteert zich zowel in ion-gas- als in ion-oppervlakte-interacties.

Hoewel belangrijke aspecten van deze interacties nu met grotere nauwkeurigheid kunnen worden beschreven, is een complete beschrijving op atomaire schaal nog niet bereikt. Deze resultaten laten echter zien dat dit doel binnen handbereik komt.

LIST OF PUBLICATIONS

Chapter 1

L. Assink, T. Nieboer, J. Bijma, B. Neijzen, K. Bijlsma, L. Poirier, E. de Wit, D.J. Engels, J. Sheil, O.O. Versolato, and R. Hoekstra, "On the stopping of laser-plasma produced Sn^{1+} ions in molecular hydrogen gas", Nucl. Instrum and Methods Phys. Res. B, under review (2026).

Chapter 2

L. Assink, J. Brötzner, C. Cupak, M. Salverda, H. Jonkman, O.O. Versolato, R.A. Wilhelm, and R. Hoekstra, "On the question whether surface roughness can explain the absence of a prominent single-collision peak in keV heavy-ion scattering off a polycrystalline Ru surface", Nucl. Instrum and Methods Phys. Res. B **554**, 165442 (2024).

Chapter 3

L. Assink, V. Vojtech, R.A. Wilhelm, and R. Hoekstra, "Electron emission induced by slow Sn^{1-5+} ions on metal surfaces", in preparation.

Chapter 4

L. Assink, E. de Wit, F. Veen, K. Bijlsma, O.O. Versolato, and R. Hoekstra, "The voltage dependent transmission function of a retarding field analyzer", Nucl. Instrum and Methods Phys. Res. B **579**, 166217 (2026).

Chapter 5

L. Tinge, L. Assink, S. Buitjes, C. van Elsberg, M. Salverda, O.O. Versolato, and R. Hoekstra, "The open retarding field analyzer", in preparation.

The author also contributed to the following publications:

G.H. ten Brinke, X. Zhu, W. Guo, K. Blauw, L. Assink, V.B. Svetovoy, and B.J. Kooi, and G. Palasantzas, "Wetting of surfaces decorated by gas-phase synthesized silver nanoparticles: Effects of Ag adatoms, nanoparticle aging, and surface mobility", J. Chem. Phys. **155**, 214701 (2021).

L. Poirier, A. Lassise, Y. Mostafa, L. Behnke, N. Braaksma, L. Assink, R. Hoekstra, and O.O. Versolato, "Energy- and charge-state-resolved spectrometry of tin laser-produced plasma using a retarding field analyzer", App. Phys. B **128**, 135 (2022).

L. Poirier, D.J. Hemminga, A. Lassise, L. Assink, R. Hoekstra, J. Sheil, and O.O. Versolato, "Strongly anisotropic ion emission in the expansion of Nd:YAG-laser-produced plasma", Phys. Plasmas **29**, 123102 (2022).

S. Rai, K.I. Bijlsma, L. Poirier, E. de Wit, L. Assink, A. Lassise, I. Rabadán, L. Méndez, J. Sheil, O.O. Versolato, and R. Hoekstra "Evidence of production of keV Sn^{+} ions in the H_2 buffer gas surrounding an Sn-plasma EUV source", Plasma Sci. Technol. **32**, 035006 (2023).

K. Bijlsma, L. Oltra, E. de Wit, L. Assink, I. Rabadán, L. Méndez, and R. Hoekstra, "Electron capture from molecular hydrogen by metastable Sn^{2+}* ions", Atoms **12**, 9 (2024).

K. Bijlsma, E. de Wit, J.L. Pascual, A. Kleinsmit, E. Lalkens, L. Assink, M. Salverda, L. Méndez, O.O. Versolato, I. Rabadán, and R. Hoekstra, "Electron capture in low-energy collisions of Sn^{3+} ions with H_2 and D_2", Phys. Rev. A **112**, 052806 (2025).

P

DANKWOORD

Terwijl ik aan dit dankwoord begin, besef ik dat dit de laatste woorden zullen zijn van het proefschrift dat symbool staat voor het afronden van een bijzondere periode in mijn leven. Inmiddels zijn er vier jaar verstreken, en ik vraag me oprecht af waar de tijd gebleven is. Een PhD is een lang traject, met nodige uitdagingen, omwegen en onverwachte afslagen. Toch kijk ik met niets anders dan warme gevoelens op deze jaren terug. Dat is zeker niet alleen te danken aan het onderzoek zelf, maar vooral aan de mensen die in deze periode deel hebben uitgemaakt van mijn leven. Sommigen waren er dagelijks, anderen slechts af en toe, maar ieder van jullie heeft op zijn eigen manier bijgedragen aan deze bijzondere tijd. Daar ben ik jullie ontzettend dankbaar voor! Toch zijn er een aantal mensen die ik nog graag in het bijzonder wil bedanken.

Ronnie. Ik ben je ontzettend dankbaar voor je begeleiding, steun, mentorschap en gezelschap in de afgelopen jaren. Soms kan een ontmoeting je leven blijvend veranderen. Ik heb enorm veel van je geleerd, en dan niet alleen op onderzoeksgebied. Ik kijk met goede herinneringen terug op onze gezamenlijke reizen naar Charleston, Sapporo, Frankenfels en Huizhou, de vele pubquizavonden en natuurlijk de gRFA-kerstsessies, die al vrij snel veranderden in AIVD-kerstpuzzelsessies aan de keukentafel. Het doet me veel plezier, dat we onze samenwerking nog even zullen voortzetten, en ik kijk ernaar uit, om te zien wat daar nog uit voortkomt. Sorry voor al deze komma's...

Oscar. Ik ben je dankbaar voor de begeleiding die je me als tweede supervisor hebt gegeven. Ik heb bewondering voor je kennis en de manier waarop je altijd snel tot de kern van een probleem weet door te dringen. Ik kijk met veel plezier terug op onze vele RFA- en bottom-up-discussies. Hoewel die niet altijd tot een onmiddellijk antwoord leidden, leverden ze steevast nieuwe inzichten en soms vooral nieuwe vragen op.

John. I'm thankful for all the interesting (physics) discussions we had over the last few years. I also appreciate all the humor along the way. And remember, don't throw your wallet to people in a bar.

Richard. I would like to thank you for giving me the opportunity to come to Vienna for a research stay and for the successful collaboration. My time in Vienna was a valuable part of my PhD, both scientifically and personally.

De beoordelingscommissie: **George, Jom** en **Stefan**. Ik ben jullie dankbaar voor de tijd en moeite die jullie hebben genomen om mijn proefschrift te lezen.

Mart. Je bent onmisbaar geweest. Je brede algemene én technische kennis, je geduld en vooral je bereidheid om altijd mee te denken hebben me vaak verder gebracht. Ik ben je dankbaar voor alle hulp en ik bewaar veel goede herinneringen samen, waaronder het bouwen van de hoogspanningskooi van CHEOPS in het allereerste begin en natuurlijk de verhuizing.

Klaas. Het overgrote gedeelte van mijn PhD-tijd waren we collega's, en ik kijk met veel plezier terug op die jaren samen. Van de meetcampagnes in Amsterdam en de conferenties tot de meer alledaagse gesprekken op de werkvloer: het was simpelweg erg prettig om met je samen te werken.

Het QISD-team: **Emiel, Fleur, Harry, Lennart, Linda, Mart, Ronnie, Sadia, Tara, Thije** en **Thomas**. Collega's kunnen echt het verschil maken en ik heb het wat dat betreft bijzonder getroffen. Dank voor alle gezelligheid door de jaren heen. Emiel, je hebt de hink-stap-sprong nieuw leven ingeblazen. Fleur, vroeger ging je al voor goud en dat doe je nog steeds. Lennart, geen zorgen, die detector wordt een succes. Thije, ik draag vol vertrouwen SirPhi aan je over en verheug me op onze verdere samenwerking. En vergeet niet: (diafragma-)foutjes horen er ook bij.

De Amsterdamse afdeling van de Source Department: **Aleena, Bas, Bowie, Edcel, Felix, Jerry, John, Laurens, Martijn, Mats, Mikheil, Oscar, Someshwar, Surabhi** en **Xyoisan**. Mijn bezoeken aan ARCNL zijn altijd iets om naar uit te kijken. Speciale dank aan **Laurens** voor al het voorbereidende werk om de gasgevulde DALEK-metingen te kunnen doen.

The Austrians: **Anna, Benji, Fritz, Richard**, and **Vicki**. I'm grateful for all your help, and for making sure that I had a great time during my research stays. I hope there will be many more opportunities to meet, whether in Austria, the Netherlands, or somewhere else entirely.

Alle oud-collega's uit zowel Groningen als Amsterdam: **Adam, Bo, Diko, Dion, Hugo, Jane, Jorge, Karl, Klaas, Lars, Lucas, Randy, Stan, Subam, Wim, Xin, Yahia, Yining, Youssef** en **Zoi**. Ik ben blij met alle gesprekken, samenwerkingen en momenten die we hebben gedeeld. Special thanks to **Adam** and **Lucas** for introducing me to the RFA. I am not sure whether I should thank you for that, but it certainly shaped a significant part of my PhD.

Huidige en voormalige bachelor- en masterstudenten in de groep: **Anton, Bendegúz, Bram, Ciska, Dennis, Emiel, Ennio, Fleur, Goos, Hester, Ilse, Jelger, Jesse, Kristof, Leon, Lennart, Mario, Matthieu, Matthijs, Michiel, Nathan, Patrick, Pedro, Peter, Robbert, Rutger, Samuel, Selina, Sjoerd, Sjoukje, Symen, Thije, Thijmen, Thomas A., Thomas N., Vladimir** en **Zafer**. Bedankt voor jullie inzet! In het bijzonder gaat mijn dank uit naar alle studenten die ik heb mogen begeleiden.

Het secretariaat van ARCNL: **Celine, Ellen** en **Jusra**. Het doet me altijd plezier om jullie in Amsterdam, op een conferentie of in het Groningse nachtleven tegen te komen. Jullie zijn een van die constante factoren die een organisatie als ARCNL zo prettig maken.

A

Mijn tennisteams: **Anne, Arthur, Krista, Liseth, Lukas, Maarten, Mick, Nadine, Peter** en **Renate**. Ontspanning hoorde er ook zeker bij, zowel op als naast de baan.

De zusjes: **Danae, Demi** en **Kim**. Onze avonturen begonnen in Colombia, en gingen verder in Groningen, Nijmegen en Thailand. De plek maakt voor ons niet uit. Jullie voelen toch een beetje als echte zusjes.

Mijn paranimfen: **Nick** en **Ruben**, en de feestcommissie: **Laura** en **Martijn**. Ik kan altijd op jullie kan rekenen, en het maakt me trots dat jullie 29 september naast me zullen staan. Ieder van jullie heeft op zijn eigen manier een belangrijke rol in mijn leven gespeeld in de afgelopen jaren. Mijn eeuwige dank daarvoor!

Bas en **Casper**. We go way back! Ik ben blij dat jullie vandaag de dag nog steeds in mijn leven zijn. **Jochem**. Mijn Physics Lab partner-in-crime vanaf het allereerste uur. Sommige vriendschappen beginnen blijkbaar gewoon met samen een practicum over te leven. **Liseth**. Ik koester onze vriendschap, in voor en tegenspoed. **Martijn**. De eeuwige nummer twee in Yahtzee. Het KLM-personeel (lees: niet alleen die steward) bracht ons samen. Ik zou drie stoelen voor mezelf hebben op een vlucht naar Bogotá, maar moest er toch eentje afstaan. Eerst baalde ik daarvan, maar inmiddels ben ik ze vooral dankbaar dat het zo gelopen is. **Ruben**. Eerst samen in de Kokomo, toen in de IKEA en nu in het Academiegebouw. In de tussentijd is er het nodige veranderd, maar gelukkig niet alles. Ik ben je ontzettend dankbaar voor onze onvoorwaardelijke vriendschap.

Pap en **Mam**. Kinderen nemen veel dingen snel voor vanzelfsprekend aan. Ik besef echter maar al te goed dat ik het met jullie getroffen heb. Jullie onuitputtelijke steun heeft me altijd de vrijheid gegeven om mijn eigen weg te zoeken, ook wanneer die weg niet altijd recht vooruit liep. Ik had me geen betere basis kunnen wensen. **Laura**, ik ben trots op hoe je alles aanpakt en op wat je hebt bereikt. Zoals velen zeggen: het is echt uniek wat voor band wij hebben. **Nick**, onze eerste dr. Assink! Ik heb bewondering voor wat jij hebt bereikt en vind het mooi dat we allebei onze eigen weg hebben bewandeld en uiteindelijk hier samen zijn beland. Ik hou van jullie!